

Development of sulfur-
polyacrylonitrile/graphene composite
cathode for lithium batteries

by

Jing Li

A thesis

presented to the University of Waterloo

in fulfillment of the

thesis requirement for the degree of

Master of Applied Science

in

Chemical Engineering - Nanotechnology

Waterloo, Ontario, Canada, 2013

©Jing Li 2013

AUTHOR'S DECLARATION

I hereby declare that I am the sole author of this thesis. This is a true copy of the thesis, including any required final revisions, as accepted by my examiners.

I understand that my thesis may be made electronically available to the public.

Abstract

Rechargeable lithium sulfur (Li-S) batteries are potentially safe, environmentally friendly and economical alternative energy storage systems that can potentially be combined with renewable sources including wind solar and wave energy. Sulfur has a high theoretical specific capacity of ~1680 mAh/g, attainable through the reversible redox reaction denoted as $S_8 + 16Li \leftrightarrow 8Li_2S$, which yields an average cell voltage of ~2.2 V. However, two detrimental factors prevent the achievement of the full potential of the Li-S batteries. First, the poor electrical/ionic conductivity of elemental sulfur and Li_2S severely hampers the utilization of active material. Second, dissolution of intermediate long-chain polysulfides (Li_2S_n , $2 < n < 7$) into the electrolyte and their shuttle between cathode and anode lead to fast capacity degradation and low Coulombic efficiency. As a result of this shuttle process, insoluble and insulating Li_2S/Li_2S_2 precipitate on the surface of electrodes causing loss of active material and rendering the electrode surface electrochemically inactive.

Extensive research efforts have been devoted to overcome the aforementioned problems, such as combination of sulfur with conductive polymers, and encapsulation or coating of elemental sulfur in different nanostructured carbonaceous materials. Noteworthy, sulfur-polyacrylonitrile (SPAN) composites, wherein sulfur is chemically bonded to the polymer backbone and PAN acts as a conducting matrix, have shown some success in suppressing the shuttle effect. However, due to the limited electrical conductivity of polyacrylonitrile, the capacity retention and rate performance of the SPAN systems are still very modest, which shows only 67 % retention of the initial capacity after 50 cycles for the binary system.

Recently, graphene has been intensively investigated for enhancing the rate and cycling performance of lithium sulfur batteries. Graphene, which has a two-dimensional, one-atom-thick nanosheet structure, offers extraordinary electronic, thermal and mechanical properties. Herein, a sulfur-polyacrylonitrile/reduced graphene oxide (SPAN/RGO) composite with unique electrochemical properties was prepared. PAN is deposited on the surface of RGO sheets followed by ball milling with sulfur and heat treatment. Infrared spectroscopy and microscopy studies indicate

that the composite consists of RGO decorated with SPAN particles of 100 nm average size. The PAN/RGO composite shows good overall electrochemical performance when used in Li/S batteries. It exhibits ~85% retention of the initial reversible capacity of 1467 mAh/g over 100 cycles at a constant current rate of 0.1 C and retains 1100 mAh/g after 200 cycles. In addition, the composite displays excellent Coulombic efficiency and rate capability, delivering up to 828 mAh/g reversible capacity at 2 C. The improved performance stems from composition and structure of the composite, wherein RGO renders a robust electron transport framework and PAN acts as sulfur/polysulfide absorber.

Acknowledgements

I would first and foremost give my thanks to my Lama and Buddha for their teaching and wisdom to let me have the potential to accomplish the works. I would like to give my sincere thanks to my parents and family who always give me support and love. I give everlasting gratitude to my supervisor Dr. Pu Chen for his strong dedication towards my development of knowledge and skills in research. Special thanks to Dr. Denise Gosselink and Dr. Mingqi Li, for their help on my studies. I would also like to thank my colleagues, specially to Kai (Allen) Li, Ye Tian, Xin Wang, Yongguang Zhang, Aishuak Konarov, The Nam Long DOAN, Yong Ding, Wen Xu, Baolin Chen, Zhizhen Wan for all their time and assistance. I would like to acknowledge the time and support given by my reviewers.

Table of Contents

AUTHOR'S DECLARATION.....	ii
Abstract.....	iii
Acknowledgements.....	v
Table of Contents.....	vi
List of Figures.....	ix
List of Tables.....	xii
Chapter 1 General Introduction.....	1
1.1 History of Lithium-ion batteries.....	3
1.2 Introduction to intercalation chemistry based Lithium-ion batteries.....	5
1.2.1 Mechanism and electrode materials.....	5
1.2.2 Solid-electrolyte interfacial (SEI) layer.....	7
1.3 Introduction to Lithium sulfur batteries.....	9
1.3.1 Fundamental chemistry of Li-S batteries.....	10
1.3.2 Discharge process.....	11
1.3.3 Charge Process.....	12
1.3.4 Shuttle mechanism.....	12
Chapter 2 Cathode Materials for Lithium-Sulfur batteries.....	15
2.1 General requirements of cathode materials for lithium sulfur batteries.....	16
2.2 Microporous/mesoporous carbon material.....	16
2.2.1 Mesoporous carbon.....	17
2.2.2 Microporous carbon.....	18
2.2.3 Bimodal Carbon.....	19
2.2.4 Carbon material with unique structure.....	21
2.3 Carbon nanotube.....	22
2.3.1 Sulfur coating on CNTs.....	23
2.3.2 Sulfur impregnated into CNTs.....	25

2.4 Graphene	28
2.5 Conductive Polymer	31
2.5.1 Polyacrylonitrile	32
2.5.2 Polyaniline	35
2.5.3 Polypyrrole	39
2.6 Metal oxide additives as adsorption catalyst	41
2.7 Project objective	42
Chapter 3 Techniques for Physical and Electrochemical Characterization.....	43
3.1 Scanning electron microscopy	43
3.2 Energy-dispersive X-ray spectroscopy	44
3.3 Transmission electron microscopy	45
3.4 Atomic force microscopy	46
3.5 Thermogravimetric analysis/Differential thermal analysis	47
3.6 Fourier transform infrared spectroscopy	48
3.7 X-ray Diffraction analysis	48
3.8 Elemental analysis	49
3.9 Z-potential	50
3.10 Half-cell electrochemical testing	51
3.10.1 Galvanostatic Charge/Discharge	51
3.10.2 Cyclic Voltammetry	52
3.10.3 Impedance Spectroscopy	54
Chapter 4 Fundamental Study of SPAN Composite Cathode for Li-S batteries	55
4.1 Introduction	55
4.2 Preparation of SPAN Composite	56
4.3 Effect of Sulfur content to Battery Performance	58
4.4 Effect of Conductor to Battery Performance	60
4.5 Effect of Load of Active Materials to Battery Performance.....	61

4.6 Effect of CNT as additives to Battery Performance.....	62
4.7 Summary	63
Chapter 5 A sulfur-polyacrylonitrile/graphene composite cathode for lithium batteries with excellent cyclability.....	64
5.1 Outline of the work	64
5.2 Introduction.....	64
5.3 Experimental Section	65
5.3.1 Materials	65
5.3.2 Preparation of Reduced Graphene Oxide (RGO) aqueous suspension	66
5.3.3 Polyacrylonitrile/ Reduced Graphene Oxide composite (PAN/RGO).....	66
5.3.4 Sulfur-Polyacrylonitrile/partially Reduced Graphene Oxide composite (SPAN/RGO)	66
5.3.5 Characterization	67
5.4 Results and Discussion	68
5.5 Conclusions.....	79
Chapter 6 Summary and perspective towards furthered work	80
Appendix A.....	82
Appendix B	83
Bibliography	84

List of Figures

Fig.1.1 Evolution of the consumer electronic market for lithium ion battery.....	1
Fig.1.2 HEV market evolution of the lithium ion battery.....	2
Fig.1.3 Energy density of Li-S vs other cell chemistries.....	3
Fig.1.4 The charge/discharge process in a typical lithium ion cell with layered LiCoO ₂ as the cathode and graphite as the anode.....	6
Fig.1.5 Schematic energy diagram of a lithium cell at open circuit. Eg refers to the band gap in the electrolyte. $\mu_a(\text{Li})$ and $\mu_c(\text{Li})$ refer to the lithium chemical potential in the anode and cathode, respectively.....	8
Fig.1.6 Typical model (a) and charge/discharge curves (b) of lithium-sulfur batteries.....	10
Fig.1.7 Process of polysulfides shuttle.	12
Fig.1.8 The problems of the lithium anode.....	14
Fig.2.1 (a) Schematic diagram of the sulfur/mesoporous carbon composite, in which sulfur (yellow) is confined in mesoporous carbon CMK-3, (b) Cycling performance of CMK-3/S-PEG (black) and CMK-3/S (red) at 0.1 C rate.....	17
Fig.2.2 N ₂ adsorption/desorption characterization of mesoporous carbon (MPS) and KOH activated mesoporous carbon (a-MPS) : (A) isotherms at 77K; (B) pore size distribution.....	19
Fig.2.3 (a) A) TEM and B) FESEM image of double-shelled hollow carbon spheres (DHCSs). C, D) TEM images of the sulfur-DHCS composite. E) TEM image and elemental mapping of a single sulfur-DHCS sphere, (b) Cycling performance of carbon black-sulfur (CB-S) composite and DHCS-S composite at 0.1 C rate.....	21
Fig.2.4 Scanning Electron Microscopy (SEM) images of (A) MWCNTs and (B) nano-sulfur/MWCNTs composite.....	23
Fig.2.5 (a) Schematic of sulfur/ hollow carbon nanofibers composite structure, (b) Cycling performance.	25
Fig.2.6 (A) SEM images of the disordered carbon nanotubes synthesized <i>via</i> the template wetting method. (B) Cycling performance of SDCNT-160, SDCNT-300, and SDCNT-500, which was heated at 160 °C, 300 °C, 500 °C respectively.	27
Fig.2.7 Schematic structure of the graphene-PEG-sulfur composite, SEM image of the composite and the cycling discharge capacity.....	29

Fig.2.8 (a) Representative pattern of GO immobilizing S. Yellow, red, and white balls denote S, O, and H atoms, respectively, while the others are C atoms. (b) Cycling performance of the graphene-sulfur composite at a constant current rate of 0.1C, the first two cycles are processed at 0.02C for activation;.....	30
Fig.2.9 (a) PAN dehydrogenated by sulfur, (b) Cycling performance of the PAN-sulfur composite with 54 wt.% sulfur content.	33
Fig.2.10 Proposed structure of SPAN, containing all relevant functional groups.....	34
Fig.2.11 (a) Generalized composition of PANI. The oxidation state is indicated by y which varies from 0 to 1. (b) Reversible doping and dedoping of PANI by i) redox processes between non-conducting leucoemeraldine (LE) and conducting emeraldine salt (ES), and ii) protonation reactions between non-conducting EB and ES.....	35
Fig.2.12 (A) Schematic illustration of the structure and discharge/charge process of the PANI/Sulfur composite. (B) Cycling performance.....	37
Fig.2.13 (a) TEM image of the S/T-PPy composite with 50wt. % sulfur, (b) Cycling performance.....	40
Fig.3.1 Principle of EDX.....	44
Fig.3.2 Block diagram of AFM.....	46
Fig.3.3 Bragg diffraction from a cubic crystal lattice.....	48
Fig.3.4 Diagram showing the ionic concentration and potential difference as a function of distance from the charged surface.....	50
Fig.3.5 Cyclic voltammetry waveform.....	52
Fig.3.6 Typical cyclic voltammogram where i_{pc} and i_{pa} show the peak cathodic and anodic current respectively for a reversible reaction.....	53
Fig.4.1 Preparation procedure of SPAN composite.....	56
Fig. 4.2 Charge/discharge profile for the SPAN/CNT composite with 70 wt. %.....	56
Fig. 4.3 Charge/discharge profile for the SPAN/CNT composite with 42 wt. %.....	58
Fig. 4.4 TGA results of SPAN samples carried out under N ₂ from room temperature to 600 °C.....	58

Fig. 4.5 Cycling performance of the SPAN composites with different sulfur content.....	59
Fig. 4.6 Cycling performance of the SPAN composite with KB and AB as conductor.....	60
Fig. 4.7 cycling performance of cells with different load of active materials.....	61
Fig. 4.8 SEM images of SPAN composite with CNT as additives (43 wt.% Sulfur and 10 wt.% CNT).....	62
Fig. 4.9 Rate performance of the SPAN/CNT and SPAN composite.....	63
Fig.5.1 Schematic diagram of the solvent exchange process and synthesis of the SPAN/RGO composite.....	68
Fig.5.2 AFM image of RGO sheets on a silicon wafer under tapping-mode with a cross-sectional height profile measured along the green straight line.	69
Fig.5.3 TGA of GO and RGO carried out under N ₂ from room temperature to 800 °C.....	70
Fig.5.4 FTIR spectra of GO, RGO, PAN, PAN/RGO, and SPAN/RGO.....	71
Fig.5.5 XRD patterns of graphite, RGO, PAN, PAN/RGO, SPAN/RGO, and sulfur.....	72
Fig.5.6 SEM images of RGO (A), SPAN (B) and SPAN/RGO (C).....	73
Fig.5.7 Voltage vs. capacity profile of SPAN/RGO electrode (44 wt% sulfur) at 0.1 C rate between 1.0-3.0 V	74
Fig.5.8 Cyclic voltammograms of SPAN /RGO composite electrode at a scanning rate of 0.1 mV/s	75
Fig.5.9 Discharge capacity of SPAN and SPAN/RGO (3 wt% RGO content) electrodes at different C-rates....	76
Fig.5.10 (a) Fifth galvanostatic discharge/charge curves of SPAN and SPAN/RGO at different rates and (b) EIS spectra of SPAN/RGO and SPAN composites with 44 wt% S after the 10th discharge to 1.5 V at 0.1 C rate.....	77
Fig.5.11 Cycling performance of SPAN/RGO and SPAN composite electrodes at C/10 rate.....	78

List of Tables

Table 1.1 Disadvantages and advantages of the current electrode materials.	6
Table 3.1 Colloidal Stability with the value of Zeta potential.	51
Table 4.1 Table for studying the heat treatment method, “a” refers to 1st step of the heat treatment, “b” refers to 2 nd step of the heat treatment of the material from the 1 st step, “c” refers the 3 rd heat treatment of the material achieved from the 2 nd step.....	57
Table 4.2 Porosity of two types of carbon.....	60

Chapter 1

General Introduction

Electricity and transportation tools nowadays are indispensable from people's daily life to industry production. But electricity production relies on fuel burning, and transportation still depends on the use of oil. These fuel sources are limited, and the burning of fuels leads to serious environmental pollution like global warming and climate change. Even though sustainable energy technology like wind turbines, photovoltaic cells and photo-thermal receivers have achieved significant progress, the lagging development of energy storage devices greatly limited their efficient application. [1]

In the last two decades, lithium-ion battery technology has achieved impressive success which has been widely used in portable electronics due to their high energy density compared with other rechargeable energy storage system. Lithium ion batteries have prompted the growth of the market of popular devices due to the high value of the energy content, such as lap-top computers, mobile phones, MP3s and others, which are today produced by billions of units per year as shown in Fig. 1.1 They are expected to become a promising power source that can lead us to the revolution of electrical vehicles (EV) and are also being seriously considered for efficient intermittent renewable energies storage devices. From Fig. 1.2, it can be seen that the production of battery-powered hybrid electric vehicles (HEVs) has very rapidly grown and very successfully passed from demonstration prototypes to commercial products. [2-3]

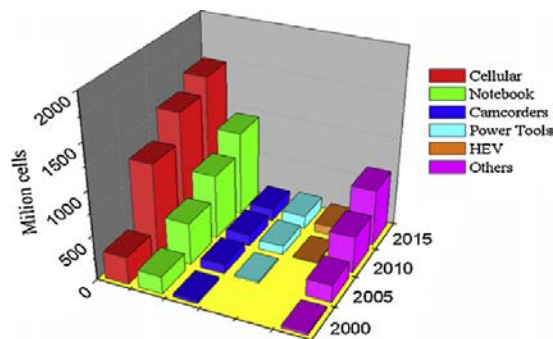


Fig. 1.1 Evolution of the consumer electronic market for lithium ion battery. Reprinted from [2] Copyright 2010 with permission from Elsevier.

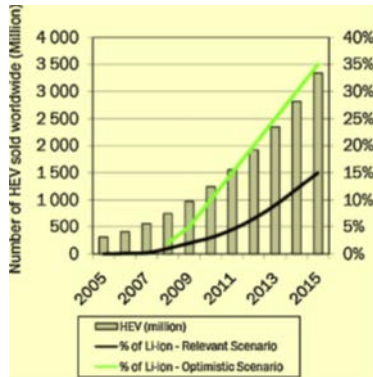


Fig. 1.2 HEV market evolution of the lithium ion battery. Reprinted from [2] Copyright 2010 with permission from Elsevier.

The dilemma in the design and operation of EVs is categorized by the depth of pure electrical propulsion. EVs can be operated at several levels and hence determined the battery pack size that should be used. There are three main options for EV operation, which are hybrid, plug in hybrid and full EV. At present, the main propulsion of commercialized hybrid EV cars (e.g. Toyota Prius) is by internal combustion engines (ICEs), where relatively small batteries (<3000 Wh <60 Kg) are used. These provide only short driving distance by electrical propulsion. However, in order to significantly reduce the use of gasoline for car propulsion, and completely shift it to electrical power for full EVs, the car batteries have to contain high energy density to enable electric cars to travel long distances. [1, 4]

After about two decades of optimization, the limits of the energy density that intercalation materials for Li-ion batteries can potentially provide, of about 300 mAhg^{-1} , are approaching. At present, for full EV's, the LIBs are not able to sustain a suitably long driving range (i.e., >300 km), and it poses limitations for PHEV. It is necessary to seek the next-generation batteries that can provide much higher energy density, and are inexpensive. Undoubtedly, these will move beyond intercalation chemistry into the realm of "integration" chemistry, where charge and discharge of the electrode is coupled with formation and cleavage of covalent bonds together with morphological or structural dynamics during redox. [5] Rechargeable lithium sulfur (Li-S) batteries are a good example

includes the electrochemical reactions. In a typical Li-S cell, as the active material of the cathode, elemental sulfur undergoes a series reduction of polysulphides Li_2S_n ($8 \leq n \leq 2$) to Li_2S during discharge. The reaction is highly reversible. The redox reaction provides a high specific capacity of 1675 mAh^{-1} and a theoretical gravimetric energy densities of about 2600 Wh kg^{-1} based on sulfur, coupled with an average cell voltage of about 2.15V . [6] Its energy density is a factor of 3–5 times higher than any commercial lithium ion cell as shown in Fig. 1.3. However, there are still challenges to attain good cycling stability at high power, which is essential for practical applications. [7]

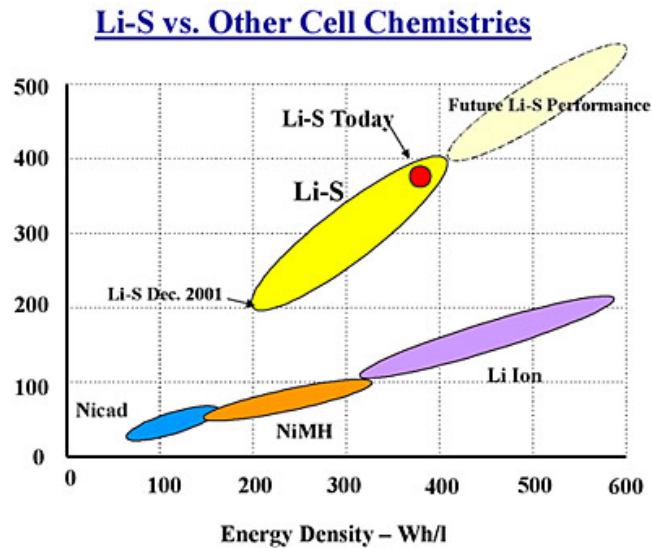


Fig. 1.3 Energy density of Li-S vs other cell chemistries, from <http://www.sionpower.com/>

1.1 History of Lithium-ion batteries

The lithium-ion battery (LIB) was invented by Asahi Kasei Co. [8] in Japan. It is first commercialized by Sony Co. [9] in 1991. Due to its good performance, high-energy density, and no memory effect compared with nickel–cadmium (Ni–Cd) or nickel-hydride (Ni–MH) batteries, the LIB was accepted immediately. Compared to lead and zinc in the traditional batteries, lithium with a high electrode potential and low atomic mass can lead to significantly high energy density for the Lithium-ion batteries. However, it requires the development of breakthrough technologies of a total

system based on new cathodes, anodes, and electrolytes to continue the steady improvement of high-energy lithium battery systems. Based on nonaqueous electrolytes such as propylene carbonate, lithium-metal anode primary batteries - lithium perchlorate and lithium negative electrodes were developed in the early 1970s. In 1973, Matsushita introduced a lithium-carbon monofluoride (Li-CFx) primary cell, and in 1975 Sanyo commercialized primary lithium-manganese dioxide primary cells (Li-MnO₂). These batteries were used for cameras, LED fishing floats, and memory backup applications. In the 1970s and 1980s, how to convert lithium primary cells into high energy density rechargeable cells drew much attention. Most of the efforts were concentrated on developing inorganic cathode compounds like conductive polymer materials such as polyacetylene. However, there is no competitive advantage for batteries made from these materials when it is scaled up due to the low density of these polymer materials, which is less than water. The low-density conductive polymer cathodes were only used for memory backup as coin cells. Moreover, the early rechargeable lithium cells were confronted with safety problems due to dendrite formation and very reactive fine powder deposits during recharge. The application of lithium-metal rechargeable cells now is confined mainly to small capacity coin cells. [10]

Then, the attention of research was shifted to the development of a lithium-intercalation material as an anode since lithium metal constituted the safety problem. A patent for an intercalation LiCoO₂ cathode material was filed by Goodenough. [11] One year after the Goodenough patent on LiCoO₂, H. Ikeda of Sanyo first patented a graphite intercalation material in an organic solvent in June 1981 Japanese (Patent No. 1769661.) [12]. In 1982, based on his finding of lithium intercalation in graphite at room temperature, Basu of Bell Laboratories filed U.S. Patent 4,423,125.[13] Using an intercalation carbon anode and a LiCoO₂ cathode I. Kuribayashi and A. Yoshino designed a new cell and filed patents worldwide. Sony Energytec Inc. developed rechargeable LiMnO₂ cells, and began to produce commercial cells in the name of Li-Ion Batteries based on the Asahi patents in 1991. The introduction of the use of lithiated transition metal oxide cathode materials- LiMO₂ as the source of lithium in the cell and graphite as the anode material instead of Li metal enables the commercialization of the rechargeable, high energy density lithium-ion batteries. [14] Graphite-

LiCoO₂ now became the leading Li-ion battery system that is used in most of the portable electronic devices: laptops, cellular phone, digital cameras, etc.

1.2 Introduction to intercalation chemistry based Lithium-ion batteries

1.2.1 Mechanism and electrode materials

The mechanism of the charge/discharge of LIBs is based on the rocking-chair concept. A typical LIB is composed of an anode (e.g., graphite), a cathode (e.g., LiCoO₂), electrolyte and separator that prevents electrodes from direct contact but allows lithium (Li) ion transfer. [15] Basically, the lithium ions are shuttled between the cathode and anode, reversible Li-ion intercalation/de-intercalation process, during the charge/discharge process. [3] During charging process, Li-ion intercalates into the anode and deintercalates from the cathode. Conversely, Li-ion deintercalates from the anode and intercalates into the cathode via the electrolyte when the battery is discharging. It enables the storage of electrochemical energy within the battery and the conversion of chemical energy into electrical energy, through the shuttle of Li ions between the cathode and the anode during charge/discharge. [16-19]

The performance of rechargeable LIBs is dependent on active materials employed in the electrodes for Li storage. The basic requirements for active materials include, low cost, good structural flexibility, high reversible capacity and stability, long cycle life, fast Li ion diffusion, improved safety, and environmental benignity. [20-22] Li-ion host materials possessing high positive redox potentials are the main source of cathodes in commercial LIBs, such as LiMn₂O₄, LiCoO₂ and LiFePO₄. [23-25] The most used commercial anode material for LIBs is graphite because of its long cycle life, low and flat working potential, and low cost. [15] The major lithium insertion electrode materials which are currently in play are provided in Table 1.1.

Table. 1.1 Disadvantages and advantages of the current electrode materials. Reprinted from [3]. Copyright 2011 with permission from American Chemical Society.

electrode material	cell voltage (V)	capacity (mA h/g)	specific energy (mWh/g)	advantages	disadvantages
layered LiCoO ₂ cathode (2-d structure)	~4	140	560	high electronic and Li ⁺ ion conductivity; revolutionized the portable electronics market	expensive and toxic Co; safety concerns; only 50% of the theoretical capacity can be utilized
spinel LiMn ₂ O ₄ cathode (3-d structure)	~4	120	480	inexpensive and environmentally benign Mn; high electronic and Li ⁺ ion conductivity; excellent rate capability; good safety	severe capacity fade at elevated temperatures (55 °C)
olivine LiFePO ₄ cathode (1-d structure)	~3.5	160	560	inexpensive and environmentally benign Fe; covalently bonded PO ₄ groups lead to excellent safety	low electronic and Li ⁺ ion conductivity; needs small particle size and carbon coating to realize high rate capability; high processing cost
graphite anode	~0.1	370	—	inexpensive and environmentally benign C; low operating potential maximizes cell voltage	SEI layer formation and lithium plating lead to safety concerns; high processing cost

The advantages and disadvantages of each system as shown in Table 1.1, often dictate their application areas. Taking the layered LiCoO₂ cathode and graphite anode as an example (Fig.1.4), the chemical reactions are described as below [3]:

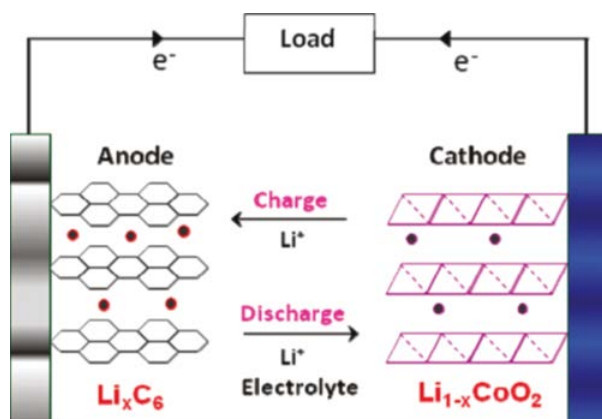


Fig. 1.4 The charge/discharge process in a typical lithium ion cell with layered LiCoO₂ as the cathode and graphite as the anode. Reprinted from [3]. Copyright 2011 with permission from American Chemical Society.

Cathode:



Anode:



Compared to Li metal-based batteries, the cathode material is the source of lithium in this system, which ensures an excellent safety features and very prolonged cycle life. Charging is always the first process in the cell, according to the delithiation and oxidation of LiCoO_2 associated with the lithiation and reduction of graphite, where the final product of graphite is LiC_6 . [1] The layered LiCoO_2 cathode has updated portable electronics like laptop computers and cell phones, but the disadvantage associated with LiCoO_2 such as the toxicity, high cost, safety concerns and chemical instability at deep charge seriously inhibit its use for stationary storage and transportation applications. An overlap of the $\text{Co}^{3+/4+}$:3d band with the top of the O^{2-} :2p band cause the consequential safety concerns and the chemical instability of LiCoO_2 . [26-27] It also limits the upper potential of the delithiation of LiCoO_2 to 4.2 V (vs. Li/Li^+). As a result, only half of the theoretical capacity of the cathode which is around 140 mAh g^{-1} can be achieved based on a reaction that limits $\text{Li}_{1-x}\text{CoO}_2$ to $0 < x < 0.5$, and is mainly first-order phase transition between LiCoO_2 and $\text{Li}_{0.5}\text{CoO}_2$. [28] Hence, due to better safety and lower cost advantages, layered materials like the $\text{LiNi}_{1/3}\text{Mn}_{1/3}\text{Co}_{1/3}\text{O}_2$ are replacing LiCoO_2 in portable electronics. In addition, because of the good chemical and structural stabilities, environmental friendliness and low cost of Mn and Fe, and high charge/discharge rate capability, spinel LiMn_2O_4 and olivine LiFePO_4 have become appealing for transportation applications. However, the drawback is their limited energy. [29, 30]

The major issue that has plagued spinel LiMn_2O_4 over the years is the disproportionation of Mn^{3+} into Mn^{4+} and Mn^{2+} which cause the dissolution of Mn. But the problem could be subdued significantly by cationic and anionic substitutions. On the other hand, for LiFePO_4 , the poor lithium ionic and electronic conduction is the major issue. These problems have been overcome by adaption of nanotechnology like coating the LiFePO_4 nanoparticles with conductive carbon. Compared to the LiMn_2O_4 -based spinel cathodes, the LiFePO_4 olivine cathodes have significant cost disadvantages by reason of the manufacturing of carbon-coated nano- LiFePO_4 . [31-36]

1.2.2 Solid-electrolyte interfacial (SEI) layer

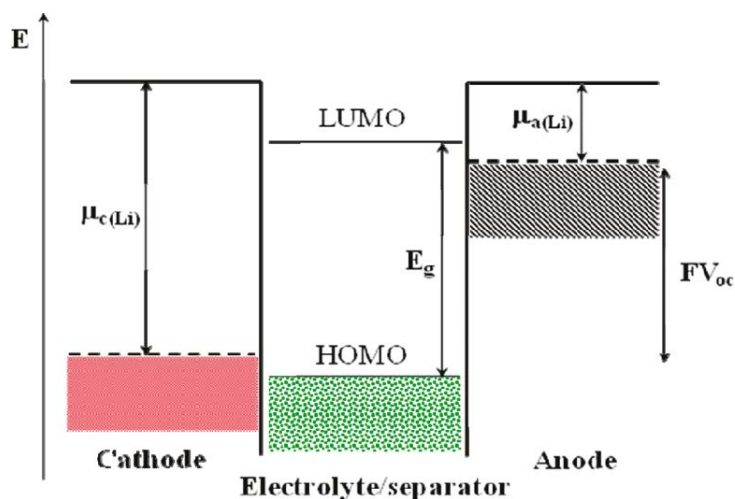


Fig. 1.5 Schematic energy diagram of a lithium cell at open circuit. E_g refers to the band gap in the electrolyte. $\mu_a(\text{Li})$ and $\mu_c(\text{Li})$ refer to the lithium chemical potential in the anode and cathode, respectively. Reprinted from [3].

Copyright 2011 with permission from American Chemical Society.

The operating voltage of graphite is close to that of Li/Li^+ , this benefits maximize the cell energy. However its electrochemical potential is above the lowest unoccupied molecular orbital (LUMO) of the electrolyte, as shown in Fig. 1.5, such as the LiPF_6 in 1:1 ethylene carbonate (EC)/diethyl carbonate (DEC) electrolyte. As a result of the transfer of electrons from the graphite anode to the LUMO of the organic solvents (EC and DEC), the electrolyte can be reduced on the graphite surface. As a result, a solid-electrolyte interfacial (SEI) layer will generate on the graphite surface. The SEI layer formed by this initial reaction prohibits the electron transfer from the anode to the electrolyte LUMO, but it also give rise to the diffusion difficulties of lithium-ion through the SEI layer leading to the deposition of metallic lithium on graphite forming a plating, which is more significant under the conditions of fast charge at cold temperatures; this lithium plating could further result in dendrite formation and become a safety hazard. This would be serious problem in application for transportation and stationary storage which requires large cells. The formation of SEI layer could also happen on the cathode surface through the oxidation of the electrolyte. When the cathode electrochemical potential is lower than the highest occupied molecular orbital (HOMO) of

the electrolyte solvent, electrons could transfer from the electrolyte HOMO to the cathode. Particularly, the SEI formation becomes severe and aggressive at elevated temperatures (~ 55 °C). [37]

The electrolyte and cathode are degraded in these reactions, and result in a lower Coulombic efficiency and capacity loss during cycling. Although strategies like introduction of additive to the electrolyte solution could suppress such reactions, but may not be able to fully solve the problem, especially for high voltage materials like spinel $\text{LiMn}_{1.5}\text{Ni}_{0.5}\text{O}_4$, olivine LiCoPO_4 , and olivine LiNiPO_4 . The limited energy and power density is still the drawback of the intercalation materials. In terms of increasing the energy density, it is necessary to look for alternative batteries, like lithium-sulfur battery. However its development also faces several technological challenges. [3]

1.3 Introduction to Lithium sulfur batteries

Pressing environmental challenges needs better energy storage systems such as long-lasting, high-energy-density, low-cost and safe rechargeable batteries, which can be combined with renewable sources like solar, wind and wave energy. In the current carbon-constrained world, especially transportation which relies on the source-limited oil, are causing global pollution increasingly due to the number of vehicles. It is inevitable to transform the traditional transportation economy to electrical vehicles. Li-ion battery based on intercalation chemistry may reach a maximum capacity and energy density due to the limited lithium ion that could be taken in the host compound. The charge storage capability of these types of batteries is inherently limited to no more than 300mAhg^{-1} . Till 2009, from the work having been reported, the maximum capacities achieved 180mAh g^{-1} . [38, 39]

The theoretical specific energy of these electrochemical systems ($\text{LiC}_6 - \text{LiXO}_2$ systems, where X is 1 or several 3-d transition elements) is in the range of 500–600 Wh/kg, and the higher power parameters of electrochemical batteries can only depend on higher theoretical specific energy of the electrochemical systems.[40] Hence, it is necessary to look for new approaches which can

provide higher energy density, lithium sulfur battery has been believed as one of the candidates as next generation battery. [41-46]

The theoretical specific energy of the lithium–sulfur electrochemical batteries are around 450–650 W h/kg. Lithium-sulfur batteries also have some other advantages like good safety due to the intrinsic over-charge protection mechanism, low cost and abundance of sulfur, wide operation temperature and possibility of long cycle life. However, problems like the fast decay of capacity during cycling, relatively low practical specific capacity against theoretical capacity of 1675 mAhg⁻¹ and high self-discharge rate prohibits the commercialization of lithium-sulfur batteries. [40] Since Abraham [47] and Peled [48] started to develop this system in the early 1980s, many attempts have been made to understand the electrochemical mechanism and overcome the disadvantages.

1.3.1 Fundamental chemistry of Li-S batteries

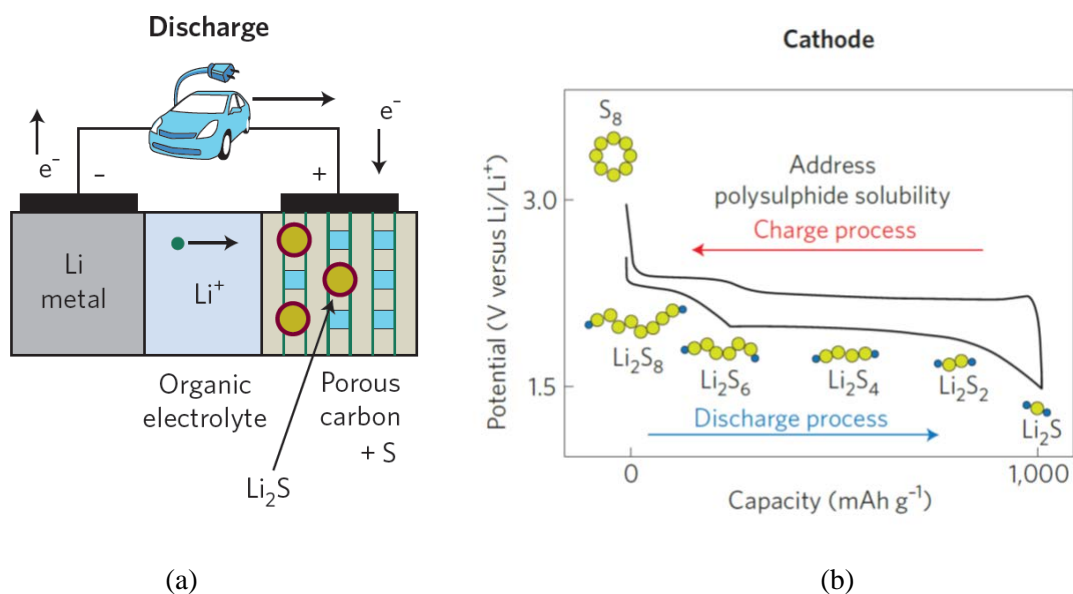


Fig. 1.6 Typical model (a) and charge/discharge curves (b) of lithium-sulfur batteries. Reprinted from [49].

Copyright 2011, with permission from Nature Publishing Group.

The rechargeable lithium-sulfur battery is composed of lithium metal as the negative electrode and sulfur as the positive electrode, as shown in Fig.1.6a [49]. Sulfur in this system delivers

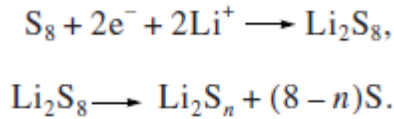
a theoretical capacity of 1675 mAhg⁻¹ by the process of non-topotactic ‘assimilation’ through the redox reaction described as below:



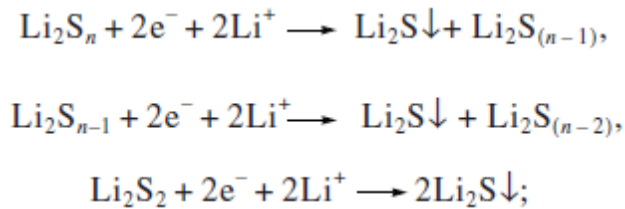
Where the potential is ~ 2/3 of that can be delivered by the conventional cathode, lies near 2.2 V (vs Li⁺/Li). Hence, if assuming complete reaction to Li₂S, the theoretical energy density of Li-S batteries could reach 2,500Wh kg⁻¹ or 2,800Wh L⁻¹, which is based on a weight or volume respectively. [38-60]

1.3.2 Discharge process

In Li-S battery, there are two stages in a typical discharge/charge process (Fig.1.6b), associated with oxidation and reduction reaction respectively. In the first discharge stage, within the potential range of 2.5–2.0 V (vs Li⁺/Li) , the elementary sulfur is dissolved in the electrolyte and forms lithium octsulfide which is soluble in the organic electrolyte. the reaction is described below in a simplified form. [51-55]



In the second stage, the long chain polysulfides are further reduced and eventually produce insoluble Li₂S through a series complex reaction process. One of the schemes suggested by Kolosnitsyn [51] is described below:

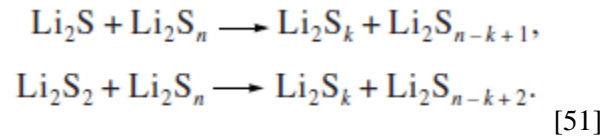


From Barchasz’s observation [60], the discharge mechanism involved in Li-S cells depends on the electrolyte used in the system. They proposed a mechanism with 3 stages coupled with disproportionation and electrochemical reactions, and observed the passivation of the positive electrode at

the end of the discharge due to the precipitation of insoluble Li_2S_2 and Li_2S , which limited the utilization of sulfur active material and the discharge capacity.

1.3.3 Charge Process

The charge process also has two stages. First, the long-chain lithium polysulfides- Li_2S_n is leading to medium-chain polysulfides- Li_2S_k by reacting with insoluble Li_2S .



When the insoluble lithium polysulfide Li_2S are fully consumed, the second stage of the reaction starts, where long-chain lithium polysulfides are leading to elementary sulfur by reduction. The potential of this plateau is around 2.4-2.6 V (vs Li^+/Li).



Where $(mn) = (m-1)((n-k)+1)$. [51]

1.3.4 Shuttle mechanism

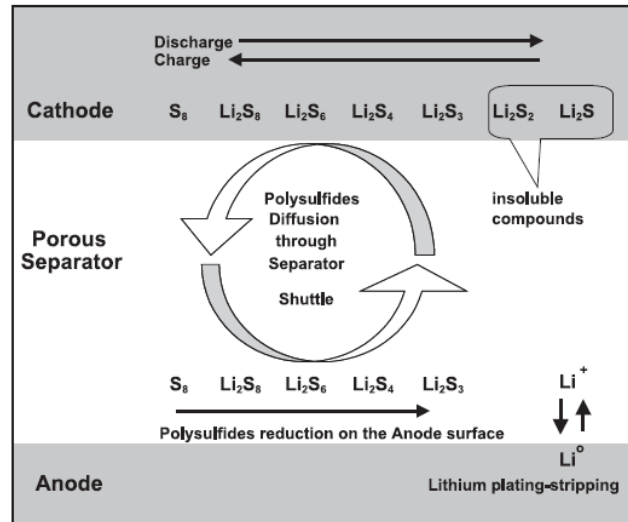
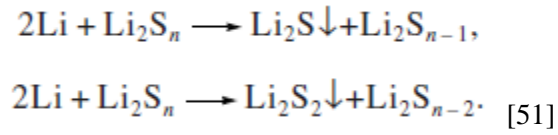
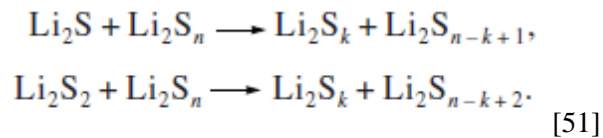


Fig. 1.7 Process of polysulfides shuttle. Reprinted from [57]. Copyright 2004, with permission from Elsevier.

The shuttle mechanism is schematically shown in Fig. 1.7. It can be described: the soluble long chain lithium polysulfides in organic electrolyte can diffuse through separator to the anode and be reduced to short-chain polysulfides and insoluble Li_2S_2 and Li_2S by lithium metal during the following oxidation process; the short chain polysulfide may then move back toward the cathode side and be reoxidized to long-chain.



As well known in lithium-ion batteries, dendrite is an essential problem of lithium metal anode during charge/discharge, which can cause serious safety problems. The reaction by long-chain polysulfide and lithium anode results in the deposition of insoluble Li_2S_2 and Li_2S on the surface of lithium anode. These insoluble sulfide products creating dense surface layers. As a result of the low reactivity of these sulfides which are electrical insulating, it retards the electron transfer between metallic lithium and electrolyte system. As a result of the reaction between dendritic lithium and long-chain polysulfide, the dendrite formation is limited. However, the active sulfur component is decreasing in the system due to the precipitation of Li_2S_2 and Li_2S on the anode. Consequently, battery capacity is fading during cycling, and the decreasing rate is proportional to the deposition rate of insoluble Li_2S_2 and Li_2S on the anode. Additionally, by reacting with long-chain lithium polysulfides, the precipitated Li_2S_2 and Li_2S can be transformed to medium-chain lithium polysulfides which are soluble in the electrolyte.



The active sulfur component in the system is related to two processes, one is the deposition of Li_2S_2 and Li_2S , the other one is their dissolution to the electrolyte. The capacity decreasing rate of this cell depends on the combined effects of formation and dissolution rate of Li_2S_2 and Li_2S on the anode side. [51-60]

Anode

Problems of Li metal

- Dendrite formation
- Cycling efficiency
- Requires stable solid-electrolyte interphase
- Safety issues
- Formation of insulating Li_2S layer on Li anode



Fig. 1.8 Problems of the lithium anode. Reprinted from [49]. Copyright 2011, with permission from Nature Publishing Group.

In general, despite the advantage of rechargeable lithium-sulfur battery such as high capacity, low cost and environment friendly, the highly ionically and electrically insulating nature of sulfur and Li_2S severely restricts the sulfur cathode to achieve good cycling stability with high power density. It is necessary to maintain sulfur in a good electrically and ionically conductive environment to allow the reversible electrochemical reaction and achieve high capacity especially at high rates charge/discharge process. [38] Moreover, the deposition of Li_2S_2 and Li_2S on the cathode results in the passivation of the positive electrode, causing the early end of discharge. [60] With the Lithium metal anode, dendrite formation could cause serious safety issues. The ‘shuttle mechanism’ leads to serious lithium anode corrosion and fast capacity fading in the cell (Fig.1.8), as well as a low cycling efficiency. [49-51]

Chapter 2

Cathode Materials for Lithium-Sulfur batteries

The rechargeable lithium-sulfur battery with its high capacity, low cost and environment friendliness has drawn much attention in recent years. However, sulfur and sulfur-containing organic compounds are electrically and ionically insulating, leading to low sulfur utilization. [61] Furthermore, the insoluble Li_2S accumulated on the surface of cathode becomes electrochemically irreversible during cycling. [62] Additionally, the 'shuttle mechanism' leads to the decrease of cathode active material resulting in extensive capacity degradation during cycling process, [63] in which soluble polysulfides formed in the cathode side diffuse to the anode and then diffuse back to the cathode by a series of reactions. These detrimental factors severely restrict the sulfur cathode to achieve high power density and good cycling stability.

To overcome the aforementioned problems, approaches have been employed in attempts including protective films for the lithium anode, new electrolytes and electrolyte additives have brought out some encouraging results. However, in the cathode part where sulfides are solubilized still needs breakthroughs which are the difficult part.[64] This work will focus on the cathode. In order to control the solubility of sulfides and improve the electrode conductivity, sulfur-carbon composites rather than simple sulfur-carbon mixtures has been proved to be an efficient method, such as encapsulating elemental sulfur in mesoporous carbon or carbon nanotube. Based on the high electrical conductivity and high surface area of graphene, sulfur-graphene composites also show some attractive results. Efforts by embedding elemental sulfur in conducting polymers or forming chemical bond between sulfur and conducting polymer have also shown some great improvements. Based on the concept to replace reactive lithium metal anode with more reliable materials such as silicon-carbon anode and tin-carbon anode in this technology, which requires the cathode to become the lithium-ion source, researchers developed a Li_2S -carbon composite instead of common sulfur-carbon composite.[64-66]

2.1 General requirements of cathode materials for lithium sulfur batteries

Based on the problems discussed before, in order to achieve high energy density as well as long cycling lithium sulfur batteries, the requirements for cathode material are listed as below:

- Good electrical and ionic conductivity
- Good distribution of active material
- High loading of active mass of sulfur
- Efficient binding or adsorbing ability of soluble polysulfides
- Flexibility to handle volume change during charge/discharge
- Relative high operating voltage for high energy density
- Stable structure during charge/discharge
- Forming stable and thin SEI on the surface
- Less irreversible reactions

2.2 Microporous/mesoporous carbon material

Porous carbon materials have drawn a lot of attention as a result of their large pore volumes, high surface area, chemical inertness and good thermal and mechanical stability. These type of porous carbons materials are widely applied as adsorbents in industry. They are used in gas separation, storage of natural gas, catalyst support, chromatography columns and use for electrodes of fuel cells, lithium-ion batteries and electrochemical double layer capacitors. [67, 68]

Based on the pore sizes, porous carbon materials can be categorized into three types, (International Union of Pure and Applied Chemistry (IUPAC) recommendation) [67] :

- Microporous, pore size < 2 nm,
- Mesoporous, $2 \text{ nm} < \text{pore size} < 50$ nm,
- Macroporous, pore size > 50 nm.

In order to overcome the problems of lithium sulfur batteries as discussed before, porous carbon which can be a host to encapsulate the active materials and as a conducting framework has been explored. Microporous carbon with small pore size has been recently reported to be a good method to

solve the dissolution problem, which brings good cycling stability, but on the other hand, it creates poor rate characteristics and shows low sulfur content. However, for mesoporous carbons which have larger pore size, it is possible to obtain high rate performance due to the rapid diffusion, but it is difficult to attain the cyclability, because of the low restriction of the extensive dissolution of intermediate polysulfides into the electrolyte during charge and discharge process. In order to attain practical high ‘C’ rate cells with high capacity and without capacity fading in such porous carbon /sulfur systems where the sulfur is hold within the carbon cathode, the pore size distribution, pore volume, surface area, carbon structure, conductivity of the porous carbon could all be important factors. [69]

2.2.1 Mesoporous carbon

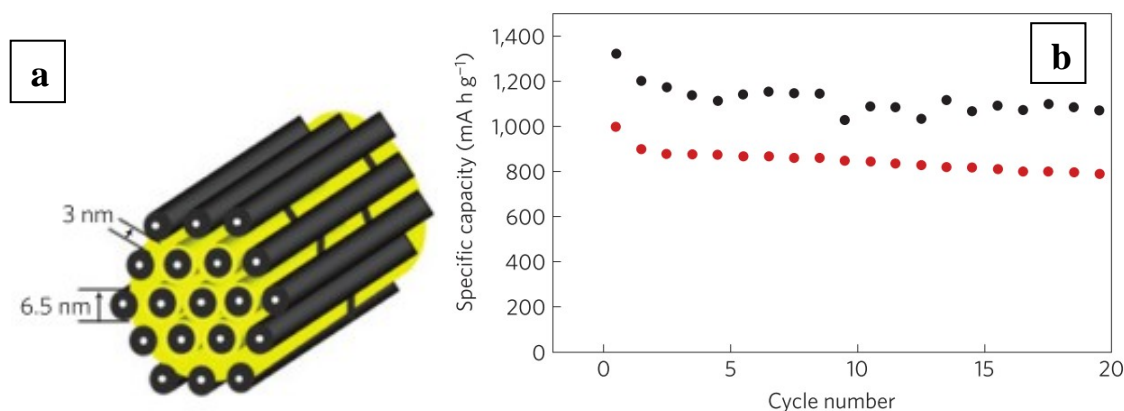


Fig. 2.1 (a) Schematic diagram of the sulfur/mesoporous carbon composite, in which sulfur (yellow) is confined in mesoporous carbon CMK-3, (b) Cycling performance of CMK-3/S-PEG (black) and CMK-3/S (red) at 0.1 C rate. Reprinted from [70]. Copyright 2009, with permission from Nature Publishing Group.

Nazar reported [70] a CMK-3/sulfur composite (Fig.2.1a) with up to 70% sulfur can be filled into CMK-3. CMK-3 with an interconnected pore structure is a well-known mesoporous carbon which is formed from carbon rods with uniform size organized in a hexagonal pattern. [67] It's reported that CMK-

3 exhibited a large specific surface area of about $1976 \text{ m}^2 \text{ g}^{-1}$ and total pore volume of about $2.1 \text{ cm}^3 \text{ g}^{-1}$. It possess a primary pore size of about 3.33 nm , and conductivity of about 0.20 S cm^{-1} . It ensures the intimate contact of highly electrical conducting carbon and insulated sulfur, which is significantly to achieve high utilization of active material, as a result, up to 80% sulfur utilization and a reversible capacity of up to 1320 mAh g^{-1} at a current rate of $C/5$ (a current density of about $334 \text{ mA g}_{\text{sulfur}}^{-1}$) was achieved. The mesopores of CMK-3 benefits the constraint of the dissolved polysulfide species. The cyclability of the cells is improved with the help of surface polymer modifier. However, only 20 cycles of the cycle life is reported, Fig. 2.1b. It is still a challenge to achieve high capacity without capacity fading.

2.2.2 Microporous carbon

In the purpose to improve the cyclability of high energy lithium sulfur batteries by solving the problems caused by the dissolution of polysulfide species into the electrolyte, Gao [71] reported a microporous carbon/sulfur composite which was achieved through thermal treatment of carbon mixture and sublimed sulfur. As a result, sulfur is ‘encapsulated’ into the micropores. The carbon spheres possess a narrow size distribution of about 0.7 nm with a large specific surface area of $843.5 \text{ m}^2 \text{ g}^{-1}$ and pore volume of $0.474 \text{ cm}^3 \text{ g}^{-1}$. Sulfur is highly dispersed in the carbon sphere, which ensures intimate contact between the carbon frame and sulfur. Due to the small pore size of 0.7 nm , the intermediate reaction species are well confined inside the narrow micropores which greatly suppress the shuttle of polysulfides. Additionally, sulfur in the micropores exist in a linear chain configuration with smaller size rather than in a crown rings configuration. Therefore, high sulfur utilization and excellent cyclability of the composite is achieved. The composite with 42 wt% sulfur content shows a reversible capacity of about $800 \text{ mAh g}_{\text{sulfur}}^{-1}$ and a capacity of about $650 \text{ mAh g}_{\text{sulfur}}^{-1}$ can be maintained after 500 cycles at current density of 400 mA g^{-1} . As a result of the strong adsorption of micropores, the electrochemical reaction is confined inside the carbon sphere, which greatly subdues the polysulfide shuttle, and ultimately benefits the enhancement of cyclability. However, the ion diffusion and volume change of active materials inside the micropores during charge and discharge would be a problem, which might be a reason why the reversible capacity of sulfur is not high compare to the theoretical capacity of sulfur (1672 mAhg^{-1}). Moreover, due to pore

volume limitation, the sulfur content was constrained. In the report, the composite with 55% sulfur shows much lower capacity comparing with the composite with 42% sulfur content at a very low c-rate.

2.2.3 Bimodal Carbon

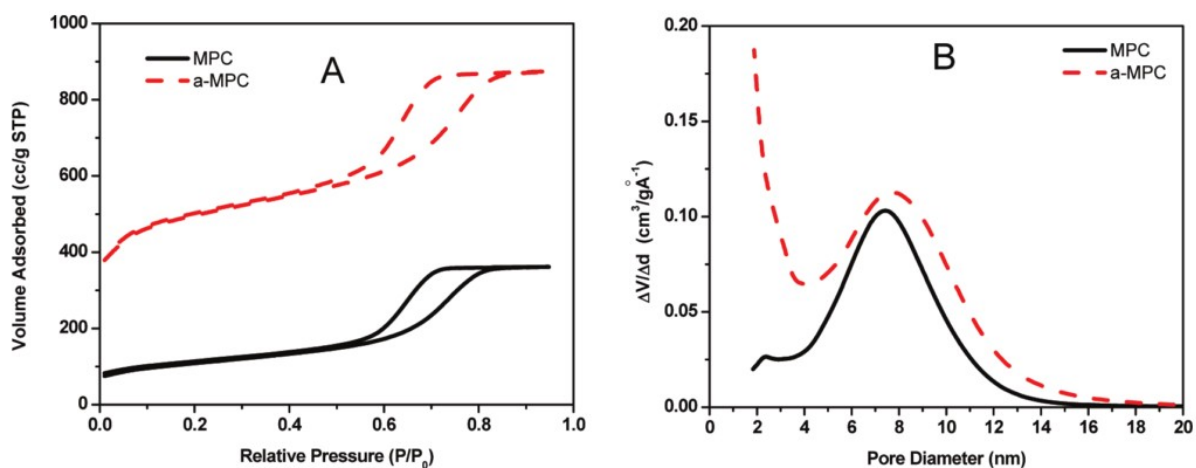


Fig. 2.2 N₂ adsorption/desorption characterization of mesoporous carbon (MPS) and KOH activated mesoporous carbon (a-MPS) : (A) isotherms at 77K; (B) pore size distribution. Reprinted from [72]. Copyright 2009, with permission from American Chemical Society.

Liang [72] reported a bimodal hierarchically structured mesoporous carbon/sulfur composite. The porous carbon reveals a distribution of mesopores of 7.3 nm and micropores of less than 2 nm which is achieved by KOH activation, the BET results are shown in Fig. 2.2. The carbon/sulfur cathode presents 94.6 % sulfur utilization ($1584 \text{ mA h}_{\text{sulfur}}^{-1}$) at high current density of 2.5 A/g and significantly improved cyclibility when the sulfur content is less than 12 wt% in the carbon. The creation of micropores is essential for polysulfide adsorption and suppressing their shuttle, while the large pores contribute to the ion diffusion for high rate charge/discharge. Despite the low loading of

active material (less than 12 wt%), this work shows the bimodal structured carbon is a promising approach for lithium sulfur batteries.

With the aim to further improve the application of bimodal carbon materials for high performance lithium sulfur batteries, it is necessary to optimize the bimodal structure of this type of carbon with regards to pore size distribution, pore volume, surface area and also the contribution of small pores to total pore volume and surface area. He, *et al.* [69] report a new bimodal mesoporous carbon (BMC-1) based on the modification of MPC-36 (surface area of $2130 \text{ m}^2\text{g}^{-1}$, pore size distribution of 2.6 nm and 5.8 nm, pore volume of $2.0 \text{ cm}^3\text{g}^{-1}$ [73]) which has better small mesopore distribution. BMC-1 shows a large BET surface area of $2300 \text{ m}^2\text{g}^{-1}$ with pore size distribution around 2.0 nm and 5.0 nm, and total pore volume $2.0 \text{ cm}^3\text{g}^{-1}$ with a small pore volume of $0.95 \text{ cm}^3\text{g}^{-1}$. The unique structure of BMC-1 renders it a suitable host for sulfur as the cathodes of Li-S batteries. BMC-1/S composite with 50 wt% sulfur content shows an initial capacity of 995 mAh g^{-1} at a current rate of 1675 mA g^{-1} (1C). After 100 cycles, the capacity is maintained at 550 mAh g^{-1} . The large number of small mesopores is essential to suppress the polysulfide shuttle while the interconnection of small pores and large pores enables the diffusion of lithium ions and polysulfide anions. [69]

2.2.4 Carbon material with unique structure

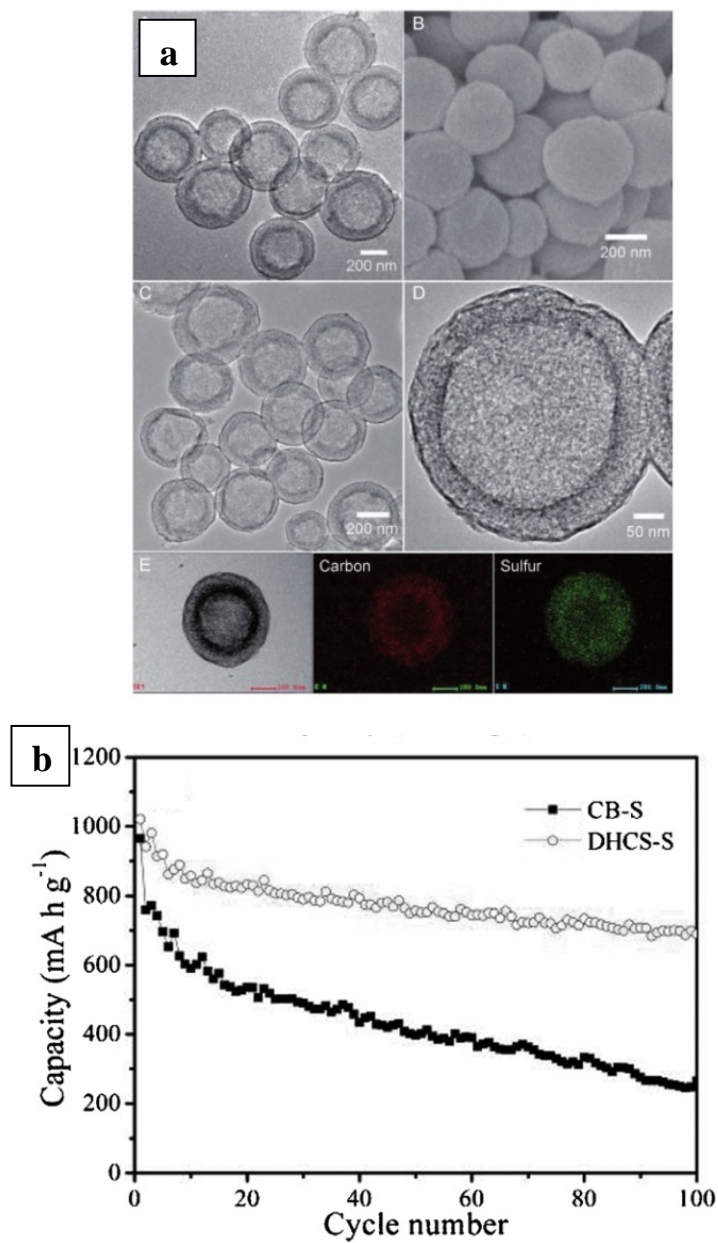


Fig. 2.3 (a) A) TEM and B) FESEM image of double-shelled hollow carbon spheres (DHCSs). (C, D) TEM images of the sulfur-DHCS composite. E) TEM image and elemental mapping of a single sulfur-DHCS sphere, (b) Cycling performance of carbon black-sulfur (CB-S) composite and DHCS-S composite at 0.1 C rate. Reprinted from [74].

Copyright 2012, with permission from WILEY-VCH Verlag GmbH & Co. KGaA, Weinheim

Guo, [74] *et al* report a double-shelled porous carbon spheres (DHCSs) as the scaffold for sulfur as the cathodes of lithium sulfur batteries. These hollow carbon spheres reveal two thin and concentric shells with carbon connection links between the two shells and the distance between them is around 50–100 nm, as shown in Fig.2.3a. The DHCS sample is proved to have a highly porous structure within the shells, which possess a total BET pore volume of $1.685 \text{ cm}^3 \text{ g}^{-1}$ and a specific surface area of $748 \text{ m}^2 \text{ g}^{-1}$. The DHCS/S composite presents an initial capacity of about $1050 \text{ mAh g}_{\text{sulfur}}^{-1}$ and a reversible capacity of $690 \text{ mAh g}_{\text{sulfur}}^{-1}$ after 100 cycles at 0.1 C (current density of 167.5 mA g^{-1}), Fig. 2.3b. It also shows improved high rate performance. The double shell structures of the hollow carbon spheres could result in a relatively high load amount of active, subdue the diffusion of polysulfides to the anode and maximize the advantages of porous carbon materials.

In summary, porous carbon material are a very promising approach for achieving high and retainable energy density of lithium sulfur batteries. A high amount of sulfur can be loaded which is essential to achieve high energy density. However, generally the capacity of this type of cathode is not very high which means a relatively low sulfur utilization, it is more obvious when the sulfur content is higher. Moreover, even though the cyclability is significantly improved, but the fading of capacity is still a big problem of the application of Li-S batteries.

2.3 Carbon nanotube

Carbon nanotubes (CNTs) belong to the fullerene structural family which is in a cylindrical nanostructure. The walls of CNTs are formed by a one-atom-thick carbon sheets named graphene rolled at discrete and specific angles in a long and hollow structure. The properties of the nanotube depend on the balance of the radius and rolling angle; for instance, semiconductor or metal of the individual nanotube shell. There are two types of nanotube, multi-walled nanotubes (MWNTs) and single-walled nanotubes (SWNTs). Individual nanotubes are not easy to be dispersed, they naturally aggregate together and form "ropes" by van der Waals forces and pi-stacking. Carbon nanotubes have some attractive properties for nanotechnology, electronics and material science and have been applied

to various structural materials, due to their unusual electrical and thermal conductivity, and mechanical properties. [76]

The carbon nanotubes have also attracted researcher's attention for its application in lithium sulfur batteries, due to its great electrical conductivity. They can build up effectively conductive network, which is better than other carbon conductors, such as graphite, acetylene black (AB) and carbon black (CB). The surfaces properties of CNTs can be modified to ensure their dispersion and interaction with solvent, and feasibility for grafting of functional groups and nanoparticles.

2.3.1 Sulfur coating on CNTs

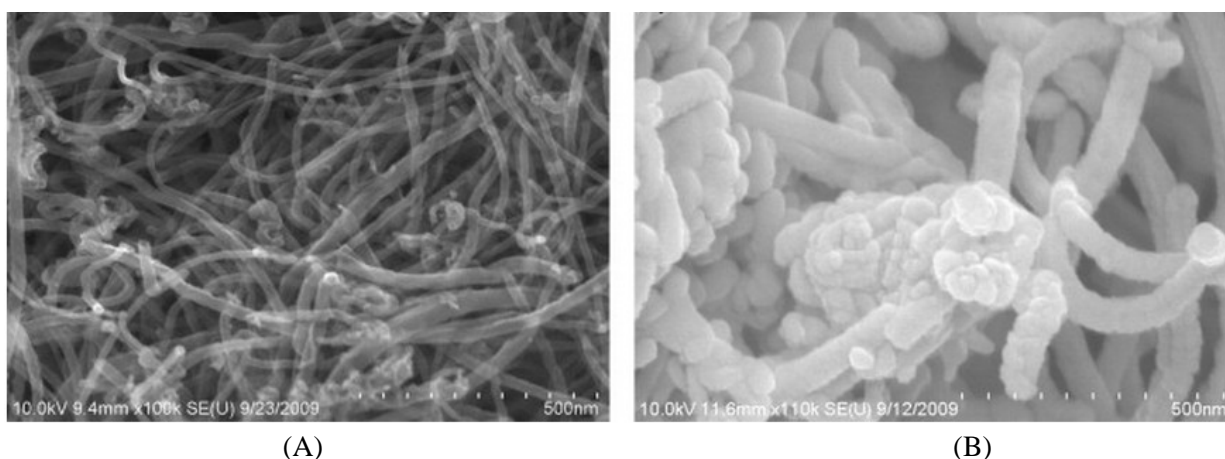


Fig. 2.4 Scanning Electron Microscopy (SEM) images of (A) MWCNTs and (B) nano-sulfur/MWCNTs composite. Reprinted from [77]. Copyright 2010, with permission from Elsevier.

Zheng [77] synthesized sulfur/MWCNTs composite with the deposition of sulfur on MWCNTs for Li/S batteries. The modified MWCNTs are dispersed in water with surfactant; sulfur is deposited on surface of carbon nanotube through solvent exchange method based on solubility difference of sulfur in different solvents. The SEM images of the MWCNTs and the nano-sulfur/MWCNTs composite are shown in Fig. 2.4. The composite shows a reversible capacity of 1210 mAh g_{sulfur}^{-1} at current density of 300 mAh g^{-1} , but it decreases to 810 mAh g_{sulfur}^{-1} after 30 cycles. The modified MWCNTs are supposed to be a conductor and also a matrix for sulfur, and it confirms that the modified MWCNTs than the other carbon materials like CB, AB and graphite for sulfur cathode.

However, the capacity of this cathode decreased pretty fast even though it showed good sulfur utilization at the beginning, which indicates that the shuttle of polysulfides is still a big problem.

As a result, Zheng's group [78] introduced porous structure to the S/MWCNT system in their later work. Through the same method, elemental sulfur was deposited on the surface of modified MWCNTs with a sulfur layer of 10–20 nm thickness. The S/MWCNT is in a typical core–shell structure. The porous sphere and interwoven structure is achieved through ball mill of the intermediate composite. The pore sizes of the final S/MWCNT composite is around 1 μm to 5 μm, which is pretty large compared with micro/mesoporous structure of most sulfur/carbon materials. However, with the additive of LiNO_3 in the electrolyte, the composite also shows high sulfur utilization and significantly improved cycle life. It shows a reversible capacity of 1000 mAhg^{-1} after 100 cycles at a current density of 0.3 Ag^{-1} , which indicates great improvement of the cyclability compared with their previous results. The unique hierarchical structure of the S/MWCNT composite is able to provide ion transport path and support more volume change and restrain electrolytes within the composite suppressing the shuttle effect. Furthermore, the interwoven architecture of MWCNT forms good framework for electron transport. LiNO_3 as additive in the electrolyte helps reduce the shuttle effect. However, it also indicates that the large pore size and hierarchical structure of the S/MWCNT is still not good enough to provide high retainable capacity for lithium-sulfur batteries.

In summary, CNTs could form interwoven structure and dramatically improve the electron conductivity of the electrode and hence improve the utilization of sulfur, however, it could not help too much on suppressing the shuttle effect due to the diffusion of dissolved polysulfides in the electrolyte. As a result, it is limited to achieve better cyclability of these types of cathodes.

2.3.2 Sulfur impregnated into CNTs

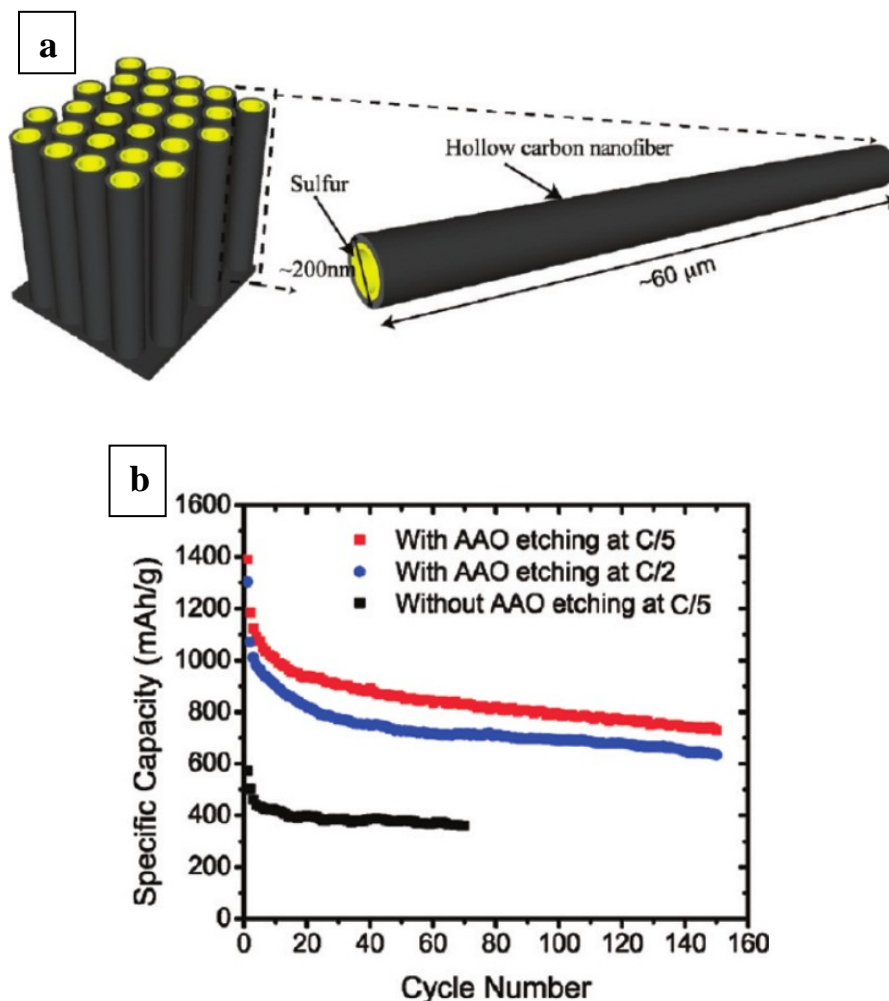


Fig. 2.5 (a) Schematic of sulfur/ hollow carbon nanofibers composite structure, (b) Cycling performance.

Reprinted from [79]. Copyright 2011, with permission from American Chemical Society.

Cui's report [79] point out that porous carbon in a case could provide intimate contact of sulfur and the conductor, and constrain polysulfides within the electrode; however, the particle size of porous carbon is too large, around micrometer scale, which still exposes a large surface area of sulfur to the electrolyte. As a result, the polysulfides dissolution is still substantial. "The characteristics of

the sulfur electrode structure are proposed as follows: (i) a closed structure for constraining polysulfides; (ii) limited contact area of sulfur and electrolyte; (iii) enough pore volume and flexibility to accommodate volume change during charge and discharge from sulfur to Li_2S_2 and Li_2S ; (iv) short electron and ion pathway to provide good electrical and ionic conductivity (v) large surface area for intimate contact of carbon and sulfur, and carbon and $\text{Li}_2\text{S}_2/\text{Li}_2\text{S}$; (vi) appropriate additives to the electrolyte to suppress the polysulfide shuttle. ” Based on the proposal, they impregnated sublimed sulfur into vertical arrays of carbon nanotube in order to effectively constrain polysulfides and achieve high specific capacity and cyclability of the cells. The hollow carbon nanofiber arrays were synthesized through carbonization of polystyrene coated on anodic aluminum oxide (AAO) template. Sublimed sulfur is impregnated into the carbon coated AAO pores, and at the end, AAO template is etched. The AAO templates ensure sulfur is coated on the inner wall but not the exterior wall. The diameters of the carbon fibers ranges from 200 to 300 nm with the length up to 60 μm , as shown in Fig.2.5a, sulfur is encapsulated inside the hollow carbon nanofibers. With addition of LiNO_3 in the electrolyte, the composite presents an initial reversible capacity of 1200 $\text{mA g}_{\text{sulfur}}^{-1}$ at C/5 rate; after 150 cycles, the capacity can be maintained at about 730 $\text{mA g}_{\text{sulfur}}^{-1}$, Fig. 2.5b. The electrochemical results demonstrate high sulfur utilization and greatly enhanced cyclability. The hollow structure of nanotubes is essential to constrain polysulfides and also provide intimate contact for the carbon wall and sulfur. The hollow structure of carbon nanofiber is essential in guaranteeing high retainable specific capacity of the sulfur cathode in Li/S batteries. [79]

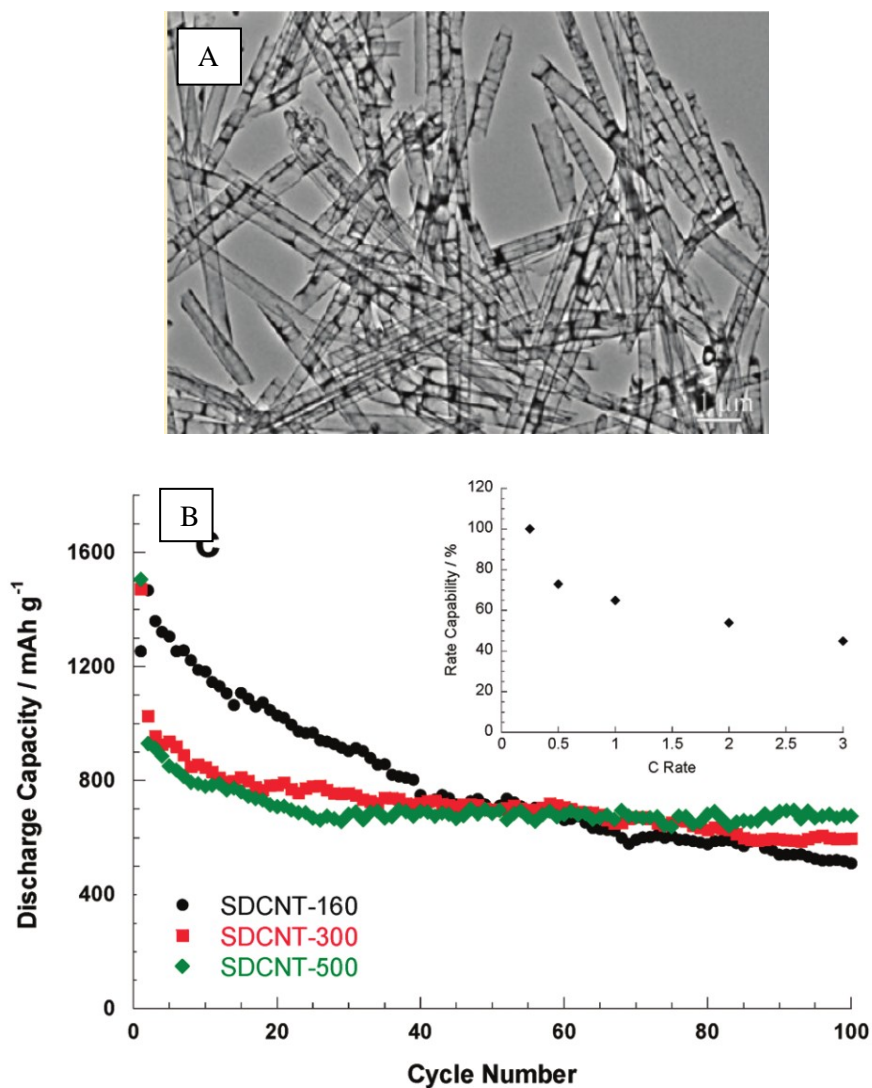


Fig. 2.6 (A) SEM images of the disordered carbon nanotubes synthesized *via* the template wetting method. (B) Cycling performance of SDCNT-160, SDCNT-300, and SDCNT-500, which was heated at 160 °C, 300 °C, 500 °C respectively. Reprinted from [80]. Copyright 2011, with permission from American Chemical Society.

Different from Cui's design of applying carbon nanofibers array, Wang [80] took advantages of disordered carbon nanotubes (DCNTs). The DCNTs are fabricated by a template wetting technique using AAO membranes; the morphology of DCNTs is shown in Fig. 2.6A. Sulfur is impregnated into

DCNTs at a much higher temperature of 500 °C in vacuum to make sure the intercalation of sulfur into carbon pores and graphite layers. The SDCNT-500 cathode shows an initial capacity of around 900 mAh g_{sulfur}⁻¹, and demonstrates 72.9% capacity retention after 100 cycles, Fig. 2.6B. The sulfur-impregnated DCNTs composite presents significantly improved coulombic efficiency and cyclability as the cathode materials for Lithium-Sulfur batteries. The impregnation of sulfur at high temperature in a vacuum environment is the key for the improvements, because the vaporized sulfur is believed to intercalate into smaller pores and the graphite layers of carbon. Hence, it limits the contact surface area of sulfur and electrolyte. In addition, sulfur in the smaller voids is no longer in a ring-crown S₈ state, but exist in small molecules like S₆ or S₂. [80]

In summary, it is more significant for achieving high retainable capacity of lithium-sulfur batteries by impregnating sulfur into carbon nanotubes compared with just coating sulfur on the exterior wall of CNTs.

2.4 Graphene

Graphene has a two-dimensional, one-atom-thick nanosheet structure with high surface area and high conductivity and has been introduced in lithium sulfur battery as substrate and conductor. Reduced graphene oxide sheets (RGO) are highly conductive, but easily aggregate making it difficult to disperse in aqueous solution. Conversely, the un-reduced graphene oxide sheet (GO) can be easily dispersed but has low electronic conductivity.

Zhang [81] reports a saccule-like sulfur/RGO composite which is fabricated within oil in water (O/W) system. GO dispersed in aqueous solution is mixed with Sulfur dissolved in CS₂ solvent under sonication. CS₂ is evaporated subsequently and GO is reduced afterwards. Small sulfur particles ranged from 10 nm to 100 nm is encapsulated by RGO and form a large particle with a saccule-like structure. The composite presents excellent high rate performance. It shows a capacity of 697.5 mAhg_{sulfur}⁻¹ at a high rate of 4C, which can be maintained at about 478.7 mAhg_{sulfur}⁻¹ after 60 cycles. As a result of the high electrical conductivity of reduced graphene oxide and the saccule-like

structure of the composite, it provides intimate contact between sulfur and graphene, and effective electrically conductive network. The volume change of sulfur during the charge and discharge could be a problem of this composite.

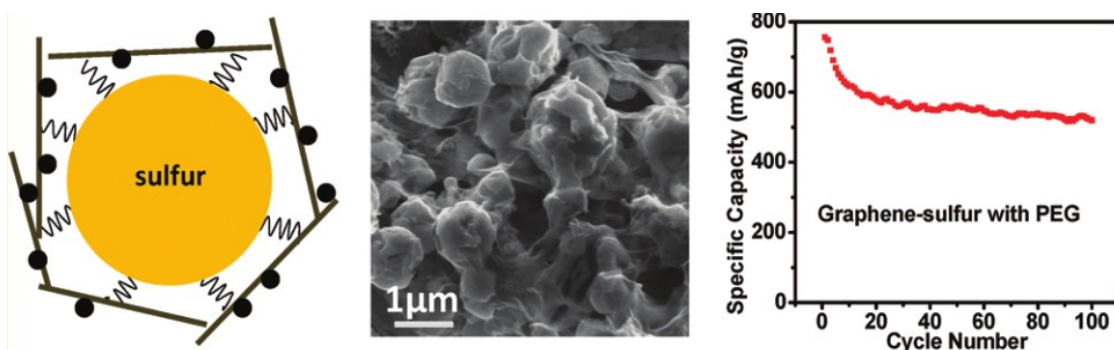


Fig. 2.7 Schematic structure of the graphene-PEG-sulfur composite, SEM image of the composite and the cycling discharge capacity. Reprinted from [82]. Copyright 2011, with permission from American Chemical Society.

With similar ideas, Cui's group [82] designed a more complicated system. Basically, sulfur particles are wrapped by reduced graphene oxide sheets with carbon black and polyethylene glycol (PEG) in between, as shown in Fig.2.7. PEG works as surfactant when micro-sized sulfur particles are synthesized first. The composite shows an initial capacity of about $750 \text{ mAhg}_{\text{sulfur}}^{-1}$ with 87% capacity retention within the last 90 cycles at C/5 rate, which shows significantly improved cyclability. It also presents better cyclability at C/2 rate with 91% retention within the last 90 cycles because of the lower polysulfide shuttle effect at higher current density. It is proposed that the existence of PEG is essential to grant the greatly improved cyclability of the sulfur/graphene composite by offering a flexible buffer to sustain the volumetric expansion. Moreover, PEG chains has the function of constraining polysulfides, and the carbon black decorated graphene sheets provide intimate contact with sulfur particles improving the electrical conductivity of the electrode.

The above two reports showed that sulfur was in micrometer scale. The large size could limit the sulfur utilization and rate performance due to the diffusion difficulties of ions and electrons. Hence, it's important to minimize the size of sulfur particles or the thickness of sulfur layers.

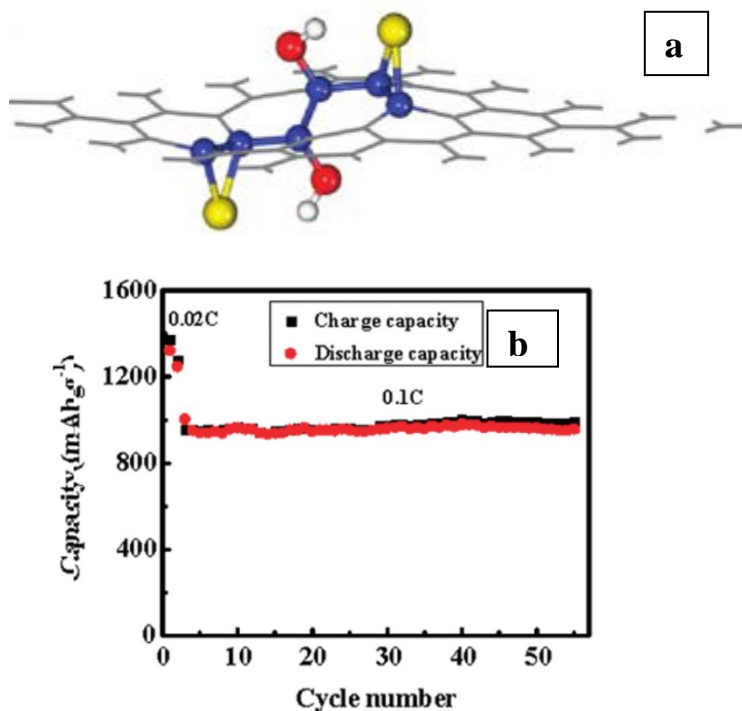


Fig. 2.8 (a) Representative pattern of GO immobilizing S. Yellow, red, and white balls denote S, O, and H atoms, respectively, while the others are C atoms. (b) Cycling performance of the graphene-sulfur composite at a constant current rate of 0.1C, the first two cycles are processed at 0.02C for activation. Reprinted from [84]. Copyright 2011, with permission from American Chemical Society.

In Sun's work [83], expanded graphite consisting of graphene nanosheet first synthesized through electric heating and reduction by H₂ at high temperature. Sulfur was embedded into the interleaved EG host *via* melt-diffusion strategy. The morphology test reveals that the composite is in a layer-by-layer structure. Sulfur particles with a size less than 100 nm are anchored on the surface of graphene. The S-EG composite with 60% sulfur content shows an initial capacity of 1210.4 mAhg_{sulfur}⁻¹ and 957.9 mAhg_{sulfur}⁻¹ at current density of 280 mA g⁻¹ and 28 mA g⁻¹ respectively. At the lower rate, the capacity can still be maintained at 879.5 mAhg_{sulfur}⁻¹ after 70 cycles. The

multifunctional expanded graphite provides excellent electrical conductivity of sulfur for achieving high utilization. The layer-by-layer structure could constrain polysulfide with the electrode and afford flexibility for volume change of sulfur.

In order to get a thin and uniform coating of sulfur on graphene, Zhang [84] used a chemical deposition strategy to immobilize sulfur on graphene oxide with the reactive functional groups of graphene oxide as the anchor sites. Sulfur was deposited on graphene in microemulsion system with size around 10 nanometers, followed by heat treatment at 155 °C in order to make melt sulfur diffuse into the graphene oxide pores. The active functional groups on graphene oxide have strong adsorption to immobilize sulfur and polysulfides (Fig.2.8a). This strong interaction effectively constrains polysulfides from dissolution into electrolytes. The composite presents an initial reversible capacity of 1400 mAhg_{sulfur}⁻¹, and stable capacity of 950 mAhg_{sulfur}⁻¹ which was kept for about 60 cycles at a rate of C/10 in ionic liquid-based electrolyte, as shown in Fig. 2.8b. The composite also presents a good rate capability. The graphene sheets in the composite, which has an extremely high surface area and good conductivity, forms a good electron transport framework. The functional groups on graphene serves as immobilizers and provide intimate contact between sulfur and graphene, and also adsorb polysulfides. The flexibility of GO sheets enables the composite to afford volume changes of sulfur during charge and discharge.

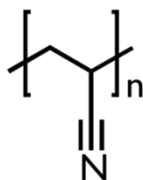
In summary, graphene with its high electrical conductive and surface area play a great role in achieving over all electrochemical performance of lithium-sulfur cells.

2.5 Conductive Polymer

Conductive polymers are a type of polymer that have electrical conductivity, which is also named as intrinsically conducting polymers.[85] Conductive polymers can deliver high electrical conductivity, some of them have high metallic conductivity and some of them are semiconductors, but generally they are not thermoplastics. Most of the conductive polymers consist of the linear-backbone so called polymer blacks, such as polypyrrole, polyaniline and polyacetylene, and their

copolymers. Conductive polymers have drawn much attention in printing electronic circuits, batteries, supercapacitors, solar cells, biosensors and chemical sensors, flexible transparent displays, organic light-emitting diodes, electromagnetic shielding. [86] With the increasing progress in getting processable conducting polymers which have lower cost, better physical and electrical properties, they are thought to be promising in new applications. They can be synthesized with various nanostructures possessing higher surface area, smaller size, and better dispersability; and also can be immobilized, drafted, and modified with other materials for particular applications. Due to their high conductivity and processable advantages, conductive polymers are also attractive for high performance lithium-sulfur batteries, through the construction of possible nanostructures, or chemical bonds with active materials. Polyacrylonitrile, polyaniline and polypyrrole are the main type of conductive polymers that have been reported in the application of lithium-sulfur batteries.

2.5.1 Polyacrylonitrile



The chemical structure of the polyacrylonitrile repeat unit

Polyacrylonitrile (PAN) with the linear formula $(C_3H_3N)_n$ is a semicrystalline organic polymer. It melts above 300 °C, but it degrades before melting. PAN can be synthesized through free radical polymerization and anionic polymerization of Acrylonitrile (AN). It is widely used in developing of carbon fiber through stabilization, carbonization, and graphitization process. It has to be mentioned that through the stabilization process in a temperature range of 200 °C to 300 °C, the PAN fiber is oxidized and converted from thermoplastic to a non-plastic cyclic or a ladder compound. [87]

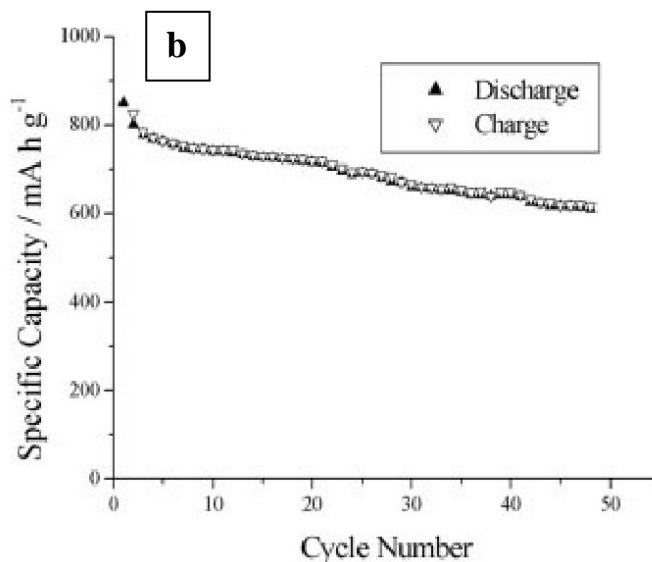
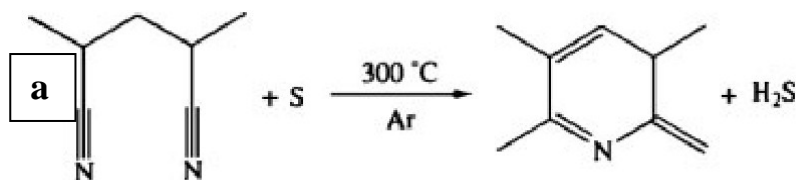


Fig. 2.9 (a) PAN dehydrogenated by sulfur, (b) Cycling performance of the PAN-sulfur composite with 54 wt.% sulfur content. Reprinted from [88]. Copyright 2003, with permission from WILEY-VCH Verlag GmbH & Co. KGaA, Weinheim.

[88] Based on these properties, Wang and his group developed a PAN-sulfur composite material for lithium-sulfur batteries. The mixture of PAN and sulfur is heat treated at 300 °C for couple of hours. As shown in Fig. 2.9a, PAN is dehydrogenated by sulfur. During this process, a thermally stable heterocyclic compound is generated through cyclization of the -CN functional group, meanwhile, it produces a conductive backbone similar to polyacetylene; at the same time, Wang suggests that sublimed sulfur is embedded into the heterocyclic compounds. In the composite with lower sulfur content, sulfur exist in amorphous state indicating its fine dispersion with particle size less than 10 nm. The composite shows a discharge plateau at about 1.47 V at the first cycle, and the

plateau shifts to higher potential in the following discharges, and stabilizes at 1.85 V. The composite shows an initial specific capacity of 850 mAhg^{-1} . After 50 cycles, it decreases to about 600 mAhg^{-1} , as shown in Fig.2.9b. This work proved the feasibility of the application of PAN in lithium sulfur batteries. But the working mechanism of the PAN-sulfur compounds has not been deeply explored in previous work.

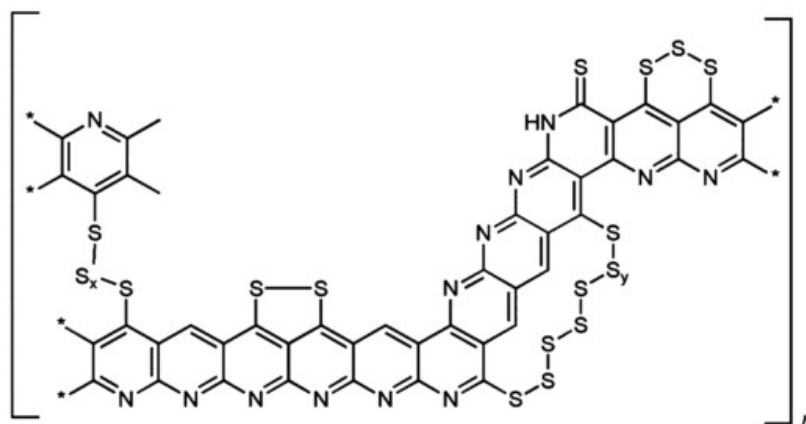


Fig. 2.10 Proposed structure of SPAN, containing all relevant functional groups ($0 < x < 6$; $y = 1,2$). Reprinted from [89]. Copyright 2011, with permission from American Chemical Society.

[89] Bunchmeiser and his group propose a structure related models of the electrochemistry of Sulfur-PAN composite for lithium-sulfur batteries based on experimental results, as shown in Fig. 2.10. Sulfur in the composite is bound to carbon in the PAN derived backbone with covalent bond, but not to nitrogen. Sulfur exists in the form of N-C-S , S_x ($x \geq 2$) and thioamide.

Based on this system, Wang developed several new composites by introducing MWCTs, graphene. In their recent work [90], a core-shell composite material was prepared. Polyacrylonitrile is deposited on the surface of MWCNT by in situ polymerization of acrylonitrile in MWCNT aqueous suspension. The mixture with sulfur is finally pyrolyzed at 300°C . MWCNTs in the composite forms a highly conductive network, and strengthen the stability of the electrode structure. After the

introduction of MWCNTs in the system, the discharge potential increases from 1.6 V to 1.8 V, suggesting lower electrical polarization. The composite presents an initial reversible capacity of 697 mAhg⁻¹, and it shows about 85% capacity retention after 50 cycles. MWCNTs are instrumental to suppress the electrochemical polarization and enhance the high rate performance of the cells for rechargeable lithium/sulfur batteries.

In summary, PAN shows good potential in the application of lithium sulfur batteries. But the sulfur/PAN composite has limiting sulfur content. The highest sulfur content as reported is no more than 55 wt%. If the sulfur content is too high, there will be sulfur existing in crystal form which is not bound with PAN backbone. The free sulfur could leads to significant capacity fading.

2.5.2 Polyaniline

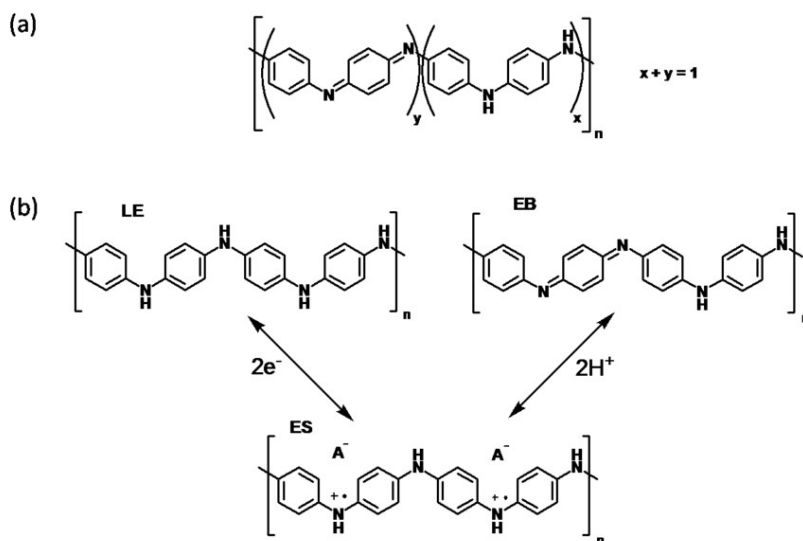


Fig. 2.11 (a) Generalized composition of PANI. The oxidation state is indicated by y which varies from 0 to 1. (b) Reversible doping and dedoping of PANI by i) redox processes between non-conducting leucoemeraldine (LE) and conducting emeraldine salt (ES), and ii) protonation reactions between non-conducting EB and ES. A⁻ denotes the dopant counterion in ES. Reprinted from [91]. Copyright 2011, with permission from American Chemical Society.

[91] Polyaniline (PANI) is a polymer with mixed oxidation states, which can be synthesized from the polymerization of aniline monomer. It has three different oxidation states as shown in Fig. 2.11. When $x=1$, it's called **leucoemeraldine (LE)**, which is completely reduced with a white or colorless color, the formula is $(C_6H_4NH)_n$. When $x=0.5$, it is called **emeraldine base (EB)**, which is half oxidized with a blue color, the chemical formula is $\{[C_6H_4NH]_2[C_6H_4N]_2\}_n$. When $x=0$, it is called **pernigraniline base (PB)** which is completely oxidized with a blue or violet color, the chemical formula is $(C_6H_4N)_n$. PANI of the three states are not electrical conductive. The conducting state of PANI is called **emeraldine salt (ES)** which is a protonated form of EB after doping, and has a green color. The backbone structure of ES contains "polysemiquinone radical cation stabilized by corresponding 'dopant' counter ions". The doping of PANI can be achieved by two approaches. First, through redox reactions, ES can be formed via oxidation of LE; second, through the non-redox protonation reactions, ES can be achieved via protonation of imine nitrogen atoms of EB. It has to be mentioned that the doping is reversible.

Due to the good conductivity of PANI in ES state, and the easy and cheap synthesis method, PANI has drawn much attention in the application of lithium ion batteries and supercapacitors. It is possible to make various nanostructures for particular applications.

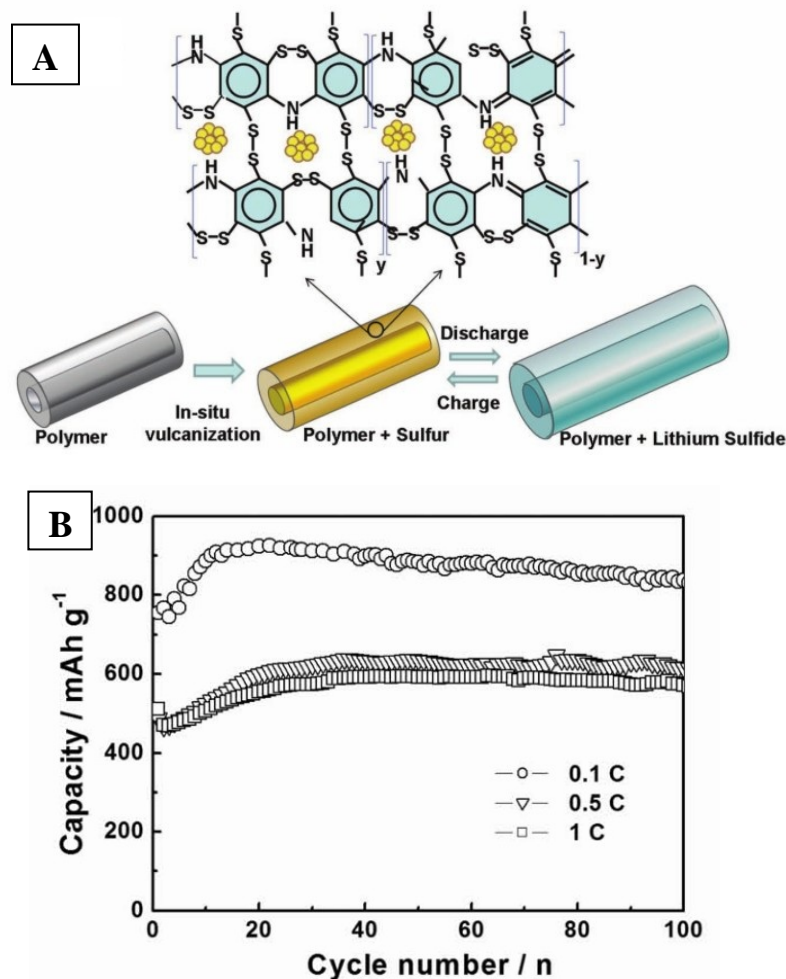


Fig. 2.12 (A) Schematic illustration of the structure and discharge/charge process of the PANI/Sulfur composite. (B) Cycling performance. Reprinted from [92]. Copyright 2012, with permission from WILEY-VCH Verlag GmbH & Co. KGaA, Weinheim.

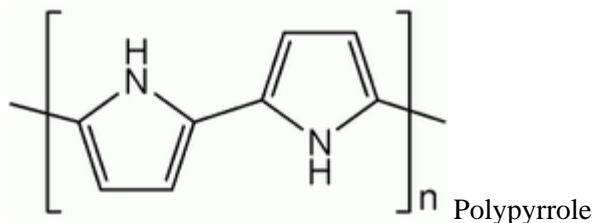
[92] Liu and his group report a Polyaniline nanotube/sulfur composite, where sulfur is encapsulated into the PANI nanotube. The process is carried out by an in situ vulcanization of PANI nanotube when the PANI and sulfur mixture is heated at 280 °C. Sulfur, at molecular level, is considered to be both chemically and physically constrained within the PANI nanotubes as shown in Fig. 2.12A. Most of the sublimed sulfur is encapsulated into the hollow voids and polymer networks of PANI nanotube, while a small portion of sulfur is reacted with polyaniline producing a “cross-

linked stereo SPANI network” with disulfide bond. After 100 cycles, the cell can maintain a discharge capacity of $837 \text{ mAhg}_{\text{sulfur}}^{-1}$ at a 0.1 C rate, Fig. 20B. It presents a cycle life of up to 500 cycles at 1 C rate. The soft polymer matrix can accommodate the volume change of sulfur compounds during charge and discharge. The cross-linked network of PANI matrix encapsulates sulfur and polysulfides. Moreover, imine and amine groups, which are electropositive, on the PANI chains could adsorb electronegative polysulfides. As a result, the polysulfide shuttle is suppressed; a great cycle life is achieved.

[93] Different from Liu’s work, Gao introduces a PANI coated sulfur-carbon composite with a core/shell structure, where Polyaniline is coated on the exterior surface of the sulfur-carbon composite. The sulfur-carbon composite is by heating the mixture of sulfur and porous carbon black. Polyaniline is coated on the sulfur-carbon composite with a thickness of $\approx 5\text{--}10 \text{ nm}$ via an “in situ chemical oxidative polymerization of the aniline” in the sulfur-carbon composite suspension. The composite presents 60% capacity retention of the highest discharge capacity of $635.5 \text{ mAhg}_{\text{sulfur}}^{-1}$ at 10C rate after 200 cycles. The high electrical conductivity of PANI and conductive carbon black enables the significantly improved rate performance of the composite. The synergistic effect of porous carbon and the coated PANI efficiently suppress the polysulfides shuttle. The unique core-shell structure is instrumental for the improvement of overall electrochemical performance. But the utilization of sulfur is not very high.

This work provides a great approach to overcome the problems in lithium-sulfur batteries by taking synergistic advantage of porous carbon and conductive polymers.

2.5.3 Polypyrrole



Polypyrrole (PPy) is a member of the conductive polymer family, which is consisted of a number of joined pyrrole ring structures. PPy can be synthesized through radical polymerization from the oxidation of pyrrole monomer. The undoped PPy is electrically insulating. However, oxidized derivatives of PPy show good electrical conductivity from 2 to 100 S/cm, which relies on the oxidation conditions. As a result, they are applied for chemical sensors, drug delivery and electronic devices. Similar to polyaniline, Polypyrrole also attract the attention of researchers for the application in lithium-sulfur batteries.

[94] Wang et al. report a polypyrrole coated sulfur composite for lithium sulfur batteries, which is synthesized through in-situ polymerization of pyrrole monomer in sulfur aqueous suspension. PPy was doped by sodium *p*-toluenesulphonate and oxidized by FeCl₃. Polypyrrole particles with size ranging from 200 nm to 500 nm are coated onto micrometer sized sulfur powder surface. The composite presents an initial discharge capacity of 1280 mAhg_{sulfur}⁻¹, but after 20 cycles, the capacity decreases to about 600 mAhg_{sulfur}⁻¹. Even though, the composite shows improved electrical performance both on the capacity and durability comparing with the bare sulfur powder, but it still needs further improvement. PPy in the composite provides good conductivity of the electrode and also help adsorb the polysulfides.

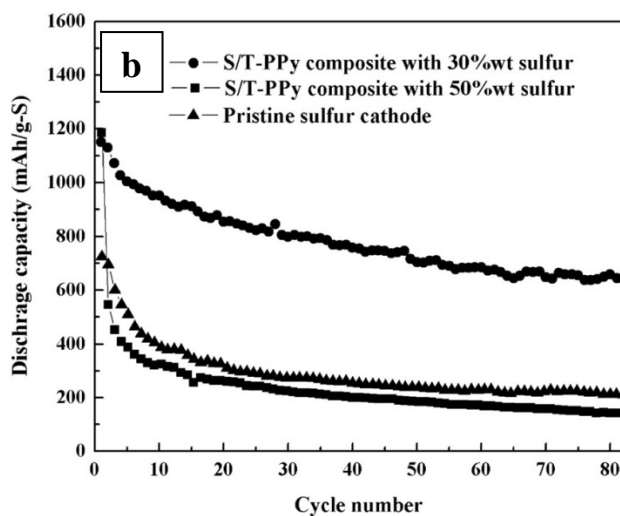
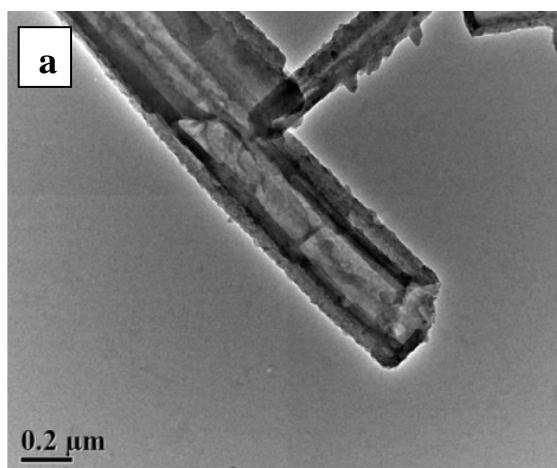


Fig. 2.13 (a) TEM image of the S/T-PPy composite with 50wt. % sulfur, (b) Cycling performance. Reprinted from [95]. Copyright 2011, with permission from Elsevier.

In order to further improve the cyclability of the PPy-sulfur composite cathode, [95] Wen *et al.* prepared a polypyrrole nanotube as a conductive matrix for sulfur, as shown in Fig. 2.13a. The Polypyrrole nanotube is achieved through a self-degraded template method. Sulfur is embedded into the PPy tube after the heat treatment of the mixture of PPy tube and sulfur. The composite shows an initial capacity of $1151.7 \text{ mAh}_{\text{sulfur}}^{-1}$, and after 80 cycles, it can be maintained at about $650 \text{ mAh}_{\text{sulfur}}^{-1}$. But the sulfur content in the composite is around 30 wt.%, Fig. 2.13b. PPy in the

composite provides good conductivity of the electrode, favors the fine distribution of sulfur, and also helps adsorb the polysulfides. Comparing with the simple coating method, the PPy tube shows significant improvement of the overall electrochemical performance of the cells.

[96] Wen *et al.* introduce MWCNTs into the PPy-sulfur system. They prepare a core/shell structure of polypyrrole (PPy) and (MWCNT) for lithium sulfur batteries. PPy is coated on the surface of MWCNTs via the in situ polymerization of pyrrole monomer in the MWCNTs dispersion. Sulfur is introduced to the PPy/MWCNTs composite by heat treatment of their mixture at 155 °C for 4 h. The composite with 25 wt.% PPy and 70 wt.% sulfur presents an initial discharge capacity of 1309 mAh_{g_{sulfur}}⁻¹, which can be maintained at about 725.8 mAh_{g_{sulfur}}⁻¹ after 100 cycles with a current density of 0.1 mAcm⁻². The MWCNTs in the composite form an electrically conductive network. PPy favors the uniform dispersion of the sulfur. Moreover, the unique core/shell structure benefits the adsorption of polysulfides.

PPy is also a good approach for achieving high performance lithium sulfur batteries. But compared with PAN, it has no chemical bond to sulfur. As a result, it will more rely on the unique nano structure for further improvements.

2.6 Metal oxide additives as adsorption catalyst

[97] Zhang *et al.* found out that nanosized Mg_{0.8}Cu_{0.2}O powders as additive of the cathode electrode for lithium sulfur batteries can significantly improve the overall electrochemical performance of the cells. The nanosized Mg_{0.8}Cu_{0.2}O powder is synthesized via the sol-gel method. Nanosized Mg_{0.8}Cu_{0.2}O powders add to the crystalline vanadium pentoxide /S composite cathode. The composite presents significantly improved capacity, rate performance and cycle life after the addition of Mg_{0.8}Cu_{0.2}O powders. It presents capacity retention of 77.5% after 30 cycles. Conversely, the cathode without Mg_{0.8}Cu_{0.2}O powders demonstrates only 56.7% retention. The Mg_{0.8}Cu_{0.2}O powder in the composite provides adsorption to the polysulfides, and also shows “catalytic effect on promoting redox reaction”.

The metal oxide additives shows significant positive effect on the overall performance of lithium sulfur cathode, but it is still not very clear about the working mechanism of this type of materials.

2.7 Project objective

The rechargeable lithium-sulfur battery with its high capacity, low cost and environment friendliness has drawn much attention in recent years. However, sulfur and sulfur-containing organic compounds are electrically and ionically insulating, leading to a low sulfur utilization. Furthermore, the insoluble Li_2S accumulated on the surface of cathode becomes electrochemically irreversible during cycling. Additionally, the 'shuttle effect' leads to the decrease of cathode active material resulting in extensive capacity degradation during cycling process, in which soluble polysulfides formed in the cathode side diffuse to the anode and then diffuse back to the cathode by a series of reactions. These detrimental factors severely restrict the sulfur cathode to achieve high power density and good cycling stability.

To overcome the aforementioned problems, different approaches have been employed, such as combining sulfur with conductive polymers, encapsulating or coating elemental sulfur in different nanostructured carbonaceous materials, modify the electrolyte such as LiNO_3 additives and gel electrolyte. There are also other methods like surface modification to passivate the lithium metal anode, and replace the elemental sulfur cathode with lithiated sulfur cathode as well as replace the lithium metal anode.

The project consists of the development and characterization of nanostructured electrode materials for lithium sulfur batteries. This work will focus on the development of Sulfur-Polyacrylonitrile based cathode materials. The objective is to improve the capacity, durability as well as the high rate performance of the cells.

Chapter 3

Techniques for Physical and Electrochemical Characterization

In order to better understand and analyze the material and its electrochemical performance, it is necessary to use proper characterization in structural, specific compositional and electrochemical aspects. Several techniques were applied for both physical and electrochemical characterization of the material. From the electrochemical characterization, the capacity, durability, resistances, energy and power density of the cells as well as the electrochemistry behind them can be determined. Based on the physical characterization, the chemical, structural properties of the materials for lithium sulfur batteries are evaluated. As a result, the physical properties of the electrode and its electrochemical performance can be integrated and analyzed. In this section, several characterization techniques as well as their respective principles are introduced. [98]

3.1 Scanning electron microscopy

Scanning electron microscopy (SEM) is a common and efficacious technique for the estimation of the morphology, atomic composition of various materials. This analytical technique is permitted through the scanning of samples in a raster scan pattern with focused electron beams. The surface topography and composition information of the samples can be detected through combination of the beam's position and signals which are produced by the interaction of focused electron beams and the atoms near the surface of the sample. Signals generated from the interaction contain transmitted electrons, secondary electrons, backscattered electrons, X-rays and more. From the secondary electron signals, high-resolution (less than 1 nm in size) morphology and topography of the sample surface can be detected. The magnifications of the images can be controlled from about 10 times to more than 500,000 times. Backscattered electrons which come from the reflection of elastic scattering can provide valuable information for demonstrating contrasts in multiphase specimens. X-rays are released from the fill of inner shells by a higher-energy electron in the specimen atoms when electron beams interact with the sample atoms (inelastic collision). The X-rays can offer composition

and elements information in the sample. Due to the strong correlation between the intensity of the backscattered electron signals with the atomic number of the sample, the backscattered electron signals and X-rays spectra are often combined for analytical SEM. [99, 100]

3.2 Energy-dispersive X-ray spectroscopy

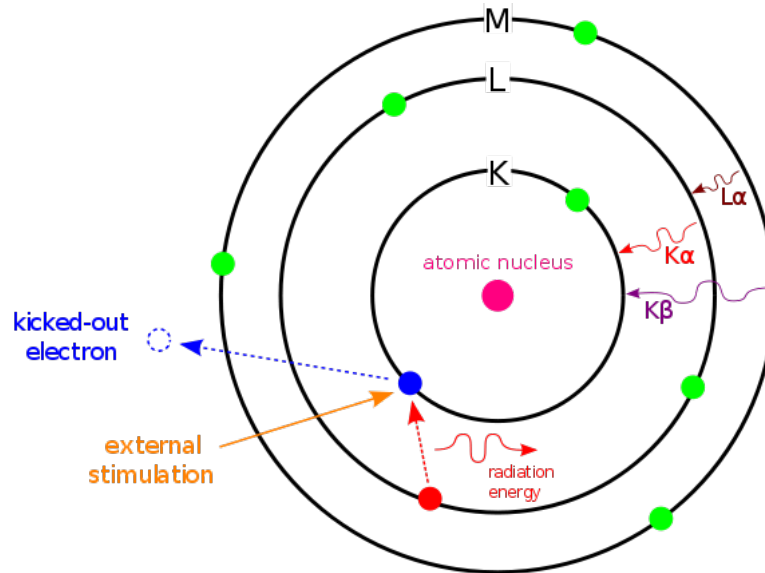


Fig. 3.1 Principle of EDX. Reprinted from [101] Copyright 2007, with permission from Wikipedia.

Energy-dispersive X-ray spectroscopy (EDX) is a useful technique for analysis of the elemental composition of a specimen. The fundamental principle of EDX relies on the correlation between the atomic structures of each element with its unique X-ray spectrum peaks. As shown in Fig. 3.1, when an incident focused electrons or X-rays beam interacts with the specimen, discrete electrons in the ground state or inner shell of atoms in the specimen may be excited and ejected from the inner shell, and thus leave an electron void in the inner shell of the specimen atoms. The electron void may be filled by the electron from an outer shell which is in a higher energy level, while X-rays may be emitted due to the energy difference between the two shells. These X-rays released from the sample

which are extremely related to the atomic structure of elements within the sample can be detected as the original signals for an energy-dispersive spectrometer. As a result, the elemental composition of the sample can be analyzed.[101]

3.3 Transmission electron microscopy

Transmission electron microscopy (TEM) is a major analysis technique in physical, chemical and biological fields for material science, as well as in nanotechnology, cancer research, pollution, semiconductor and virology research. Unlike SEM based on detecting secondary or backscatter electrons, transmission electron microscopy (TEM) is a microscopy technique permitted upon the interaction of incident electrons with the specimen when the incident electrons beam transmits through the sample. The signals can be collected and processed to produce an image of structure of the thin materials. The magnified image can be detected by a CCD camera or displayed on a fluorescent screen. TEM was first commercialized in 1939, while it was invented by Max Knoll and Ernst Ruska in 1931. As a result of the small de Broglie wavelength of electrons, TEMs can provide extremely high resolution of images which enables researchers to even look at a single column of atoms. At lower magnifications, the contrast of TEM image contrast depends on the composition and thickness of the specimen as well as its absorption of electrons. At larger magnifications, it is influenced by complex wave interactions. [102]

High-resolution transmission electron microscopy (HRTEM) is a high resolution mode of TEM which enables researchers to examine the crystal structure of materials at an atomic scale. Crystalline defects and even single atoms can be imaged within HRTEM. The highest resolution as reported is 0.047 nm. However, HRTEM images are based on phase contrast, which is significantly influenced by focus and astigmatism due to the aberration of microscope lens. [103]

3.4 Atomic force microscopy

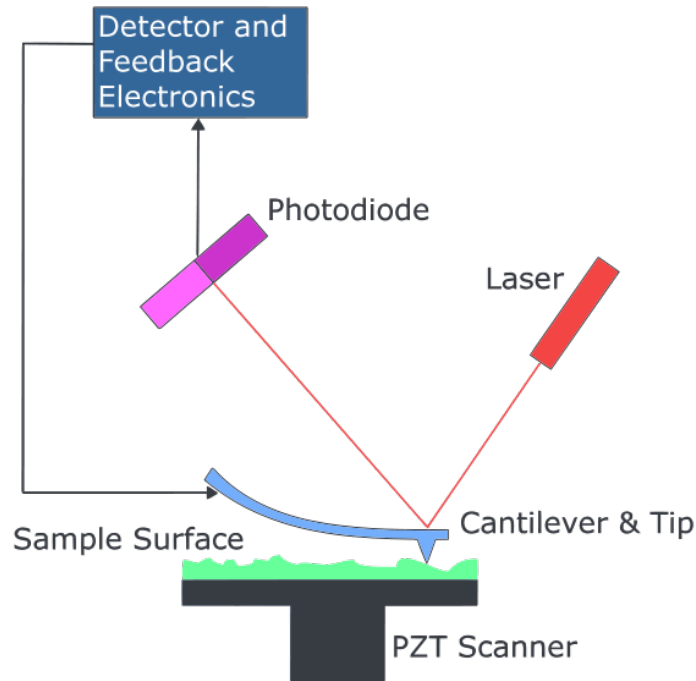


Fig. 3.2 Block diagram of AFM. Reprinted from [104] Copyright 2009, with permission from Wikipedia.

The AFM is a scanning probe microscope for imaging, examining material at nanoscale with high-resolution, which is implemented by feeling surface of the specimen with a mechanical probe. As shown in Fig. 3.2, AFM is generally consisted of a piezoelectric scanner, cantilever and tip, feedback electronics, laser and photodiode detector. The AFM scanner is used to mount and move the specimen under precise control, it is made from piezoelectric material. Piezoelectric material is a type of material that will proportionally expand when an applied voltage is loaded. This special character enables accurate control of tiny movements of the specimen during scanning. The cantilever is usually made from silicon nitride or silicon. There is a sharp tip with nanometer sized radius of curvature at the end of the cantilever which is designed as a probe to scan surface of the sample. The tip will be brought approximately into surface of the specimen, at the meantime, forces between the specimen and the tip, including van der Waals forces, electrostatic forces, mechanical

contact force, capillary forces, chemical bonding and etc, will lead to a cantilever deflection, which is describe by Hooke's law. The specimen will be adjusted in the z direction for keeping a constant force and scanned in the x and y directions. The deflection can be measured by the photodiodes which can gather the reflected laser light from the cantilever and generate an output which is proportional to the deflection of the cantilever. The output signals are used to estimate the height or z information of the specimen at according x and y, as well for the feedback electronics to keep a constant force between the specimen and tip by adjusting their distance. The topography of the specimen can be achieved from $z = f(x,y)$. [104]

3.5 Thermogravimetric analysis/Differential thermal analysis

Thermogravimetric analysis (TGA) is a thermal analysis technique which measures the chemical properties like dehydration, solid-gas reactions, decomposition, and physical properties such as sublimation, vaporization, absorption and desorption of a specimen with increasing temperature. The TGA instrument continuously measures the weight of the specimen while it is heated (up to 2000°C). During this process, the mass change caused by the decomposition of components in the specimen can be detected. The mass percentage is usually plot with temperature as shown in Fig.4 . The first derivatives of weight percentage to temperature can be used to estimate points of inflection for more profound understanding. [105]

Differential thermal analysis (DTA) is a thermo-analytic technique for studying transformations including melting, glass transitions, sublimation, and crystallization of the specimen. Temperature difference between specimen and inert reference are recorded against temperature. From the DTA thermo-gram, either endothermic or exothermic process can be identified. DTA is normally incorporated into TGA instrument in today's technique. As a result, both heat flow and mass loss of the sample can be simultaneously studied. [106]

3.6 Fourier transform infrared spectroscopy

Fourier transform infrared spectroscopy (FTIR) is a method which simultaneously detects a wide range of spectral data and provides infrared spectrum information of Raman scattering, emission, absorption of a specimen. The actual spectrum of FTIR is converted from the raw data via a Fourier transform, that's where the term of "Fourier transform" in FTIR comes from. The technique of FTIR is implemented through irradiation scanning of a sample with a light beam which comprises various frequencies. As a result, the adsorption of the light beam by the specimen can be measured. This process is repeated by changing the frequencies combination of the light beam. The raw data points is collected, and then processed by computer through the Fourier transform algorithm to conclude the absorption by the specimen at corresponding wavelength. The light beam aforementioned is produced by shining a light source which comprises a full spectrum of frequencies into a Michelson interferometer. Through manipulating the Michelson interferometer, each frequency of light in the source can be periodically transmitted and blocked owing to the interference of wave. Hence, light spectrum of the source can be modulated at each measure. [107]

3.7 X-ray Diffraction analysis

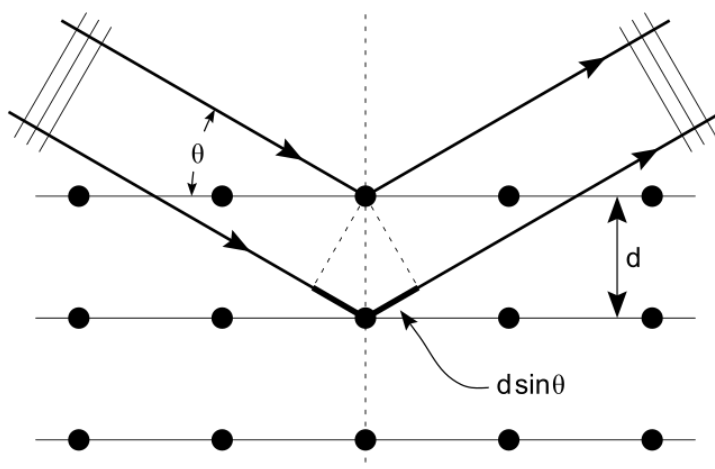


Fig. 3.3 Bragg diffraction from a cubic crystal lattice. Reprinted from [108] Copyright, with permission from Wikipedia.

[108] X-ray diffractometry (XRD) is implemented by using a monochromatic X-ray beam to hit the specimen. As a result, the X-rays will be scattered in various angles. Based on Bragg's law, as shown in Fig. 3.3, the incoming beam will lead the scatters to generate a regular array of spherical waves. If the beam wavelength is λ , and the distance of the plane distance of the scatters is d . Due to the destructive interference, these waves will cancel out each other in some angles. However, they will constructively add each other in the other specific angles. These directions can be determined by Bragg's law:

$$2d \sin \theta = n\lambda$$

θ is the incident angle and n is an integer.

Hence, the wave length of the beam is of the same order of magnitude as the space of the diffraction planes of the specimen. A typical and unique diffraction patterns for each specific material can be produced. The atomic and molecular structure of a crystal can be determined by analyzing the diffraction data in the XRD patterns. [109]

3.8 Elemental analysis

Elemental analysis is a technique that can examine the elemental composition both quantitatively and qualitatively in a specimen. Elemental analysis generally denotes CHNX analysis in organic analysis, which determines the weight percentage of X (sulfur or halogens), nitrogen, hydrogen, and carbon of a specimen. This technique is essential to determine the structure and composition of an unknown or synthesized composite. Generally, CHN analysis is implemented by burning a specimen in an extra oxygen environment. The combustion products including nitric oxide, water, and carbon dioxide are collected for calculation of the elemental composition in the specimen. [110]

In this work, sulfur content in the synthesized sample was all detected by a CHNS elemental analyzer.

3.9 Z-potential

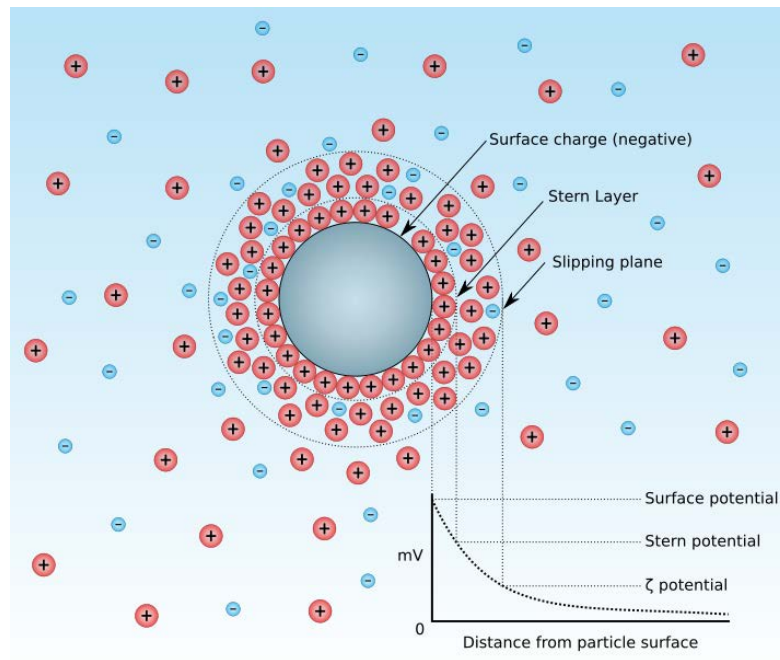


Fig.28 Diagram showing the ionic concentration and potential difference as a function of distance from the charged surface of a particle suspended in a dispersion medium. Reprinted from [111]. Copyright, with permission from Wikipedia.

An electrical double layer (DL) denotes two parallel layers of charge formed around the particles in liquid. As shown in Fig. 28, ions which are adsorbed onto the particles surface formed the internal stern layer. Owing to the thermal motion ions and Coulomb force, ions which are attracted to the external surface formed the second layer. Zeta potential is defined as the electric potential at outer surface-the slipping plane of the DL, which represents the potential difference between the stationary layer of ions surrounding the particle and the liquid. Zeta potential shows the degree of repulsion between dispersed particle neighbors with similar charge. When the value of zeta potential is high, repulsion surpasses attraction and the particles will trend to be dispersed rather than to aggregate if the particles are small enough. As a result, stability of colloidal dispersions can be implied from the value of Zeta potential, as shown in Table 3.1. [111, 112]

Zeta potential [mV]	Stability behavior of the colloid
from 0 to ± 5 ,	Rapid coagulation or flocculation
from ± 10 to ± 30	Incipient instability
from ± 30 to ± 40	Moderate stability
from ± 40 to ± 60	Good stability
more than ± 61	Excellent stability

Table 3.1 Colloidal Stability with the value of Zeta potential. Reprinted from [111] Copyright 2007, with permission from Wikipedia.

3.10 Half-cell electrochemical testing

The electrochemical performance of the composite was evaluated using lithium metal as counter and pseudo-reference electrode. The cathode was prepared by mixing active material, Katjen Black 600, and polyvinylidene fluoride (PVDF) with a weight ratio of 8:1:1 using N-methylpyrrolidone (NMP) as solvent. The resulting slurry was painted onto nickel foam current collector ($\Phi 12$ mm) and dried at 60 °C for 12 h. The final electrode loading density was around 6~8 mg/cm² (total cathode material). CR2025 coin cells were assembled in an argon-filled glove box (Mbraun) using 1.0 M LiPF₆ in 1:1:1 v/v EC/DC/DMC as electrolyte and Celgard 2250 as separator. The cells were galvanostatically charge-discharged between 1 V and 3 V (vs Li/Li⁺) using a battery tester (Neware Shenzhen, China). Cyclic voltammetry measurements were carried out on a Biologic VMP3 electrochemistry workstation.

3.10.1 Galvanostatic Charge/Discharge

Galvanostatic Charge/Discharge technique is a common procedure applied in electrochemistry test of electrode materials in batteries. It is implemented by charging the cell at constant current (I) and subsequently discharging at constant current. [98]

The potential difference across the cell will change with time t . The capacity or quantity of electricity Q can be described as below:

$$Q=I*t$$

During the discharge process, the electrochemical active materials at the anode are oxidized while releasing electrons. Simultaneously the electrochemical active materials at the cathode receive electrons and are reduced at the same time. The electrons transport through the external circuit. The relationship between the mass of active material (m) at the anode and the constant current I can be described by Faraday's first law:

$$m = \frac{M}{zF} \cdot It$$

Where the molar mass of active material is M , number of electrons transported is z , and Faraday constant is F (26.8 Ah mol^{-1}).

The charging process only existed in secondary cells. It requires a charge voltage source to be applied on the cell, which is higher than the equilibrium potentials difference of the two half-cells. During the charge process, the electrochemical active materials at the positive electrode are oxidized; meanwhile a reduction process occurs at the negative electrode. [113]

3.10.2 Cyclic Voltammetry

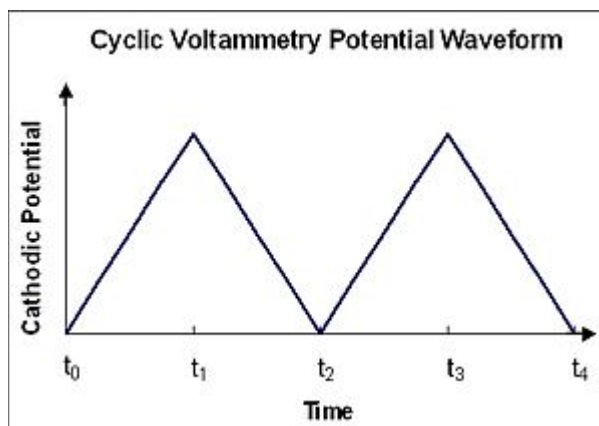


Fig. 3.5 cyclic voltammetry waveform. Reprinted from [114] Copyright, with permission from Wikipedia.

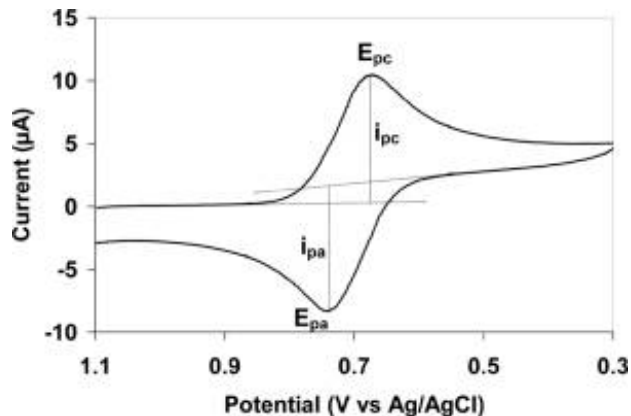


Fig. 3.6 typical cyclic voltammogram where i_{pc} and i_{pa} show the peak cathodic and anodic current respectively for a reversible reaction. Reprinted from [114] Copyright 2007, with permission from Wikipedia.

Cyclic voltammetry (CV) is a type of potentiodynamic electrochemical measurement which is implemented by linearly ramp the potential (E) between the working electrode and the reference electrode with time in a scan rate (V/s) as shown in Fig.3.5. Meanwhile, the current (I) between the counter electrode and the working electrode is recorded. The potential ramp of working electrode will be inverted when the potential reaches a set value. The cyclic voltammogram trace is achieved by plot potential (E) versus current (I). If any analytes can be oxidized (or reduced) in the range of the scanned potential window during the forward scan, a current peak for the corresponding analyte can be produced. The current will rise while the potential gets to the analyte reduction potential and then drop down due to the decrease of the analyte concentration to be close to the electrode surface. If the redox couple is reversible, the analyte which is reduced in the forward scan will be reoxidized in the reverse scan, and an oxidation current peak of reverse polarity with similar shape to the reduction peak will be generated. Fig. 3.6 shows a typical CV diagram. The redox potential and the electrochemical reaction rates of the materials can be estimated from CV diagram. Due to the polarization overpotential of the reversible couples which caused by the limitation of the diffusion

rates of analyte and electronic transfer speed at the surface, there will be a potential difference between the absolute potential of the oxidation peak and the reduction peak. [114]

3.10.3 Impedance Spectroscopy

The electrochemical impedance spectroscopy (EIS) is a measurement of impedance as a function of the frequency (ω) of the alternating current (AC) source. Generally, the impedance of a cell can be described as below: [115]

$$\mathbf{Z}(\omega) = Z_{\text{Re}} - jZ_{\text{Im}}$$

where Z_{Im} and Z_{Re} are the imaginary and real parts of the impedance.

A typical *Nyquist plot* plots Z_{Im} against Z_{Re} for different values of ω . From the EIS, the phase relation between Z_{Im} and Z_{Re} can be examined, and the circuit elements of the electrode structure including potential-dependent Faradaic resistances and the equivalent series resistance (ESR) can be estimated. The EIS can be performed over a wide range of frequencies (10 mHz ~ 10 KHz). A typical Nyquist impedance plot of a cell may contain semicircles at high frequencies region; a Warburg region at moderate frequencies related to the resistance of ion diffusion and a non-vertical slope region at low frequencies. [98]

Chapter 4

Fundamental Study of SPAN Composite Cathode for Li-S batteries

4.1 Introduction

Rechargeable lithium sulfur (Li-S) batteries are safe, environmentally friendly and economical alternative energy storage systems that can potentially be combined with renewable sources including wind solar and wave energy. Sulfur has a high theoretical specific capacity of ~1680 mAh/g, attainable through the reversible redox reaction denoted as $S_8 + 16Li \leftrightarrow 8Li_2S$, which yields an average cell voltage of ~2.2 V. However, two detrimental factors prevent the achievement of the full potential of the Li-S batteries. First, the poor electrical/ionic conductivity of elemental sulfur and Li_2S severely hampers the utilization of active material for obtaining full capacity of the electrode. [116] Second, dissolution of intermediate long-chain polysulfides (LiS_n , $2 < n < 7$) into the electrolyte and their shuttle between cathode and anode leads to fast capacity degradation and low Coulombic efficiency.[117] As a result of this shuttle process, insoluble and insulating Li_2S/Li_2S_2 precipitates on the surface of electrodes causing loss of active material and rendering the electrodes surface electrochemically inactive.[118]

Extensive research efforts have been devoted to overcome the aforementioned problems, such as combination of sulfur with conductive polymers,[119-123] and encapsulation or coating of elemental sulfur in different nanostructured carbonaceous materials.[124-135] Noteworthy, sulfur-polyacrylonitrile (SPAN) composites, wherein sulfur is chemically bond to the polymer backbone and PAN acts as a conducting matrix, have shown some success in suppressing the shuttle effect.[136,137] However, due to the limited electrical conductivity of polyacrylonitrile, the capacity retention and rate performance of the SPAN systems are still very modest.

My project has been focused on the development and characterization of cathode materials based on the Sulfur-PAN system for lithium sulfur batteries. In this chapter, the fundamentals of SPAN Composite will be discussed.

4.2 Preparation of SPAN Composite



Fig. 4.1 Preparation procedure of SPAN composite

The SPAN composite or SPAN/CNT are prepared by mixing 8.57g Sulfur, 1.43g PAN and with or without 0.5g MWCNT, respectively, by ball milling for 3 hours at 400 rpm. Then the composite was heated at 320 °C for several hours. After heated for about 7 hours, the sulfur content for the achieved SPAN/CNT composite is ~70 wt. % detected from elemental analyzer.

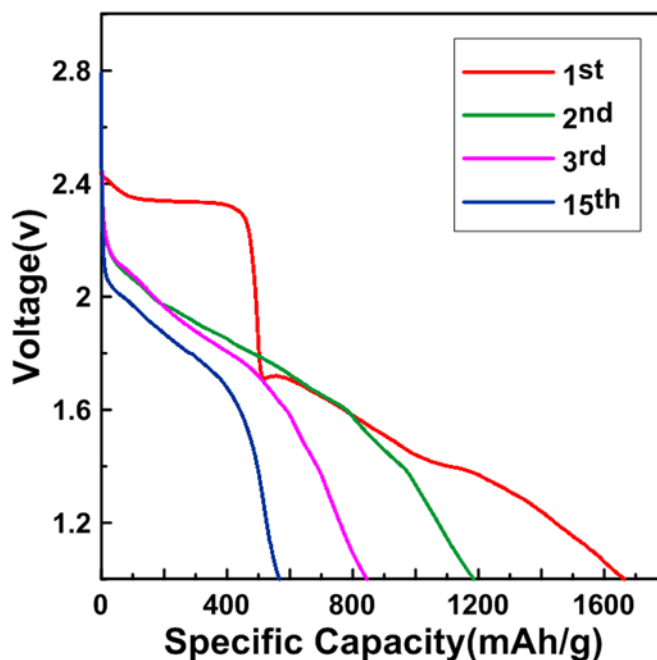


Fig. 4.2 Charge/discharge profile for the SPAN/CNT composite with 70 wt. %

The charge/discharge results are shown in Fig. 4.2. It can be seen that there is a long plateau at 2.4 V in the first discharge, indicating the existence of excess amount of un-reacted sulfur which is not bound with the PAN backbone. The capacity of the composite also decreases rapidly.

Hence, the heat treatment method for preparing the SPAN composite was systematically studied. The key point of the idea is that first make sure complete reaction between PAN and Sulfur, second, remove the excess amount of un-reacted sulfur.

Batch No.	Weight of Reagent (g)	Time(h)	Sulfur Content(%)
1a	10.5	3	70.2
1b	2	+2	43.3
1c	1	+2	42.1
2a	10.5	5	69.6
2b	2	+2	42.8
3a	10.5	7	69.1
3b	2	+2	42.3

Table 4.1 Table for studying the heat treatment method, “a” refers to 1st step of the heat treatment, “b” refers to 2nd step of the heat treatment of the material from the 1st step, “c” refers the 3rd heat treatment of the material achieved from the 2nd step.

As shown in Table 4.1, 10.5 g of the raw material after heated for 3 h, sulfur content achieved is about 70 wt. % (1a). In step 1b, 2 g of the material obtained from the 1a step were heated for 2 more hours, the sulfur content decreased to about 43 wt. %. In step 1c, 1 g of the materials achieved from the 1b step were heated for 2 more hours, the sulfur content did not change much, indicating the sulfur content is almost stable after the second heat treatment and the un-reacted sulfur should be removed.

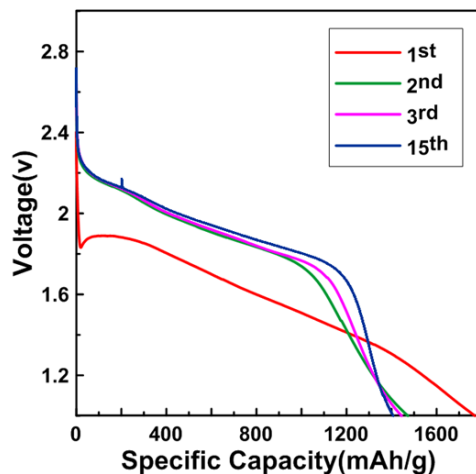


Fig. 4.3 Charge/discharge profile for the SPAN/CNT composite with 42 wt. %.

The charge and discharge results (Fig. 4.3) of the composite which is after the second step heat treatment with about 43 wt.% sulfur content shows that the long plateau at 2.4 v in the first discharge disappeared, and the capacity are very stable, confirms the removal of un-reacted sulfur. The two-step heat treatment is very efficient to prepare the SPAN composite.

4.3 Effect of Sulfur content to Battery Performance

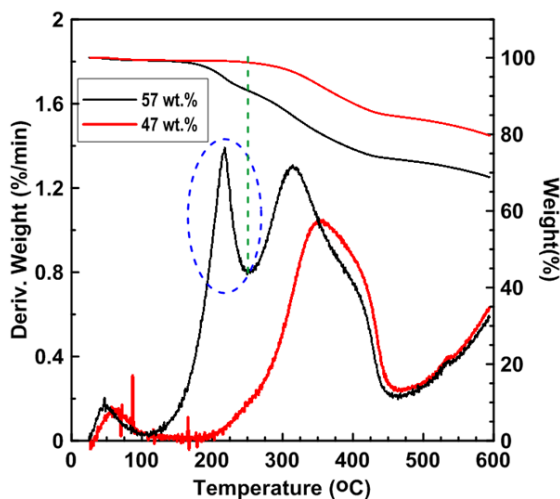


Fig. 4.4 TGA results of SPAN samples carried out under N_2 from room temperature to 600 °C

For the SPAN composite, the effect of different sulfur content to the battery performance was studied. As shown in Fig. 4.4, there is an onset of mass loss of the composite with 57 wt. % sulfur content at 220 °C, which is due to the evaporation of elementary sulfur which is not bound with the PAN backbone. The second onset of mass loss at around 350 °C is due to the decomposition of the sulfur from the bond with PAN.

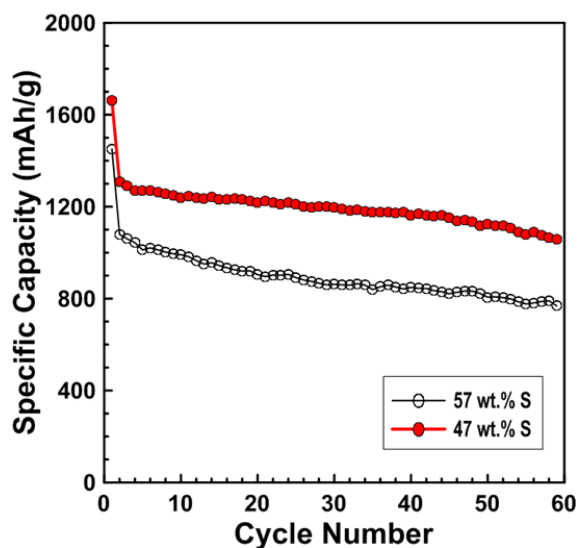


Fig. 4.5 Cycling performance of the SPAN composites with different sulfur content.

As shown in Fig. 4.5, the SPAN composite with 57 wt. % sulfur content has much lower capacity comparing the SPAN composite with 47 wt. % sulfur. The existence of un-reacted sulfur renders the electrode lower electrical conductivity and more effect from the shuttle of polysulfides.

4.4 Effect of Conductor to Battery Performance

	BET surface area	Pore Size	Pore Volume
Acetylene Black (AB)	90 m ² /g	35-45 nm	220-330 ml/100g
Ketjenblack. EC-600JD (KB)	1400 m ² /g	2-10 nm	480-510 ml/100g

Table 4.2 porosity of two types of carbon

The cathode electrode are composed of 80 wt.% Composite, 10 wt.% Conductor and 10 wt.% PVDF (Polyvinylidifluoride) as binder. In order to study if a carbon conductor with high porosity could help to absorb the dissolved polysulfides and thus enhance the capacity retention of the cells, two type of carbon conductors are studied as shown in Table 4.2.

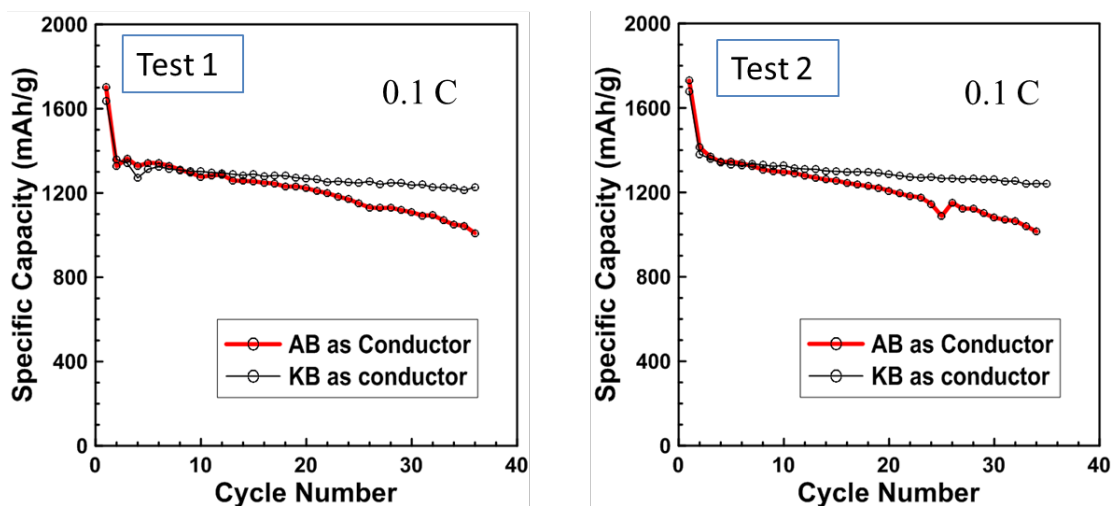


Fig. 4.6 Cycling performance of the SPAN composite with KB and AB as conductor.

KB has a higher surface area, larger pore volume and smaller pore size comparing with AB. The cycling tests (Fig. 4.6) show that the cells with KB as conductor have about 92 % capacity retention after 35 cycles; conversely, the cells with AB black have about 75 % capacity retention. It indicates that KB with more porous structure could help absorb the dissolved polysulfides within the electrode, and thus the shuttle of polysulfide is suppressed.

4.5 Effect of Load of Active Materials to Battery Performance

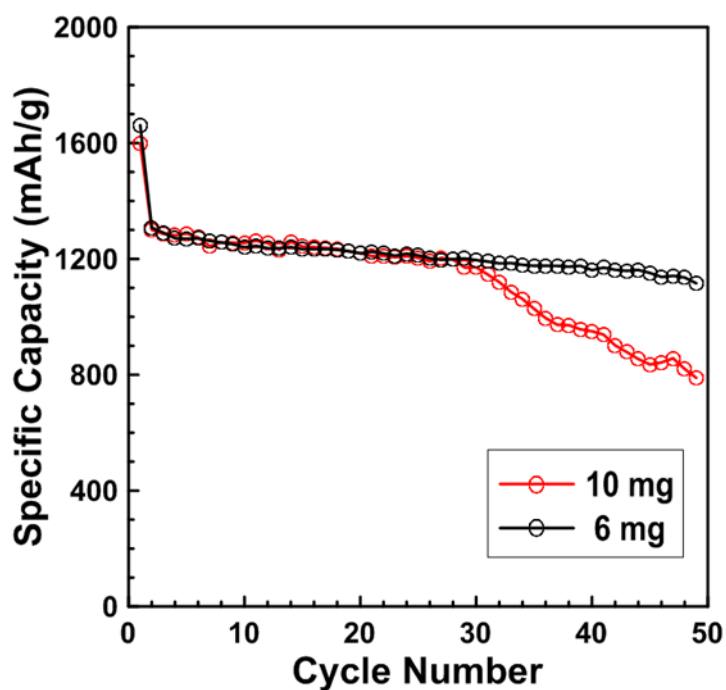


Fig. 4.7 cycling performance of cells with different load of active materials

When preparing the electrode, the amount of load of active materials can be controlled. In Fig. 4.7, it shows the cycling performance of cells with different load of active materials. The capacity of the cells with 10 mg of load rapidly decrease after about 30 cycles; conversely, the capacity of the

cells with 6 mg of load are still very stable after 30 cycles. It indicates that the increase of load of active material could negatively influence the capacity durability of the cells.

4.6 Effect of CNT as additives to Battery Performance

Carbon nanotube has extraordinary electronic conductivity, it could be used to increase the conductivity of the electrode, and hence, enhance the capacity of the electrode.

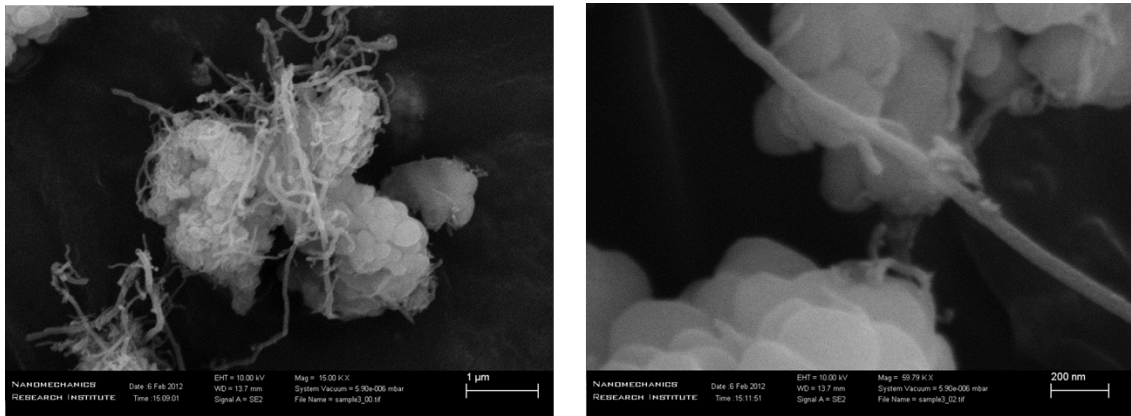


Fig. 4.8 SEM images of SPAN composite with CNT as additives (43 wt.% Sulfur and 10 wt.% CNT)

Fig. 4.8 shows the SEM image of SPAN/CNT composite, it can be seen that CNT can form bridges between the SAPN particles. CNT could form a good conductive network within the electrode.

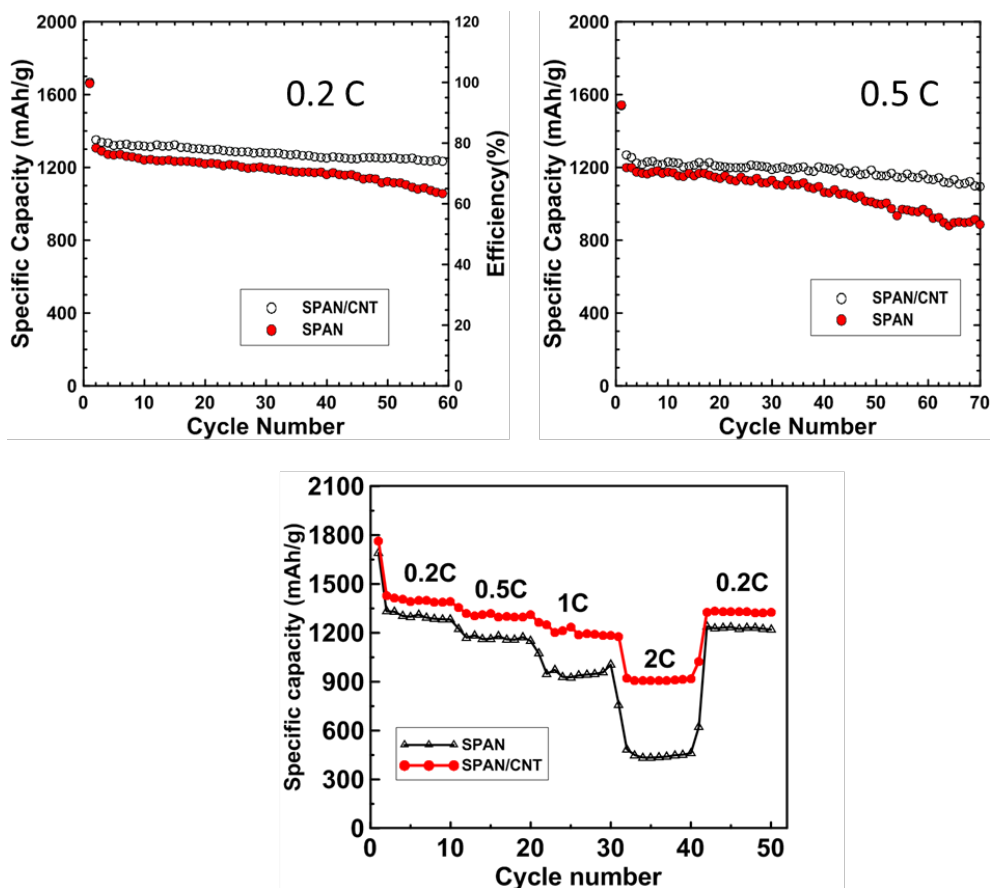


Fig. 4.9 Rate performance of the SPAN/CNT and SPAN composite.

The Rate performance of the SPAN/CNT composites is shown in Fig. 4.9. It can be seen that the capacity at lower C-rates has not much difference between the two composite, however, at higher C-rates like 1 C and 2 C, the SPAN/CNT composite has much higher capacity. CNT could form a highly conductive network, and thus enhance the electronic conductivity of the electrode. As a result, the rate performance of the cells is improved.

4.7 Summary

Fundamentals of SPAN composite as cathode has been studied, including the heat treatment method, effect of sulfur content, conductor, loading amount of active materials, and CNT as additive. This study gives guidance to the further development of the SPAN based cathode material.

Chapter 5

A sulfur-polyacrylonitrile/graphene composite cathode for lithium batteries with excellent cyclability

5.1 Outline of the work

A sulfur-polyacrylonitrile/reduced graphene oxide (SPAN/RGO) composite with unique electrochemical properties was prepared *via* deposition of PAN on the surface of RGO sheets followed by ball milling with sulfur and heat treatment. Infrared spectroscopy and microscopy studies indicate that the composite consists of RGO decorated by SPAN particles of 100 nm average size. The PAN/RGO composite shows good overall electrochemical performance when used in Li/S batteries. It exhibits ~85% retention of the initial reversible capacity of 1467 mAh/g over 100 cycles at a constant current rate of 0.1 C and retains 1100 mAh/g after 200 cycles. In addition, the composite displays excellent coulombic efficiency and rate capability, delivering up to 828 mAh/g reversible capacity at 2 C. The improved performance stems from composition and structure of the composite, wherein RGO renders a robust electron transport framework and PAN acts as sulfur/polysulfide absorber.

5.2 Introduction

Rechargeable lithium sulfur (Li-S) batteries are safe, environmentally friendly and economical alternative energy storage systems that can potentially be combined with renewable sources including wind solar and wave energy. Sulfur has a high theoretical specific capacity of ~1680 mAh/g, attainable through the reversible redox reaction denoted as $S_8 + 16Li \leftrightarrow 8Li_2S$, which yields an average cell voltage of ~2.2 V. However, two detrimental factors prevent the achievement of the full potential of the Li-S batteries. First, the poor electrical/ionic conductivity of elemental sulfur and Li_2S severely hampers the utilization of active material for obtaining full capacity of the electrode. [116] Second, dissolution of intermediate long-chain polysulfides (Li_2S_n , $2 < n < 7$) into the electrolyte and their shuttle between cathode and anode leads to fast capacity degradation and low

Coulombic efficiency.[117] As a result of this shuttle process, insoluble and insulating $\text{Li}_2\text{S}/\text{Li}_2\text{S}_2$ precipitates on the surface of electrodes causing loss of active material and rendering the electrodes surface electrochemically inactive.[118]

Extensive research efforts have been devoted to overcome the aforementioned problems, such as combination of sulfur with conductive polymers,[119-123] and encapsulation or coating of elemental sulfur in different nanostructured carbonaceous materials.[124-135] Noteworthy, sulfur-polyacrylonitrile (SPAN) composites, wherein sulfur is chemically bonded to the polymer backbone and PAN acts as a conducting matrix, have shown some success in suppressing the shuttle effect.[136,137] However, due to the limited electrical conductivity of polyacrylonitrile, the capacity retention and rate performance of the SPAN systems are still very modest.

Recently, graphene has been intensively investigated for enhancing the rate and cycling performance of lithium sulfur batteries. Graphene, which has a two-dimensional, one-atom-thick nanosheet structure offers extraordinary electronic, thermal and mechanical properties. [138-143] Herein, we report on a sulfur-polyacrylonitrile-reduced graphene oxide (SPAN/RGO) composite prepared by a low-cost and environmentally benign solvent exchange approach. The electrochemical performance of the composite as a cathode material for Li/S batteries was also investigated.

5.3 Experimental Section

5.3.1 Materials

Natural graphite (Alfa Aesar), hydrazine (35 wt. % in water), ammonia solution (28 wt. % in water), polyacrylonitrile, sulfur, dimethylformamide, sodium chloride, sulfuric acid (concentrated), sodium nitrate, potassium permanganate, hydrogen peroxide (30 wt. %), hydrochloric acid (37 wt. %) (Sigma-Aldrich) were used without further purification, Katjen Black 600 (AkzoNobel), polyvinylidene fluoride (Sigma-Aldrich), N-methylpyrrolidone (Sigma-Aldrich). Milli-Q grade water was used in all experiments.

5.3.2 Preparation of Reduced Graphene Oxide (RGO) aqueous suspension

Graphite oxide (GO) was prepared through a modified Hummers method.[144] 0.8 g natural graphite was stirred in 23 ml concentrated H₂SO₄ (98%) for 24 hours, and 3 g KMnO₄ were added to the dispersion while the temperature was kept below 20 °C. The mixture was then diluted and heated up to 100 °C for 15 minutes. The reaction was terminated by addition of 10mL H₂O₂ solution (30%) and 140 ml water. The resulting graphite oxide was repeatedly washed with 5% HCl aqueous solution and water. A brown-colored dispersion was achieved. The graphite oxide dispersion was ultrasonicated for 30 minutes using a Hielscher Ultrasonics (UIP 1000hd, 150W, 50% amplitude).

Next, a reduced graphene oxide dispersion was achieved through chemical reduction of GO with the presence of ammonia.[145] The GO dispersion was diluted with water to 0.05 wt%. 100 ml of the homogeneous dispersion was then mixed with 100 ml water, 100 µl hydrazine solution (35 wt. % in water), and 0.7 ml ammonia solution (28 wt. % in water) in a 250 ml round bottom flask. The weight ratio of hydrazine to graphene oxide was 7:10. The flask and its contents were immersed into an oil bath, kept at 95 °C, for 1 hour. The excess hydrazine was thoroughly removed by dialysis against 0.5% ammonia solution.

5.3.3 Polyacrylonitrile/ Reduced Graphene Oxide composite (PAN/RGO)

100 ml of the as prepared RGO dispersion were mixed with 64 ml of a 5.88 g/L PAN/DMF solution. After vigorous stirring for 10 minutes, 600 ml 0.5 wt% ammonia aqueous solution was added to the beaker and stirred for 24 hours. About 0.4 g PAN/RGO sediment was obtained by centrifugation, and repeatedly washing with ethanol and water.

5.3.4 Sulfur-Polyacrylonitrile/partially Reduced Graphene Oxide composite (SPAN/RGO)

The PAN/RGO composite obtained by centrifugation was immediately subject to wet ball milling with 1.6 g sulfur at 500 rpm for 3 hours. The mixture was then dried in a vacuum oven at 60 °C, followed by heat treatment at 320 °C for 5 hours under argon atmosphere.

5.3.5 Characterization

The sulfur content in all the composites was determined with a CHNOS Elemental Analyzer (Vario Micro Cube, Elementar Americas). The morphology of the composites particles was evaluated by scanning electron microscopy (SEM, Leo FESEM). Atomic force microscopy (AFM, Agilent 4500 Series) imaging was detected under tapping mode. Zeta potential of graphene was determined using a laser electrophoresis zeta potential analyser (Zetasizer 3000HSA, Malvern Instruments). Powder X-ray diffraction (XRD, Bruker D8 Discover) analysis was carried out using Cu–K α 1.1446 Å radiation at 40 kV. Fourier transformed infrared spectroscopy (FTIR, Bruker Vertex 70) analysis of KBr pellets were recorded in transmission mode. Thermogravimetric analysis (TGA, TA Instruments SDT Q600) was performed in nitrogen atmosphere at heating rate of 10 °C/min to investigate the thermal stability of the composites.

The electrochemical performance of the composites was evaluated using lithium metal as counter and pseudo-reference electrode. The cathode was prepared by mixing active material, Katjen Black 600, and polyvinylidene difluoride (PVDF) with a weight ratio of 8:1:1 using N-methylpyrrolidone (NMP) as solvent. The resulting slurry was painted onto nickel foam current collector (Φ 12 mm) and dried at 60 °C for 12 h. The final electrode loading density was around 6~8 mg/cm² (total cathode material). CR2025 coin cells were assembled in an argon-filled glove box (Mbraun) using 1.0 M LiPF₆ in 1:1:1 v/v EC/DC/DMC as electrolyte and Celgard 2250 as separator. The cells were galvanostatically charge-discharged between 1 V and 3 V (vs Li/Li⁺) using a battery tester (Neware Shenzhen, China). The specific capacities and rates reported here are based on the mass of sulfur. Cyclic voltammetry (CV) and electrochemical impedance spectroscopy (EIS) measurements were carried out on a Biologic VMP3 electrochemistry workstation. EIS was handled over the frequency range of 100 kHz to 0.1 Hz and CV analysis was performed at scan rate of 0.1 mV/s.

5.4 Results and Discussion

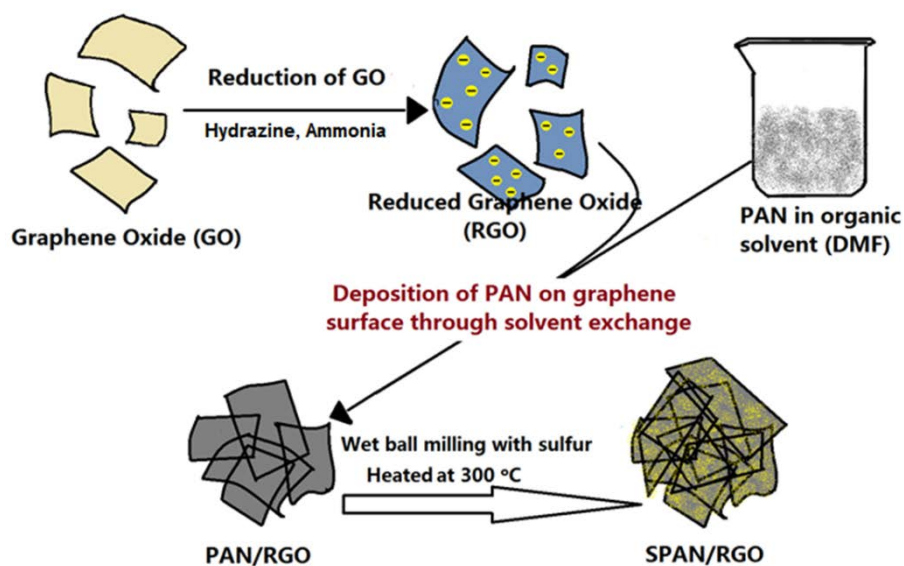


Fig. 5.1 Schematic diagram of the solvent exchange process and synthesis of the SPAN/RGO composite.

The preparation procedure of SAPN/RGO composite is illustrated in Fig. 5.1. Through the process, the exfoliated graphene oxide (GO) sheets in water are converted back to graphene by chemical reduction. Zeta potential measurements confirmed the anionic charge of graphene sheets in water. The exfoliated GO shows a zeta potential of -55.7 mV, whilst that of hydrazine reduced RGO is -43.2 mV. This result implies that the carboxylic acid groups of GO are partially preserved when the reduction is conducted in the presence of ammonia. As a result, RGO can be dispersed due to the electrostatic forces.

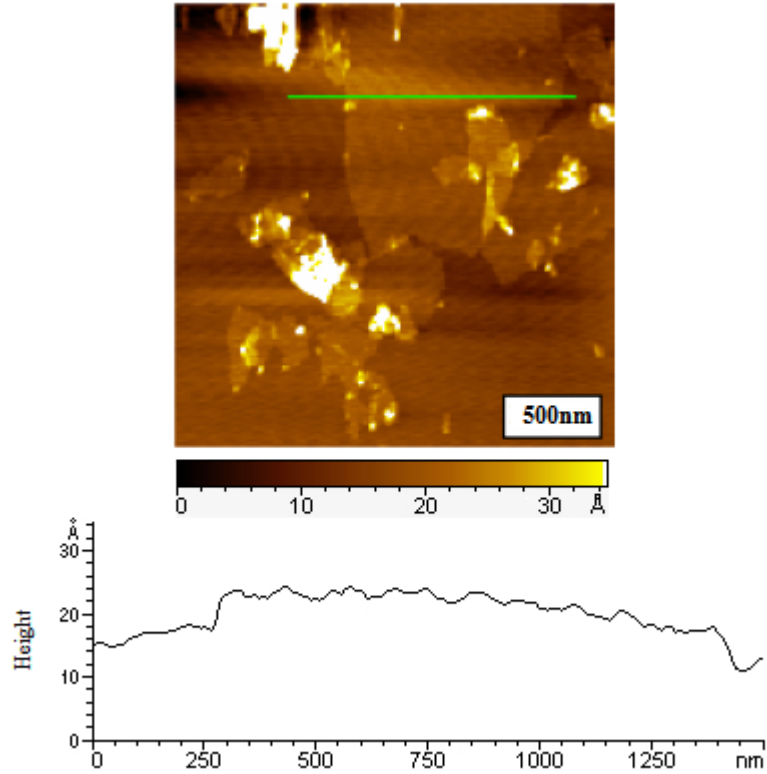


Fig. 5.2 AFM image of RGO sheets on a silicon wafer under tapping-mode with a cross-sectional height profile measured along the green straight line.

RGO sheets cast on a silicon wafer were examined by AFM under tapping mode. Fig. 5.2 shows flat RGO sheets with a thickness of ~ 1 nm, implying the successful exfoliation from graphite to graphene sheets.

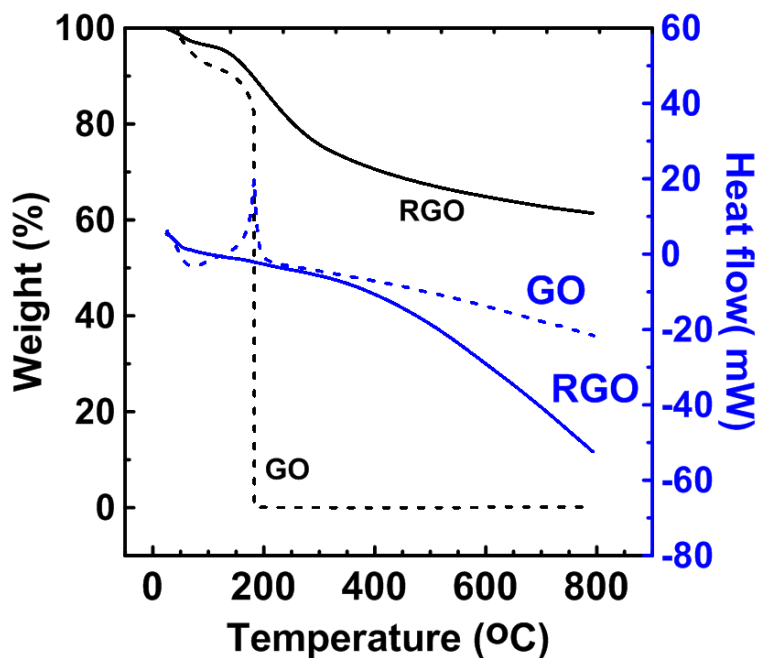


Fig. 5.3 TGA of GO and RGO carried out under N₂ from room temperature to 800 °C.

Fig. 5.3 depicts typical TGA results of GO and RGO. The onset of mass loss for GO occurs at 200 °C, due to the pyrolysis of the labile oxygen containing functional groups leading to total decomposition of the material. The reaction is accompanied by an exothermic peak at 200 °C in the heat flow curve. Conversely, RGO shows about 65 wt. % residual mass after heating to 800 °C, and no obvious exothermic peak is detected in its heat flow curve. This is likely due to an increased thermal stability of the RGO after reduction of the oxygen functional groups and implies the successful formation of graphene.

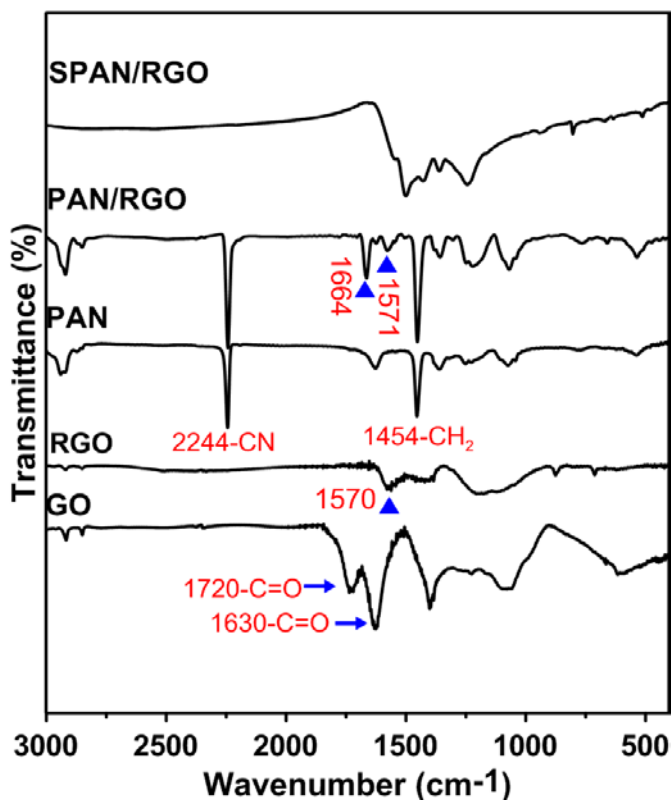


Fig. 5.4 FTIR spectra of GO, RGO, PAN, PAN/RGO, and SPAN/RGO.

The FTIR spectra of intermediates and composite materials are displayed in Fig. 5.4. After reduction of GO, the carboxylic and ketone C=O stretching vibration peaks at 1720 cm^{-1} and 1630 cm^{-1} are no longer observed in RGO pattern, confirming the successful reduction of GO by hydrazine with recovery of graphitic sp^2 configuration from sp^3 . [146] The appearance of the peak at 1570 cm^{-1} , typical of the carboxylate anion group, indicates partial preservation of polar groups from GO. [146,147] In the spectrum of PAN/RGO, the characteristic strong sharp peak at 2244 cm^{-1} (relative to the cyano group stretching vibration) and the medium peak at 2940 cm^{-1} confirm the presence of PAN in the composite. The additional peak located at 1571 cm^{-1} attributes to the remaining carboxyl groups in RGO. Additionally, the peak at 1664 cm^{-1} indicates there might be some interaction between PAN and RGO, such as electrostatic force between the cyano groups of PAN and the polar groups remained on RGO. Furthermore, no apparent shift is observed for the peaks relative to the

polyacrylonitrile functional groups, indicating that PAN is deposited but not covalently bonded to RGO (only electrostatic or long range interactions). On the contrary, the appearance of peaks in the 1000 cm^{-1} – 1750 cm^{-1} range of the SPAN/RGO spectrum, corresponding to the pyrolyzed PAN backbone and the covalent bond between sulfur and carbon in the PAN matrix, [148] implies successful reaction between sulfur and PAN.

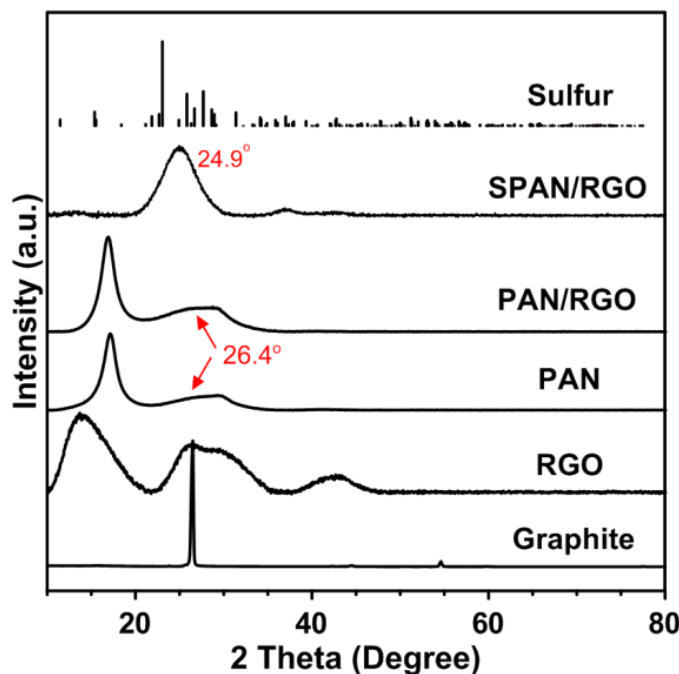


Fig. 5.5 XRD patterns of graphite, RGO, PAN, PAN/RGO, SPAN/RGO, and sulfur.

The results of XRD measurements are presented in Fig. 5.5. The strong and narrow characteristic peak of graphite at 26.4° becomes broad in RGO pattern, and two new broad peaks emerge at 13.3° and 42.6° . This indicates an increase of interlayer spacing of pristine graphite, resulting from the addition of oxygen-containing functional groups after partial reduction of graphene oxide. [123] Besides the typical diffraction of PAN at 16.8° and 28.6° , a weak peak at 26.4° stemming from graphite is observed in the PAN/RGO pattern. However, the strong diffraction peak from RGO at 13.3° vanishes due to the loss of graphitic layer order. In the SPAN/RGO composite with ~44 wt% sulfur and ~3 wt% RGO, a new broad peak at 24.9° appears but no typical characteristic diffraction from sulfur and PAN is observed, indicating the successful reaction between PAN and Sulfur. Sulfur

is in amorphous state within the composite, which seems to be uniformly dispersed in the PAN matrix. [121, 150] The absence of characteristic peak of RGO in SPAN/RGO composite probably results from the low RGO content.

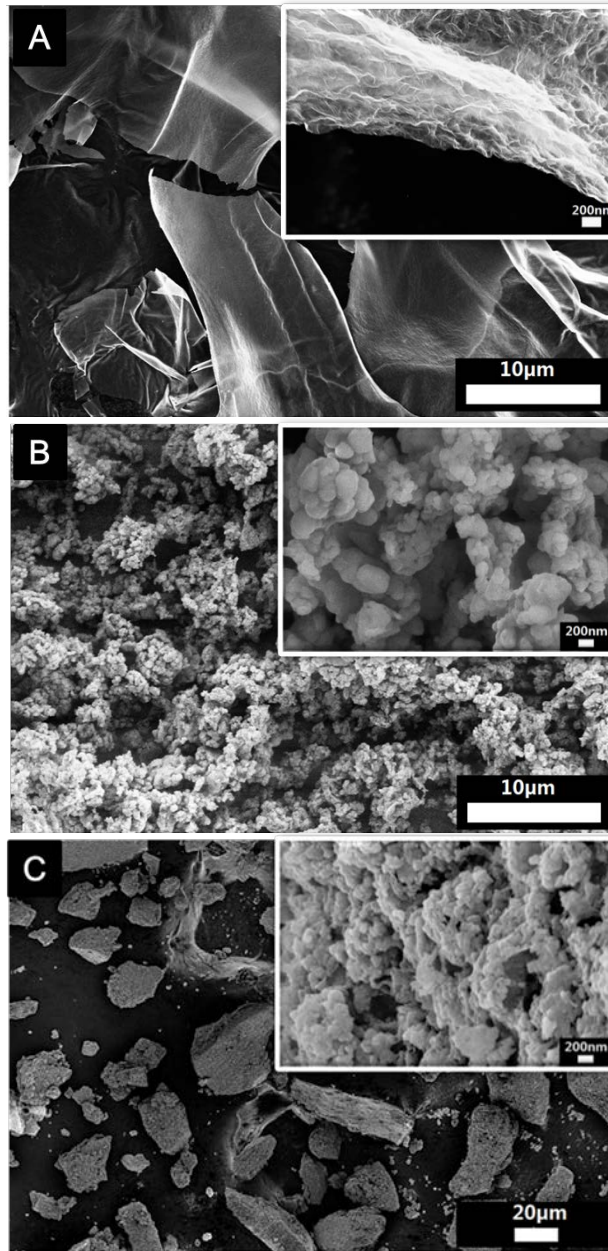


Fig.5.6 SEM images of RGO (A), SPAN (B) and SPAN/RGO (C).

The SEM images of RGO, SPAN/RGO and SPAN (44 wt. % S) composites are shown in Fig. 37. Strong agglomeration was observed in the dried RGO sheets (inset in Fig. 37A). The SPAN composite appears as a loose aggregation of small SPAN particles with average size of 200 nm (Fig. 37B). The morphology of the SPAN/RGO shows large aggregates with primary SPAN particles of much smaller size (around 100 nm) deposited on the surface of graphene, Fig. 37C. Hence, graphene cannot be identified in the SEM.

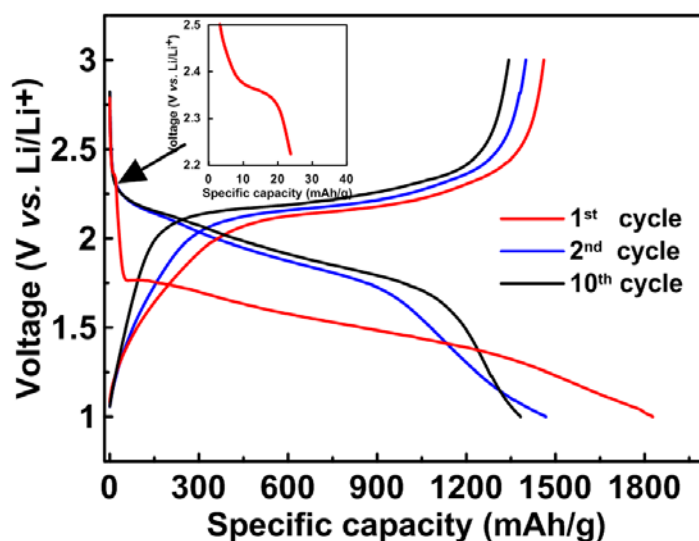


Fig.5.7 Voltage vs. capacity profile of SPAN/RGO electrode (44 wt% sulfur) at 0.1 C rate between 1.0-3.0 V.

Galvanostatic discharge/charge curves of SPAN/RGO composite with 44 wt% sulfur at 0.1 C rate are depicted in Fig. 5.7. The initial discharge capacity of the composite is 1827 mAh/g, which is much higher than the theoretical capacity of sulfur (1675 mAh/g). The extra capacity is due to the irreversible insertion of lithium into the conjugated π -system of the PAN backbone. [149] In the second cycle, a reversible capacity of 1470 mAh/g was achieved indicating 90% sulfur utilization. There is a very short potential plateau at ~ 2.35 V and a longer one at ~ 1.65 V in the first discharge curve. However, these two plateaus can hardly be distinguished in the 2nd and following cycles. Instead, only one potential plateau at about 1.8 V is portrayed. Additionally, the discharge/charge

plateaus shift to higher values from the 1st to 10th cycle. Theoretically, there are two potential plateaus corresponding to the two-step reaction of sulfur with lithium at ~2.4 V and 2.1 V, respectively. The lower potential for the second discharge plateau in the initial cycle is provoked by the additional energy needed to dissociate sulfur from the covalent bond with carbon in PAN backbone. Additionally, the highly dispersed elemental sulfur in short chain configurations inside the PAN matrix also contributes to the lower potential in the initial discharge due to their high energy state compared with large molecules of sulfur in crown ring structures. [151,152] The shorter potential plateau in the initial discharge (inset) indicates the existence of a very small amount of elemental sulfur which is not bound with PAN backbone. The shift in potential upon cycling is mainly due to the formation of the complexes with lower absorbing energy. [152]

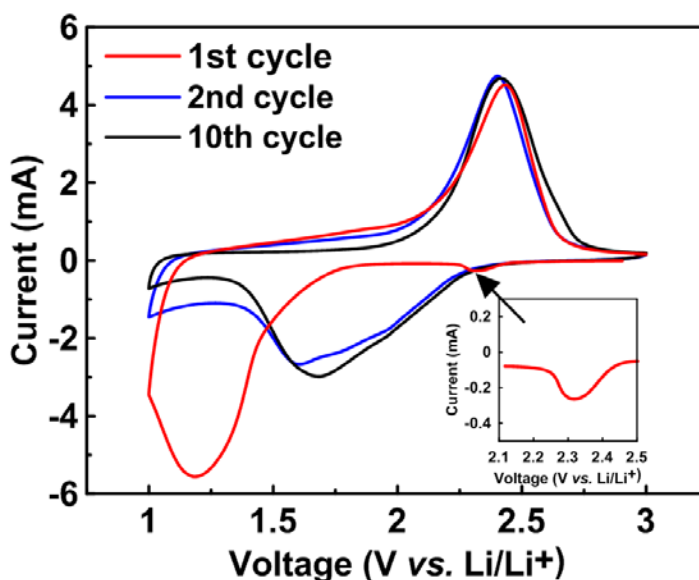


Fig.5.8 Cyclic voltammograms of SPAN/RGO composite electrode at a scanning rate of 0.1 mV/s .

Fig. 5.8 shows the cyclic voltammograms of SPAN/RGO composite at a scanning rate of 0.1 mV/s. In the first cycle, it presents a weak cathodic peak at 2.35 V and a strong cathodic peak at 1.21 V, corresponding to the two-step reaction between lithium and sulfur. A strong anodic peak appears at 2.4 V, assigned to lithium ion extraction from Li_2S_n . In the subsequent cycles, the cathodic peak at

2.35 V disappears, while the cathodic peak at 1.21 V shifts positively, reaching 1.69 V in the 10th cycle. However, the anodic peak has only slight negative shift. These results are in good agreement with the charge-discharge curves.

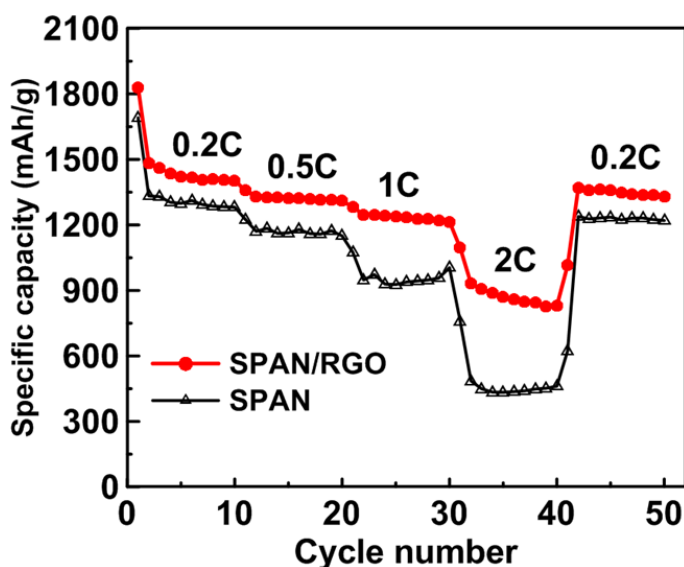


Fig.5.9 Discharge capacity of SPAN and SPAN/RGO (3 wt% RGO content) electrodes at different C-rates.

The results of rate performance studies of the SPAN and SPAN/RGO composite electrodes are shown in Fig. 5.9. The discharge capacities of SPAN decrease steeply with increasing discharge rate, whereas the SPAN/RGO composite with ~3 wt% graphene shows a much slower decline. The ternary composite delivers high capacities at relative high C-rates, namely, 1292 mAh/g at 0.5 C, 1180 mAh/g at 1 C, and 828 mAh/g at 2 C. Moreover, it shows good capacity recovery, with ~96% of the initial value attained at 0.2 C rate after high rate cycling, indicating that the structure of the composite is very stable. Comparatively, the composite SPAN cathode without RGO delivers only half of the reversible capacity attained by the SPAN/RGO composite at 2 C rate. This implies the SPAN/RGO composite has better conductivity confirming that the presence of highly conductive graphene sheets is instrumental to enhance the high rate performance in the sulfur-polymer cathode.

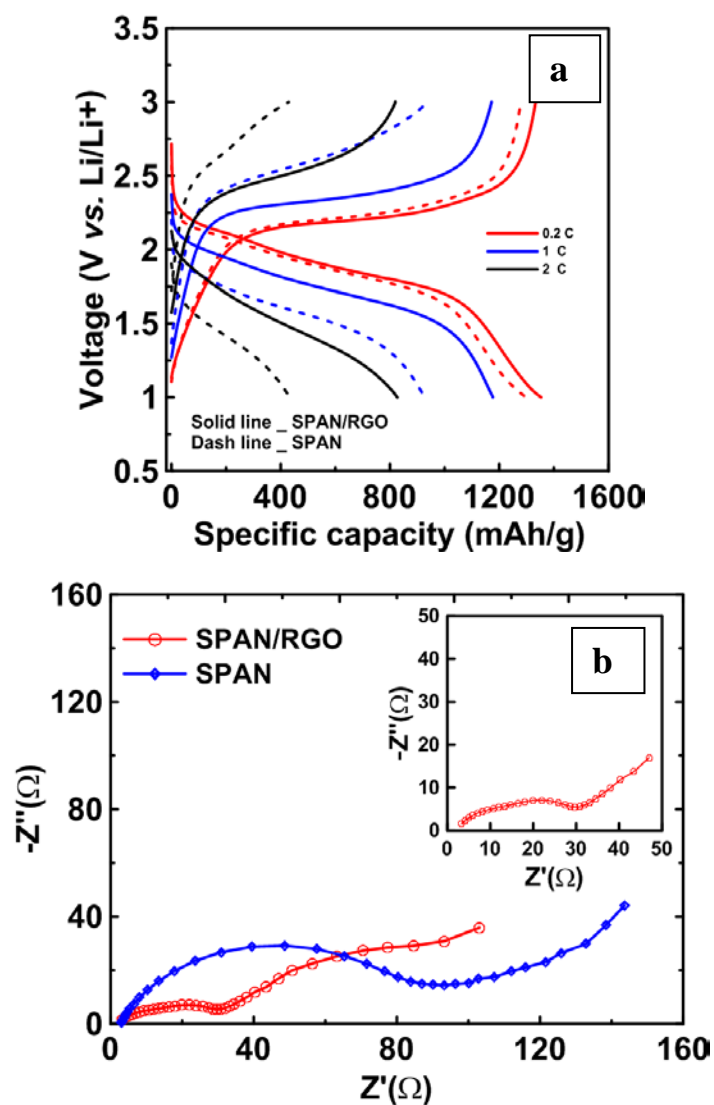


Fig.10 (a) Fifth galvanostatic discharge/charge curves of SPAN and SPAN/RGO at different rates and (b) EIS spectra of SPAN/RGO and SPAN composites with 44 wt% S after the 10th discharge to 1 V at 0.1 C rate, the inset is the enlarged image of SPAN/RGO spectra.

A close examination of the galvanostatic discharge and charge curves of SPAN and SPAN/RGO at different C-rates allows for the inspection of the effectiveness of RGO in reducing the potential polarization due to increased electrode resistance. As seen in Fig. 10a, the polarization of the SPAN/RGO composite electrode increases much more slowly than that of the SPAN composite upon increasing C-rate. This suggests that graphene significantly improves the electronic conductivity of

the composite. EIS analysis of the SPAN/RGO and SPAN composites after the 10th discharge (Fig.10b) corroborates the rate capability results. The SPAN/RGO composite has much lower charge transfer resistance, manifested by the smaller semi-circle at middle frequency.

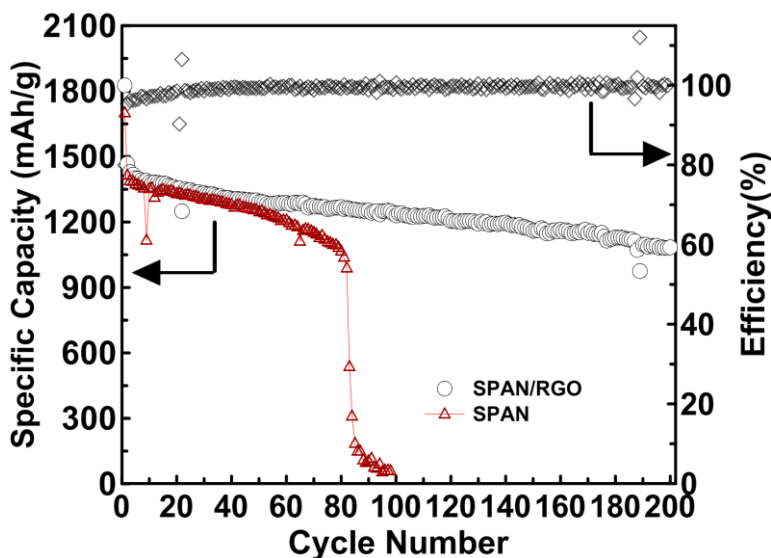


Fig.5.11 Cycling performance of SPAN/RGO and SPAN composite electrodes at C/10 rate.

The cycling performance of SPAN/RGO and SPAN at 0.1 C rate is shown in Fig. 42. Both composites with and without RGO show similar capacity performance within the first 20 cycles. However, the SPAN composite cathode starts rapid capacity decay after 40 cycles, losing about 25% capacity by the 80th cycle. It eventually reaches 0 mAh/g at the 100th cycle, which may be attributed to the dendrite growth due to the corrosion of the anode surface caused by the polysulfide shuttle. [153] Conversely, the SPAN/RGO composite with 3 wt. % RGO exhibits excellent cycle stability. After 100 cycles, the electrodes show overall 85% retention of the initial reversible capacity of 1467 mAh/g. Following the first discharge, the capacity rapidly decreases to 1385 mAh/g in 10 cycles. Nevertheless, the SPAN/RGO composite delivers 1100 mAh/g by the 200th cycle, which means 80% capacity retention within the last 190 cycles. Noteworthy, the columbic efficiency of the composite is close to 100% after 20 cycles, implying a very minute amount of shuttle effect.

The RGO sheets impart good conductivity and high surface area to the SPAN/RGO composite, providing a robust electron transport framework. In addition, the flexible graphene framework reinforces the structural stability of the electrode and enables the composite to accommodate the volume change of sulfur compounds during charge and discharge. [139-142] On the other hand, the presence of PAN in the composite helps maintain the polysulfides within the electrode. As a result, electrochemical polarization and the shuttle effect of polysulfides are suppressed, and the overall electrical performance of the sulfur cathode was significantly improved.

5.5 Conclusions

A SPAN/RGO composite was successfully synthesized *via* deposition of PAN on the surface of reduced graphene oxide sheets followed by ball milling with sulfur and heat treatment. The SPAN/RGO composite with 3 wt.% RGO and 44 wt.% sulfur shows good overall electrochemical performance, exhibiting ~85% retention of the initial reversible capacity of 1467 mAh/g over 100 cycles at a constant current rate of 0.1 C. After 200 cycles, the reversible capacity is still as high as 1100 mAh/g. The composite demonstrate excellent rate capability, delivering up to 828 mAh/g reversible capacity at 2 C, as well as high Coulombic efficiency. The improved performance stems from composition and structure of the composite, wherein RGO is shown to enhance electronic conductivity and PAN acts as sulfur/polysulfide absorber.

Chapter 6

Summary and perspective towards furthered work

Rechargeable lithium sulfur (Li-S) batteries are safe, environmentally friendly and economical alternative energy storage systems that can potentially be combined with renewable sources including wind solar and wave energy. Sulfur has a high theoretical specific capacity of ~1680 mAh/g, attainable through the reversible redox reaction denoted as $S_8 + 16Li \leftrightarrow 8Li_2S$, which yields an average cell voltage of ~2.2 V. However, two detrimental factors prevent the achievement of the full potential of the Li-S batteries. First, the poor electrical/ionic conductivity of elemental sulfur and Li_2S severely hampers the utilization of active material for obtaining full capacity of the electrode. Second, dissolution of intermediate long-chain polysulfides (Li_2S_n , $2 < n < 7$) into the electrolyte and their shuttle between cathode and anode leads to fast capacity degradation and low Coulombic efficiency. As a result of this shuttle process, insoluble and insulating Li_2S/Li_2S_2 precipitates on the surface of electrodes causing loss of active material and rendering the electrodes surface electrochemically inactive.

Graphene has been intensively investigated for enhancing the rate and cycling performance of lithium sulfur batteries. Graphene, which has a two-dimensional, one-atom-thick nanosheet structure, offers extraordinary electronic, thermal and mechanical properties. In order to solve the aforementioned problems within lithium-sulfur batteries, graphene has been successfully introduced to the Sulfur-PAN system. A SPAN/RGO composite was successfully synthesized *via* deposition of PAN on the surface of reduced graphene oxide sheets followed by ball milling with sulfur and heat treatment. The SPAN/RGO composite with 3 wt.% RGO and 44 wt.% sulfur shows good overall electrochemical performance, exhibiting ~85% retention of the initial reversible capacity of 1467 mAh/g over 100 cycles at a constant current rate of 0.1 C. After 200 cycles, the reversible capacity is still as high as 1100 mAh/g. The composite demonstrate excellent rate capability, delivering up to 828 mAh/g reversible capacity at 2 C, as well as high coulombic efficiency. The improved

performance stems from composition and structure of the composite, wherein RGO is shown to enhance electronic conductivity and PAN acts as sulfur/polysulfide absorber.

However it is still necessary to further explore the effect of the addition of different amount of RGO to the structure and electrochemical properties of the composite. It is also interesting to investigate the degree to reduce GO, because it would influence the conductivity of RGO.

This system shows excellent overall electrochemical performance, however, the capacity fading is still obvious. In order to achieve high retainable energy density of lithium-sulfur batteries, there will be a lot of challenges in the future. It will be necessary to look for appropriate electrolyte or electrolyte additives to suppress the dissolution of polysulfide. If we want to explore the full potential of Li-S batteries, it is also necessary to find a proper anode material which has a comparable capacity and low plateau potential. In summary, solving the problems within the sulfur cathode and exploring proper and stable anodes will be future challenges of Li-S cells.

Appendix A

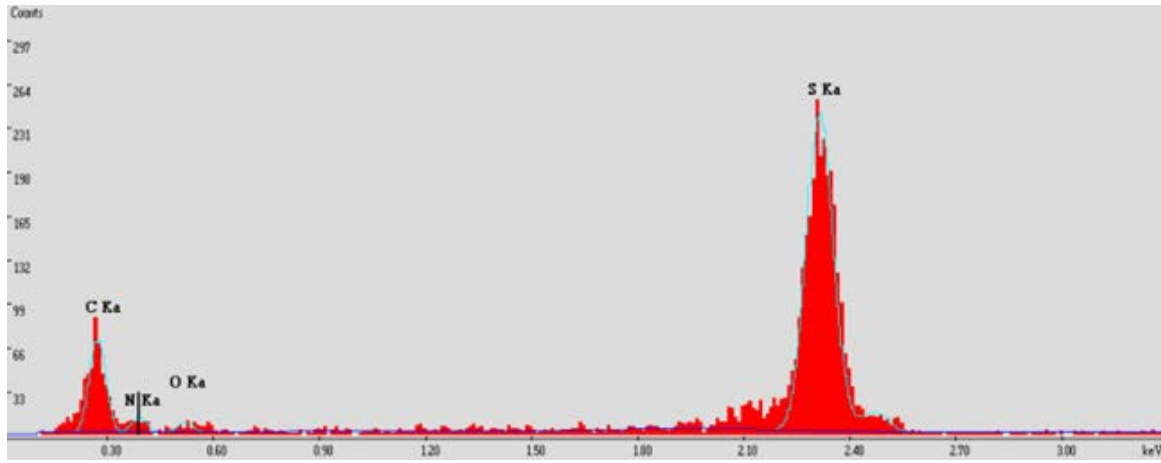


Fig. 1 EDS spectrum of a sulfur-polyacrylonitrile/graphene sample.

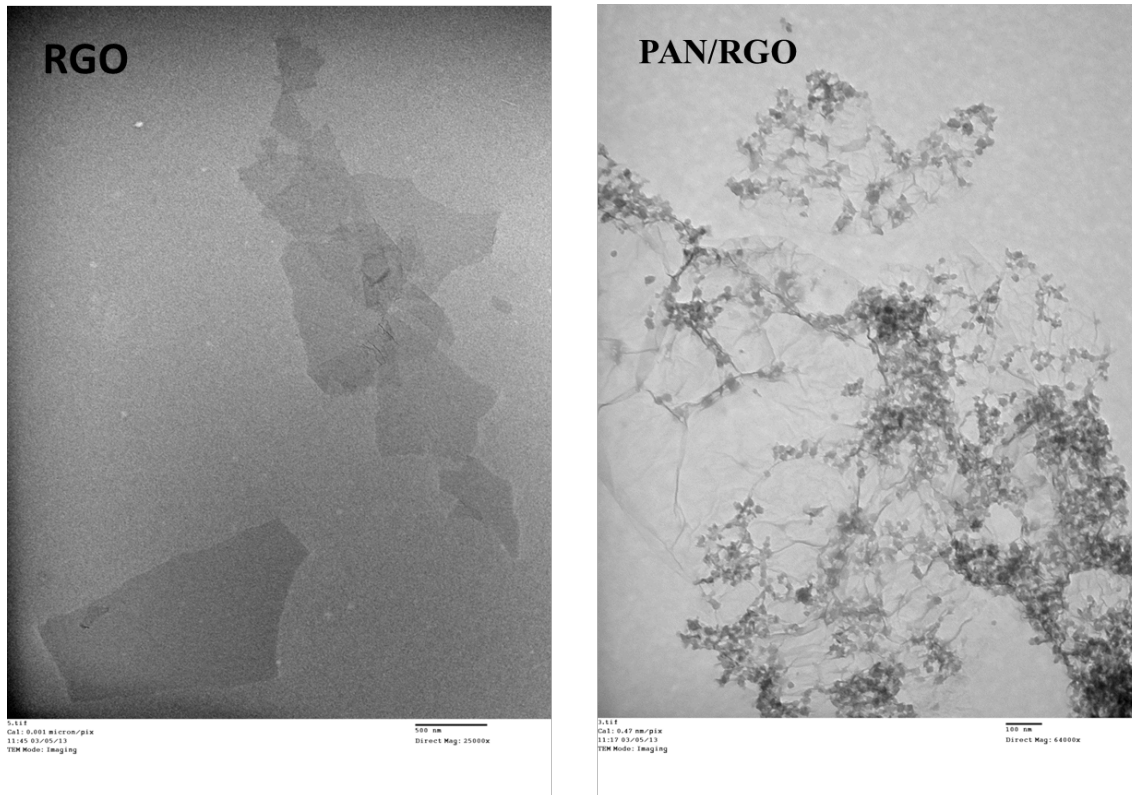
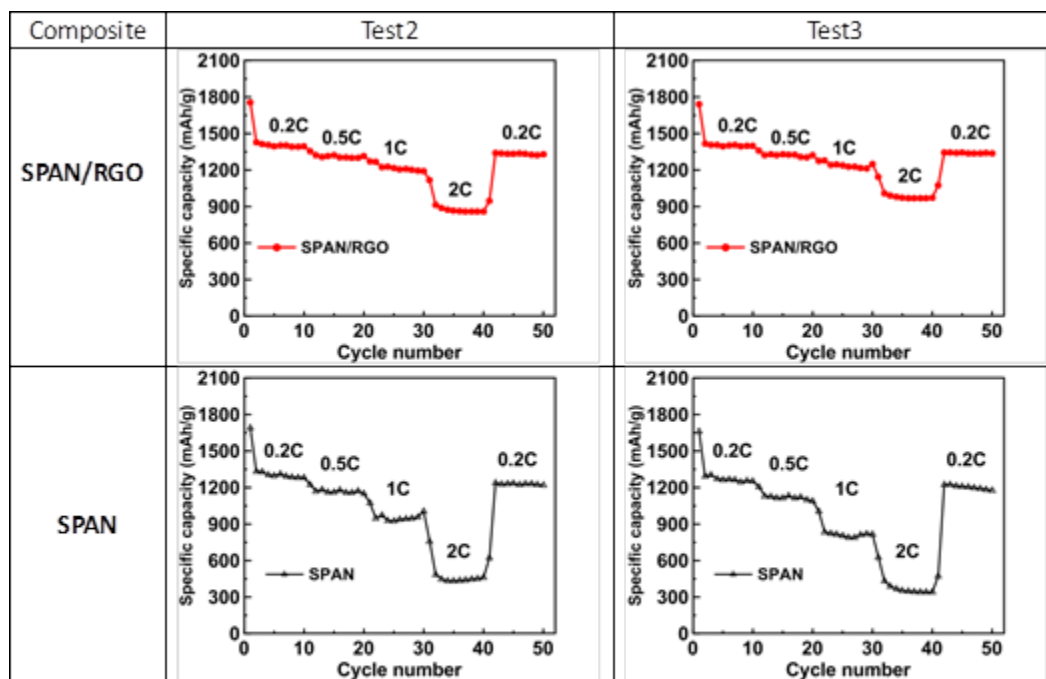


Fig.2 TEM of RGO and PAN/RGO

Appendix B



**Reproducible data of C-rate performance of the SPAN/RGO composite
and SPAN composite**

Bibliography

- [1] V. Etacheri, R. Marom, R. Elazari, G. Salitra, and D. Aurbach, "Challenges in the development of advanced Li-ion batteries: a review," *Energy & Environmental Science*, vol. 4, no. 9, p. 3243, 2011.
- [2] B. Scrosati and J. Garche, "Lithium batteries: Status, prospects and future," *Journal of Power Sources*, vol. 195, no. 9, pp. 2419–2430, May 2010.
- [3] A. Manthiram, "Materials Challenges and Opportunities of Lithium Ion Batteries," *The Journal of Physical Chemistry Letters*, vol. 2, no. 3, pp. 176–184, Feb. 2011.
- [4] D. Coup, "Toyota's approach to alternative technology vehicles: The power of diversification strategies," *Corp. Environ. Strategy*, vol. 6, no. 3, pp. 258-269, 1999.
- [5] X. Ji and L. F. Nazar, "Advances in Li–S batteries," *Journal of Materials Chemistry*, vol. 20, no. 44, p. 9821, 2010.
- [6] Y. V. Mikhaylik and J. R. Akridge, "Polysulfide Shuttle Study in the Li/S Battery System," *Journal of The Electrochemical Society*, vol. 151, no. 11, p. A1969, 2004.
- [7] G. He, X. Ji, and L. Nazar, "High 'C' rate Li-S cathodes: sulfur imbibed bimodal porous carbons," *Energy & Environmental Science*, vol. 4, no. 8, p. 2878, 2011.
- [8] A. Yoshino, K. Jitsuchika, T. Nakashima, Japanese Patent 1989293 (issued 1985/5/10)
- [9] T. Nagura, K. Tozawa, *Progr. Batteries Solar Cells*, vol.10, p.218, 1991.
- [10] M. Yoshio, R. J. Brodd, A. Kozawa, Ed., "*Lithium-Ion Batteries: Science and Technologies*," Springer Science+Business Media, 2009.
- [11] J.B. Goodenough, U.S. Patent 4,302,518 (issued 1980/3/31)
- [12] H. Ikeda, K. Narukawa, H. Nakashim, Japanese Patent 1769661 (issued 1981/6/18)
- [13] S. Basu, U.S. Patent 4,423,125 (issued 1982/9/13)
- [14] B. Scrosati, *Electrochemistry of Novel Materials*, VCH Publishers, 1993.
- [15] L. Ji, Z. Lin, M. Alcoutlabi and X. Zhang, "Recent developments in nanostructured anode materials for rechargeable lithium-ion batteries," *Energy & Environmental Science*, vol. 4, no. 8, p. 2682, 2011.

- [16] J. Chen, J. Z. Wang, A. I. Minett, Y. Liu, C. Lynam, H. K. Liu and G. G. Wallace, "Carbon nanotube network modified carbon fibre paper for Li-ion batteries," *Energy & Environmental Science*, vol. 2, p. 393, 2009.
- [17] B. J. Landi, M. J. Ganter, C. D. Cress, R. A. DiLeo and R. P. Raffaele, "Carbon nanotubes for lithium ion batteries," *Energy & Environmental Science*, vol. 2, p. 638, 2009.
- [18] M. R. Palacin, "Recent advances in rechargeable battery materials: a chemist's perspective," *Chemical Society Reviews*, vol. 38, p. 2565, 2009.
- [19] H. Zhang, G. P. Cao and Y. S. Yang, "Carbon nanotube arrays and their composites for electrochemical capacitors and lithium-ion batteries," *Energy & Environmental Science*, vol. 2, p. 932, 2009.
- [20] Y. G. Guo, J. S. Hu and L. J. Wan, "Nanostructured materials for electrochemical energy conversion and storage devices," *Advanced Materials*, vol. 20, p. 2878, 2008.
- [21] J. M. Tarascon, N. Reham, M. Armand, J. N. Chotard, P. Barpanda, W. Walker and L. Dupont, "Hunting for Better Li-Based Electrode Materials via Low Temperature Inorganic Synthesis," *Chemistry of Materials*, vol. 22, p. 724, 2010.
- [22] M. Armand, S. Grugeon, H. Vezin, S. Laruelle, P. Ribiere, P. Poizot and J. M. Tarascon, "Conjugated dicarboxylate anodes for Li-ion batteries," *Nature Materials*, vol. 8, p. 120, 2009.
- [23] H. Li, Z. X. Wang, L. Q. Chen and X. J. Huang, "Research on Advanced Materials for Li - ion Batteries," *Advanced Materials*, vol. 21, p. 4593, 2009.
- [24] B. Peng and J. Chen, "Functional materials with high-efficiency energy storage and conversion for batteries and fuel cells," *Coordination Chemistry Reviews*, vol. 253, p. 2805, 2009.
- [25] A. K. Padhi, K. S. Nanjundaswamy and J. B. Goodenough, "Phospho - olivines as Positive - Electrode Materials for Rechargeable Lithium Batteries," *Journal of The Electrochemical Society*, vol. 144, p. 1188, 1997.

- [26] R. V. Chebiam, A. M. Kannan, F. Prado, and A. Manthiram, "Comparison of the Chemical Stability of High Energy Density Cathodes of Lithium-Ion Batteries," *Electrochemistry Communications*, vol. 3, p. 624, 2001.
- [27] J. Choi, E. Alvarez, T. A. Arunkumar and A. Manthiram, "Proton Insertion into Oxide Cathodes During Chemical Delithiation," *Electrochemical and Solid-State Letters*, vol. 9, p. 241, 2006.
- [28] S. Whittingham, "Lithium batteries and cathode materials," *Chemical Reviews-Columbus*, , vol. 104, p. 4271, 2004.
- [29] T. Ohzuku and Y. Makimura, "Layered Lithium Insertion Material of $\text{LiCo}_{1/3}\text{Ni}_{1/3}\text{Mn}_{1/3}\text{O}_2$ for Lithium-Ion Batteries," *Chemistry Letters*, vol. 30, p. 642, 2001.
- [30] Z. Lu, D. D. MacNeil and J. R. Dahn, "Layered cathode materials $\text{Li}[\text{Ni}_x\text{Li}_{(1/3-2x/3)}\text{Mn}_{(2/3-x/3)}]\text{O}_2$ for lithium-ion batteries," *Electrochemical and Solid-State Letters*, vol. 4, p. 200, 2001.
- [31] R. J. Gummow, A. de Kock, and M. M. Thackeray, "Improved Capacity Retention in Rechargeable 4 V Lithium/Lithium-Manganese Oxide (Spinel) Cells," *Solid State Ionics*, vol. 69, p. 59, 1994.
- [32] D. H. Jang, Y. J. Shin, and S. M. Oh, "Dissolution of Spinel Oxides and Capacity Losses in 4 V $\text{Li}/\text{Li}_x\text{Mn}_2\text{O}_4$ Cells," *Journal of Electrochemistry Society*, vol. 143, p. 2204, 1996.
- [33] Y. Shin and A. Manthiram, "Factors Influencing the Capacity Fade of Spinel Lithium Manganese Oxides," *Journal of Electrochemistry Society*, vol. 151, p. 204, 2004.
- [34] W. Choi and A. Manthiram, "Superior Capacity Retention Spinel Oxyfluoride Cathodes for Lithium Ion Batteries," *Electrochemical and Solid-State Letters*, vol. 9, p. 245, 2006.
- [35] S. Y. Chung, J. T. Bloking and Y. M. Chiang, "Electronically Conductive Phospho-olivines as Lithium Storage Electrodes," *Nature materials*, vol. 1, p. 123, 2002.
- [36] B. Ellis, W. H. Kan, W. RM. Makahnouk and L.F. Nazar, "Synthesis of Nanocrystals and Morphology Control of Hydrothermally Prepared LiFePO_4 ," *Journal of Materials Chemistry*, vol. 17, pp. 3248–3254, 2007.

- [37] J. B. Goodenough and Y. Kim, "Challenges of Rechargeable Lithium Batteries," *Chemistry of Materials*, vol. 22, pp. 587–603, 2010.
- [38] X. Ji, K. T. Lee, and L. F. Nazar, "A highly ordered nanostructured carbon-sulphur cathode for lithium-sulphur batteries.," *Nature materials*, vol. 8, no. 6, p. 500, Jun. 2009.
- [39] K. Kang, Y. S. Meng, J. Bréger, C. P. Grey, and G. Ceder, "Electrodes with high power and high capacity for rechargeable lithium batteries," *Science*, vol. 311, pp. 977–980, 2006.
- [40] V. S. Kolosnitsyn and E. V. Karaseva, "Lithium-sulfur batteries: Problems and solutions," *Russian Journal of Electrochemistry*, vol. 44, no. 5, pp. 506–509, Jun. 2008.
- [41] S.-E. Cheon, K.-S. Ko, J.-H. Cho, S.-W. Kim, E.-Y. Chin, and H.-T. Kim, "Rechargeable Lithium Sulfur Battery," *Journal of The Electrochemical Society*, vol. 150, no. 6, p. A800, 2003.
- [42] H. Yamin, A. Gorenstein, J. Penciner, Y. Sternberg, and E. Peled, "Lithium sulfur battery oxidation/reduction mechanisms of polysulfides in THF solutions," *Journal of The Electrochemical Society*, vol. 135, p. 1045, 1988.
- [43] H. Yamin, J. Penciner, A. Gornenshtain, M. Elam, and E. Peled, "Rechargeable lithium sulfur battery," *Journal of Power Sources*, vol. 14, p. 129, 1985.
- [44] E. Peled, A. Gorenstein, M. Segal, and Y. Sternberg, *Journal of Power Sources*, vol. 26, p. 269, 1989.
- [45] R. D. Raugh, K. M. Abraham, G. F. Pearson, Y. K. Suprenant, and S. B. Brummer, "A lithium/dissolved sulfur battery with an organic electrolyte," *Journal of The Electrochemical Society*, vol. 126, p. 523, 1979.
- [46] E. Strauss D. Golodnitsky, and E. Peled, "Study of phase changes during 500 full cycles of Li/composite polymer electrolyte/FeS₂ battery," *Electrochemical Acta*, vol. 45, p. 1519, 2000.

- [47] R. D. Rauh, K. M. Abraham, G. F. Pearson, J. K. Surprenant and S. B. Brummer, "A lithium/dissolved sulfur battery with an organic electrolyte," *Journal of The Electrochemical Society*, vol. 126, p. 523, 1979.
- [48] H. Yamin and E. Peled, "Electrochemistry of a nonaqueous lithium/sulfur cell," *Journal of Power Sources*, vol. 9, p. 28, 1983.
- [49] P. G. Bruce, S. a Freunberger, L. J. Hardwick, and J.-M. Tarascon, "Li-O₂ and Li-S batteries with high energy storage," *Nature materials*, vol. 11, no. 1, pp. 19–29, 2012.
- [50] S. Wei, H. Zhang, Y. Huang, W. Wang, Y. Xia, and Z. Yu, "Pig bone derived hierarchical porous carbon and its enhanced cycling performance of lithium–sulfur batteries," *Energy & Environmental Science*, vol. 4, no. 3, p. 736, 2011.
- [51] V. S. Kolosnitsyn and E. V. Karaseva, "Lithium-sulfur batteries: Problems and solutions," *Russian Journal of Electrochemistry*, vol. 44, no. 5, pp. 506–509, Jun. 2008.
- [52] V. S. Kolosnitsyn, E. V. Karaseva, N. A. Amineva and G. A. Batyrshina, "Cycling Lithium–Sulfur Batteries," *Russian Journal of Electrochemistry*, vol. 38, p. 329, 2002.
- [53] V. S. Kolosnitsyn, E. V. Karaseva, D. Y. Seung and M. D. Cho, "Cycling a Sulfur Electrode in Mixed Electrolytes Based on Sulfolane: Effect of Ethers," *Russian Journal of Electrochemistry*, vol. 38, p. 1314, 2002.
- [54] V. S. Kolosnitsyn, E. V. Karaseva, and A. L. Ivanov, "Electrochemistry of a lithium electrode in lithium polysulfide solutions," *Russian Journal of Electrochemistry*, vol. 44, p. 564, 2008.
- [55] V. S. Kolosnitsyn, E. V. Karaseva, D. Y. Seung and M. D. Cho, "Cycling a Sulfur Electrode: Effect of Physicochemical Properties of Electrolyte Systems," *Russian Journal of Electrochemistry*, vol. 39, p. 1089, 2003.
- [56] S.-E. Cheon, K.-S. Ko, J.-H. Cho, S.-W. Kim, E.-Y. Chin, and H.-T. Kim, "Rechargeable Lithium Sulfur Battery," *Journal of The Electrochemical Society*, vol. 150, no. 6, p. A796, 2003.

- [57] N. W. James R. Akridge, Yuriy V. Mikhaylik, "Li/S fundamental chemistry and application to high-performance rechargeable batteries," *Solid State Ionics*, vol. 175, no. 1–4, pp. 243–245, Nov. 2004.
- [58] Y. V. Mikhaylik and J. R. Akridge, "Polysulfide Shuttle Study in the Li/S Battery System," *Journal of The Electrochemical Society*, vol. 151, no. 11, p. A1969, 2004.
- [59] K. Kumaresan, Y. Mikhaylik, and R. E. White, "A Mathematical Model for a Lithium–Sulfur Cell," *Journal of The Electrochemical Society*, vol. 155, no. 8, p. A576, 2008.
- [60] C. Barchasz, F. Molton, C. Duboc, J.-C. Leprêtre, S. Patoux, and F. Alloin, "Lithium/sulfur cell discharge mechanism: an original approach for intermediate species identification.," *Analytical chemistry*, vol. 84, no. 9, pp. 3973–80, 2012.
- [61] J. A. Dean, "Lange's handbook of chemistry," *McGraw Hill Book Co., New York, NY*, Jan. 1985.
- [62] Y. Cao, X. Li, I. a Aksay, J. Lemmon, Z. Nie, Z. Yang, and J. Liu, "Sandwich-type functionalized graphene sheet-sulfur nanocomposite for rechargeable lithium batteries," *Physical chemistry chemical physics*, vol. 13, no. 17, pp. 7660–5, May 2011.
- [63] X. Ji and L. F. Nazar, "Advances in Li–S batteries," *Journal of Materials Chemistry*, vol. 20, no. 44, p. 9821, 2010.
- [64] X. Ji, K. T. Lee, and L. F. Nazar, "A highly ordered nanostructured carbon-sulphur cathode for lithium-sulphur batteries," *Nature materials*, vol. 8, no. 6, pp. 500–6, Jun. 2009.
- [65] B. Scrosati, J. Hassoun, and Y.-K. Sun, "Lithium-ion batteries. A look into the future," *Energy & Environmental Science*, vol. 4, no. 9, p. 3287, 2011.
- [66] P. G. Bruce, S. a Freunberger, L. J. Hardwick, and J.-M. Tarascon, "Li-O₂ and Li-S batteries with high energy storage," *Nature materials*, vol. 11, no. 1, pp. 19–29, Jan. 2012.
- [67] R. Ryoo, S. H. Joo, M. Kruk, and M. Jaroniec, "Ordered Mesoporous Carbons," *Advanced Materials*, vol. 13, no. 9, pp. 677–681, May 2001.
- [68] Billur Sakintuna; Yuda Yu, "Templated Porous Carbons: A Review Article." *Ind. Eng. Chem. Res.*, pp. 44, 2893–2902, 2005.

- [69] G. He, X. Ji, and L. Nazar, "High 'C' rate Li-S cathodes: sulfur imbibed bimodal porous carbons," *Energy & Environmental Science*, vol. 4, no. 8, p. 2878, 2011.
- [70] X. Ji, K. T. Lee, and L. F. Nazar, "A highly ordered nanostructured carbon-sulphur cathode for lithium-sulphur batteries," *Nature materials*, vol. 8, no. 6, pp. 500–6, Jun. 2009.
- [71] B. Zhang, X. Qin, G. R. Li, and X. P. Gao, "Enhancement of long stability of sulfur cathode by encapsulating sulfur into micropores of carbon spheres," *Energy & Environmental Science*, vol. 3, no. 10, p. 1531, 2010.
- [72] C. Liang, N. J. Dudney, and J. Y. Howe, "Hierarchically Structured Sulfur/Carbon Nanocomposite Material for High-Energy Lithium Battery," *Chemistry of Materials*, vol. 21, no. 19, pp. 4724–4730, Oct. 2009.
- [73] R. L. Liu, Y. F. Shi, Y. Wan, Y. Meng, F. Q. Zhang, D. Gu, Z. X. Chen, B. Tu and D. Y. Zhao, *J. Am. Chem. Soc.*, 2006, 128, 11652.
- [74] C. Zhang, H. Bin Wu, C. Yuan, Z. Guo, and X. W. D. Lou, "Confining Sulfur in Double-Shelled Hollow Carbon Spheres for Lithium-Sulfur Batteries," *Angewandte Chemie International Edition*, p. n/a–n/a, Aug. 2012.
- [75] X. Wang, Qunqing. Li, Jing. Xie, Zhong. Jin, Jinyong. Wang, Yan. Li, Kaili. Jiang, and Shoushan. Fan, "Fabrication of Ultralong and Electrically Uniform Single-Walled Carbon Nanotubes on Clean Substrates," *Nano Letters*, vol. 9, pp. 3137–3141, 2009.
- [76] S. Gullapalli and M. S. Wong, "Nanotechnology: A Guide to Nano-Objects," *Chemical Engineering Progress*, vol. **107**, pp. 28–32, 2011.
- [77] C. Jia-jia, J. Xin, S. Qiu-jie, W. Chong, Z. Qian, Z. Ming-sen, and D. Quan-feng, "The preparation of nano-sulfur/MWCNTs and its electrochemical performance," *Electrochimica Acta*, vol. 55, no. 27, pp. 8062–8066, Nov. 2010.
- [78] J. Chen, Q. Zhang, Y. Shi, L. Qin, Y. Cao, M. Zheng, and Q. Dong, "A hierarchical architecture S/MWCNT nanomicrosphere with large pores for lithium sulfur batteries.," *Physical chemistry chemical physics : PCCP*, vol. 14, no. 16, pp. 5376–82, Apr. 2012.

- [79] G. Zheng, Y. Yang, J. J. Cha, S. S. Hong, and Y. Cui, "Hollow carbon nanofiber-encapsulated sulfur cathodes for high specific capacity rechargeable lithium batteries.," *Nano letters*, vol. 11, no. 10, pp. 4462–7, Oct. 2011.
- [80] J. Guo, Y. Xu, and C. Wang, "Sulfur-impregnated disordered carbon nanotubes cathode for lithium-sulfur batteries.," *Nano letters*, vol. 11, no. 10, pp. 4288–94, Oct. 2011.
- [81] F. Zhang, X. Zhang, Y. Dong, and L. Wang, "Facile and effective synthesis of reduced graphene oxide encapsulated sulfur via oil/water system for high performance lithium sulfur cells," *Journal of Materials Chemistry*, vol. 22, no. 23, p. 11452, 2012.
- [82] H. Wang, Y. Yang, Y. Liang, J. T. Robinson, Y. Li, A. Jackson, Y. Cui, and H. Dai, "Graphene-wrapped sulfur particles as a rechargeable lithium-sulfur battery cathode material with high capacity and cycling stability.," *Nano letters*, vol. 11, no. 7, pp. 2644–7, Jul. 2011.
- [83] Y.-X. Wang, L. Huang, L.-C. Sun, S.-Y. Xie, G.-L. Xu, S.-R. Chen, Y.-F. Xu, J.-T. Li, S.-L. Chou, S.-X. Dou, and S.-G. Sun, "Facile synthesis of a interleaved expanded graphite-embedded sulphur nanocomposite as cathode of Li-S batteries with excellent lithium storage performance," *Journal of Materials Chemistry*, vol. 22, no. 11, p. 4744, 2012.
- [84] L. S. Cells, L. Ji, M. Rao, H. Zheng, L. Zhang, O. Y. Li, and W. Duan, "Graphene Oxide as a Sulfur Immobilizer in High Performance," *JACS*, pp. 18522–18525, 2011.
- [85] I. György and F.Scholz, "Conducting Polymers: A New Era in Electrochemistry," *Springer*, Chapter. 1, pp. 1–6, 2008
- [86] H. S. Nalwa, Ed., "Handbook of Nanostructured Materials and Nanotechnology," *Academic Press*: New York, NY, USA, 2000; Volume 5, p. 501
- [87] M. S. a. Rahaman, a. F. Ismail, and a. Mustafa, "A review of heat treatment on polyacrylonitrile fiber," *Polymer Degradation and Stability*, vol. 92, no. 8, pp. 1421–1432, Aug. 2007.

- [88] J. Wang, J. Yang, C. Wan, K. Du, J. Xie, and N. Xu, "Sulfur Composite Cathode Materials for Rechargeable Lithium Batteries," *Advanced Functional Materials*, vol. 13, no. 6, pp. 487–492, Jun. 2003.
- [89] J. Fanous, M. Wegner, J. Grimming, Ä. Andresen, and M. R. Buchmeiser, "Structure-Related Electrochemistry of Sulfur-Poly(acrylonitrile) Composite Cathode Materials for Rechargeable Lithium Batteries," *Chemistry of Materials*, vol. 23, no. 22, pp. 5024–5028, Nov. 2011.
- [90] L. Yin, J. Wang, J. Yang, and Y. Nuli, "A novel pyrolyzed polyacrylonitrile-sulfur@MWCNT composite cathode material for high-rate rechargeable lithium/sulfur batteries," *Journal of Materials Chemistry*, vol. 21, no. 19, p. 6807, 2011.
- [91] C. Vall, P. Jim, E. Mu, A. M. Benito, and W. K. Maser, "Simultaneous Reduction of Graphene Oxide and Polyaniline : Doping-Assisted Formation of a Solid-State Charge-Transfer Complex," pp. 10468–10474, 2011.
- [92] L. Xiao, Y. Cao, J. Xiao, B. Schwenzer, M. H. Engelhard, L. V Saraf, Z. Nie, G. J. Exarhos, and J. Liu, "A soft approach to encapsulate sulfur: polyaniline nanotubes for lithium-sulfur batteries with long cycle life.," *Advanced materials (Deerfield Beach, Fla.)*, vol. 24, no. 9, pp. 1176–81, Mar. 2012.
- [93] G.-C. Li, G.-R. Li, S.-H. Ye, and X.-P. Gao, "A Polyaniline-Coated Sulfur/Carbon Composite with an Enhanced High-Rate Capability as a Cathode Material for Lithium/Sulfur Batteries," *Advanced Energy Materials*, p. n/a–n/a, May 2012.
- [94] J. Wang, J. Chen, K. Konstantinov, L. Zhao, S. H. Ng, G. X. Wang, Z. P. Guo, and H. K. Liu, "Sulphur-polypyrrole composite positive electrode materials for rechargeable lithium batteries," *Electrochimica Acta*, vol. 51, no. 22, pp. 4634–4638, Jun. 2006.
- [95] X. Liang, Y. Liu, Z. Wen, L. Huang, X. Wang, and H. Zhang, "A nano-structured and highly ordered polypyrrole-sulfur cathode for lithium–sulfur batteries," *Journal of Power Sources*, vol. 196, no. 16, pp. 6951–6955, Aug. 2011.

- [96] X. Liang, Z. Wen, Y. Liu, H. Zhang, J. Jin, M. Wu, and X. Wu, "A composite of sulfur and polypyrrole–multi walled carbon combinatorial nanotube as cathode for Li/S battery," *Journal of Power Sources*, vol. 206, pp. 409–413, May 2012.
- [97] Y. Zhang, X. Wu, H. Feng, L. Wang, a Zhang, T. Xia, and H. Dong, "Effect of nanosized $Mg_{0.8}Cu_{0.2}O$ on electrochemical properties of Li/S rechargeable batteries," *International Journal of Hydrogen Energy*, vol. 34, no. 3, pp. 1556–1559, Feb. 2009.
- [98] A. Davies, "Development of Electro-active Graphene Nanoplatelets and Composites for Application as Electrodes within Supercapacitors" Thesis presented to University of Waterloo, 2012.
- [99] "Scanning electron microscope", Wikipedia.
http://en.wikipedia.org/wiki/Scanning_electron_microscope#Principles_and_capacities
- [100] "Scanning Electron Microscopy (SEM)", Geochemical Instrumentation and Analysis.
http://serc.carleton.edu/research_education/geochemsheets/techniques/SEM.html
- [101] Muso, "Energy-dispersive X-ray spectroscopy", Wikipedia.
http://en.wikipedia.org/wiki/Energy-dispersive_X-ray_spectroscopy
- [102] "Transmission electron microscopy", Wikipedia.
http://en.wikipedia.org/wiki/Transmission_electron_microscopy#Imaging_methods
- [103] "High-resolution transmission electron microscopy", Wikipedia.
http://en.wikipedia.org/wiki/High-resolution_transmission_electron_microscopy
- [104] "Atomic force microscopy", Wikipedia.
http://en.wikipedia.org/wiki/Atomic_force_microscopy
- [105] "Thermogravimetric analysis", Wikipedia.
http://en.wikipedia.org/wiki/Thermogravimetric_analysis

- [106] “Differential thermal analysis”, Wikipedia.
http://en.wikipedia.org/wiki/Differential_thermal_analysis
- [107] “Fourier transform infrared spectroscopy”, Wikipedia.
http://en.wikipedia.org/wiki/Fourier_transform_infrared_spectroscopy
- [108] “X-ray crystallography”, Wikipedia.
http://en.wikipedia.org/wiki/X-ray_crystallography
- [109] P.B.Balbuena, Y. Wang, Ed., “Lithium-Ion Batteries: Solid-Electrolyte Interphase,” *Imperial College Press*, p. 85, 2004.
- [110] “Elemental analysis”, Wikipedia.
http://en.wikipedia.org/wiki/Elemental_analysis
- [111] “Zeta potential”, Wikipedia.
http://en.wikipedia.org/wiki/Zeta_potential
- [112] “Double layer (interfacial)”, Wikipedia.
[http://en.wikipedia.org/wiki/Double_layer_\(interfacial\)](http://en.wikipedia.org/wiki/Double_layer_(interfacial))
- [113] J. O. Besenhard, Ed., *Handbook of Battery Materials*. Wiley-VCH, 1999.
- [114] “Cyclic voltammetry”, Wikipedia.
http://en.wikipedia.org/wiki/Cyclic_voltammetry
- [115] A. J. Bard, L. R. Faulkner, E. Swain, and C. Robey, “Fundamentals and Applications of Electrochemistry,” 2nd ed. John Wiley & Sons, Inc., 2001.
- [116] J. A. Dean, “Lange’s handbook of chemistry,” *McGraw Hill Book Co., New York, NY*, Jan. 1985.

- [117] Y. Cao, X. Li, I. a Aksay, J. Lemmon, Z. Nie, Z. Yang, and J. Liu, "Sandwich-type functionalized graphene sheet-sulfur nanocomposite for rechargeable lithium batteries.," *Physical chemistry chemical physics : PCCP*, vol. 13, no. 17, pp. 7660–5, May 2011.
- [118] X. Ji and L. F. Nazar, "Advances in Li–S batteries," *Journal of Materials Chemistry*, vol. 20, no. 44, p. 9821, 2010.
- [119] G.-C. Li, G.-R. Li, S.-H. Ye, and X.-P. Gao, "A Polyaniline-Coated Sulfur/Carbon Composite with an Enhanced High-Rate Capability as a Cathode Material for Lithium/Sulfur Batteries," *Advanced Energy Materials*, p. n/a–n/a, May 2012.
- [120] X. Liang, Z. Wen, Y. Liu, H. Zhang, J. Jin, M. Wu, and X. Wu, "A composite of sulfur and polypyrrole–multi walled carbon combinatorial nanotube as cathode for Li/S battery," *Journal of Power Sources*, vol. 206, pp. 409–413, May 2012.
- [121] J. Wang, J. Yang, C. Wan, K. Du, J. Xie, and N. Xu, "Sulfur Composite Cathode Materials for Rechargeable Lithium Batteries," *Advanced Functional Materials*, vol. 13, no. 6, pp. 487–492, Jun. 2003.
- [122] L. Xiao, Y. Cao, J. Xiao, B. Schwenzer, M. H. Engelhard, L. V Saraf, Z. Nie, G. J. Exarhos, and J. Liu, "A soft approach to encapsulate sulfur: polyaniline nanotubes for lithium-sulfur batteries with long cycle life.," *Advanced materials (Deerfield Beach, Fla.)*, vol. 24, no. 9, pp. 1176–81, Mar. 2012.
- [123] L. Yin, J. Wang, F. Lin, J. Yang, and Y. Nuli, "Polyacrylonitrile / Graphene composite as a precursor of sulfur-based cathode material for high-rate rechargeable Li-S batteries_SP," *Energy & Environmental Science*, 2012.
- [124] X. Ji, K. T. Lee, and L. F. Nazar, "A highly ordered nanostructured carbon-sulphur cathode for lithium-sulphur batteries.," *Nature materials*, vol. 8, no. 6, pp. 500–6, Jun. 2009.
- [125] G. He, X. Ji, and L. Nazar, "High 'C' rate Li-S cathodes: sulfur imbibed bimodal porous carbons," *Energy & Environmental Science*, vol. 4, no. 8, p. 2878, 2011.
- [126] Y.-S. Su and A. Manthiram, "A facile in situ sulfur deposition route to obtain carbon-wrapped sulfur composite cathodes for lithium–sulfur batteries," *Electrochimica Acta*, vol. 77, pp. 272–278, Aug. 2012.

- [127] X. Li, Y. Cao, W. Qi, L. V. Saraf, J. Xiao, Z. Nie, J. Mietek, J.-G. Zhang, B. Schwenzer, and J. Liu, "Optimization of mesoporous carbon structures for lithium-sulfur battery applications," *Journal of Materials Chemistry*, vol. 21, no. 41, p. 16603, 2011.
- [128] J. Kim, D.-J. Lee, H.-G. Jung, Y.-K. Sun, J. Hassoun, and B. Scrosati, "An Advanced Lithium-Sulfur Battery," *Advanced Functional Materials*, p. n/a-n/a, May 2012.
- [129] X. Liang, Z. Wen, Y. Liu, H. Zhang, L. Huang, and J. Jin, "Highly dispersed sulfur in ordered mesoporous carbon sphere as a composite cathode for rechargeable polymer Li/S battery," *Journal of Power Sources*, vol. 196, no. 7, pp. 3655-3658, Apr. 2011.
- [130] S. Wei, H. Zhang, Y. Huang, W. Wang, Y. Xia, and Z. Yu, "Pig bone derived hierarchical porous carbon and its enhanced cycling performance of lithium-sulfur batteries," *Energy & Environmental Science*, vol. 4, no. 3, p. 736, 2011.
- [131] C. Zhang, H. Bin Wu, C. Yuan, Z. Guo, and X. W. D. Lou, "Confining Sulfur in Double-Shelled Hollow Carbon Spheres for Lithium-Sulfur Batteries," *Angewandte Chemie International Edition*, p. n/a-n/a, Aug. 2012.
- [132] G. Zheng, Y. Yang, J. J. Cha, S. S. Hong, and Y. Cui, "Hollow carbon nanofiber-encapsulated sulfur cathodes for high specific capacity rechargeable lithium batteries.," *Nano letters*, vol. 11, no. 10, pp. 4462-7, Oct. 2011.
- [133] R. Elazari, G. Salitra, A. Garsuch, A. Panchenko, and D. Aurbach, "Sulfur-impregnated activated carbon fiber cloth as a binder-free cathode for rechargeable Li-S batteries.," *Advanced materials (Deerfield Beach, Fla.)*, vol. 23, no. 47, pp. 5641-4, Dec. 2011.
- [134] J. Guo, Y. Xu, and C. Wang, "Sulfur-impregnated disordered carbon nanotubes cathode for lithium-sulfur batteries.," *Nano letters*, vol. 11, no. 10, pp. 4288-94, Oct. 2011.
- [135] L. Ji, M. Rao, S. Aloni, L. Wang, E. J. Cairns, and Y. Zhang, "Porous carbon nanofiber-sulfur composite electrodes for lithium/sulfur cells," *Energy & Environmental Science*, vol. 4, no. 12, p. 5053, 2011.
- [136] L. Yin, J. Wang, J. Yang, and Y. Nuli, "A novel pyrolyzed polyacrylonitrile-sulfur@MWCNT composite cathode material for high-rate rechargeable lithium/sulfur batteries," *Journal of Materials Chemistry*, vol. 21, no. 19, p. 6807, 2011.

- [137] W. Wei, J. Wang, L. Zhou, J. Yang, B. Schumann, and Y. NuLi, "CNT enhanced sulfur composite cathode material for high rate lithium battery," *Electrochemistry Communications*, vol. 13, no. 5, pp. 399–402, May 2011.
- [138] F. Zhang, X. Zhang, Y. Dong, and L. Wang, "Facile and effective synthesis of reduced graphene oxide encapsulated sulfur via oil/water system for high performance lithium sulfur cells," *Journal of Materials Chemistry*, vol. 22, no. 23, p. 11452, 2012.
- [139] Y.-X. Wang, L. Huang, L.-C. Sun, S.-Y. Xie, G.-L. Xu, S.-R. Chen, Y.-F. Xu, J.-T. Li, S.-L. Chou, S.-X. Dou, and S.-G. Sun, "Facile synthesis of a interleaved expanded graphite-embedded sulphur nanocomposite as cathode of Li-S batteries with excellent lithium storage performance," *Journal of Materials Chemistry*, vol. 22, no. 11, p. 4744, 2012.
- [140] J.-Z. Wang, L. Lu, M. Choucair, J. a. Stride, X. Xu, and H.-K. Liu, "Sulfur-graphene composite for rechargeable lithium batteries," *Journal of Power Sources*, vol. 196, no. 16, pp. 7030–7034, Aug. 2011.
- [141] H. Wang, Y. Yang, Y. Liang, J. T. Robinson, Y. Li, A. Jackson, Y. Cui, and H. Dai, "Graphene-wrapped sulfur particles as a rechargeable lithium-sulfur battery cathode material with high capacity and cycling stability.," *Nano letters*, vol. 11, no. 7, pp. 2644–7, Jul. 2011.
- [142] L. S. Cells, L. Ji, M. Rao, H. Zheng, L. Zhang, O. Y. Li, and W. Duan, "Graphene Oxide as a Sulfur Immobilizer in High Performance," *JACS*, pp. 18522–18525, 2011.
- [143] Y.-X. Wang, L. Huang, L.-C. Sun, S.-Y. Xie, G.-L. Xu, S.-R. Chen, Y.-F. Xu, J.-T. Li, S.-L. Chou, S.-X. Dou, and S.-G. Sun, "Facile synthesis of a interleaved expanded graphite-embedded sulphur nanocomposite as cathode of Li-S batteries with excellent lithium storage performance," *Journal of Materials Chemistry*, vol. 22, no. 11, p. 4744, 2012.
- [144] D. Li, M. B. Müller, S. Gilje, R. B. Kaner, and G. G. Wallace, "Processable aqueous dispersions of graphene nanosheets-sp," *Nature nanotechnology*, vol. 3, no. 2, pp. 101–5, Feb. 2008.
- [145] R. E. O. William S. Hummers Jr., "Preparation of Graphitic Oxide," vol. 208, no. 1937, p. 1937, 1957.
- [146] S. A. Ju, K. Kim, J.-H. Kim, and S.-S. Lee, "Graphene-wrapped hybrid spheres of electrical conductivity.," *ACS applied materials & interfaces*, vol. 3, no. 8, pp. 2904–11, Aug. 2011.

- [147] J. Zhang, H. Yang, G. Shen, P. Cheng, J. Zhang, and S. Guo, "Reduction of graphene oxide via L-ascorbic acid.," *Chemical communications (Cambridge, England)*, vol. 46, no. 7, pp. 1112–4, Feb. 2010.
- [148] J. Fanous, M. Wegner, J. Grimming, Ä. Andresen, and M. R. Buchmeiser, "Structure-Related Electrochemistry of Sulfur-Poly(acrylonitrile) Composite Cathode Materials for Rechargeable Lithium Batteries," *Chemistry of Materials*, vol. 23, no. 22, pp. 5024–5028, Nov. 2011.
- [149] A. G. Macdiarmid, "“Synthetic Metals^o: A Novel Role for Organic Polymers (Nobel Lecture)**,” *Angew.Chem.Int.Ed*, no. 40, pp. 2581–2590, 2001.
- [150] Y. V. Mikhaylik and J. R. Akridge, "Polysulfide Shuttle Study in the Li/S Battery System," *Journal of The Electrochemical Society*, vol. 151, no. 11, p. A1969, 2004.
- [151] V. V Shinkarev, V. B. Fenelonov, and G. G. Kuvshinov, "S ulfur distribution on the surface of mesoporous nanofibrous carbon," vol. 41, pp. 295–302, 2003.
- [152] B. Zhang, X. Qin, G. R. Li, and X. P. Gao, "Enhancement of long stability of sulfur cathode by encapsulating sulfur into micropores of carbon spheres," *Energy & Environmental Science*, vol. 3, no. 10, p. 1531, 2010.
- [153] V. S. Kolosnitsyn and E. V. Karaseva, "Lithium-sulfur batteries: Problems and solutions," *Russian Journal of Electrochemistry*, vol. 44, no. 5, pp. 506–509, Jun. 2008.